Copyright Undertaking

This thesis is protected by copyright, with all rights reserved.

By reading and using the thesis, the reader understands and agrees to the following terms:

1. The reader will abide by the rules and legal ordinances governing copyright regarding the use of the thesis.
2. The reader will use the thesis for the purpose of research or private study only and not for distribution or further reproduction or any other purpose.
3. The reader agrees to indemnify and hold the University harmless from and against any loss, damage, cost, liability or expenses arising from copyright infringement or unauthorized usage.

IMPORTANT

If you have reasons to believe that any materials in this thesis are deemed not suitable to be distributed in this form, or a copyright owner having difficulty with the material being included in our database, please contact lbsys@polyu.edu.hk providing details. The Library will look into your claim and consider taking remedial action upon receipt of the written requests.

Pao Yue-kong Library, The Hong Kong Polytechnic University, Hung Hom, Kowloon, Hong Kong

http://www.lib.polyu.edu.hk

This thesis in electronic version is provided to the Library by the author. In the case where its contents is different from the printed version, the printed version shall prevail.

FABRICATION AND CHARACTERIZATION OF TWO-DIMENSIONAL LAYERED MATERIALS FOR ELECTRONIC AND OPTOELECTRONIC APPLICATIONS

HUI YEUNG YU

Ph.D

The Hong Kong Polytechnic University

2015

The Hong Kong Polytechnic University

Department of Applied Physics

Fabrication and Characterization of Two-Dimensional Layered Materials for Electronic and Optoelectronic Applications

Hui Yeung Yu

A thesis submitted in partial fulfillment of the requirements

for the degree of Doctor of Philosophy

August 2014

THE HONG KONG POLYTECHNIC UNIVERSITY

Certificate of Originality

I hereby declare that this thesis is my own work and that, to the best of my knowledge and belief, it reproduces no material previously published or written nor material which has been accepted for the award of any other degree or diploma, except where due acknowledgement has been made in the text.

____________________ (Signature)

_____Hui Yeung Yu___ (Name of candidate)

Abstract

Graphene has been attracting great interest because of its distinctive band structure and physical properties. Single crystalline graphene is limited to small sizes as it is produced mostly by exfoliating graphite. Large-area graphene films of the order of centimeters on copper substrates are fabricated by chemical vapor deposition (CVD) technique but they are in polycrystalline structure. The films are predominantly single-layer graphene, with a small percentage of the area having few layers, and are continuous and homogenous. The realization of *n*- and *p*-type graphene field-effect transistors (GFETs) by controlling merely the thickness of a zinc oxide (ZnO) nanomesh deposited on the graphene was demonstrated. This nanopatterning technique could open up new opportunities for developing electronic and optoelectronic devices that are based on graphene.

The absence of a bandgap for graphene has limited its application in nanoelectronics. The well-studied semi-conducting two-dimensional (2D) material is the layered metal chalcogenides (LMDCs), the most common being molybdenum disulfide (MoS_2). Large-area MoS_2 films of the order of centimeters on sapphire substrates were prepared by CVD. The films can be single-layer or multi-layer.

Tuning band energies of semiconductors through strain engineering can significantly enhance their electronic, photonic, and spintronic performances. We developed an electromechanical device that can apply biaxial compressive strain to tri-layer MoS_2 supported by a piezoelectric substrate and covered by a transparent graphene electrode. Photoluminescence (PL) and Raman characterizations show that the direct bandgap can be blue shifted for ~ 300 meV per 1% strain. First principle investigations confirm that the blue-shift of the direct bandgap and reveal a higher tunability of the indirect bandgap than the direct one. The exceptionally high strain tunability of the electronic structure in MoS_2 promises a wide range of applications in functional nanodevices and the developed methodology should be generally applicable for 2D semiconductors.

Although strain engineering in 2D materials is possible nowadays, most of the strain engineering techniques require external agent to apply strain onto the 2D materials. We developed a novel approach to apply continuous strain to any 2D materials on arbitrary substrates. Monolayer MoS_2 was transferred onto patterned SiO_2/Si substrates with inclined trenches of different sizes, 5×5, 10×10 and 20×20 μm^2. One side of the MoS_2 layer was in contact with the inclined plane of the trench and the other side was free standing within the trench. This structure created continuous strain

from tensile to compressive. An exceptional total Raman and PL shift of 12 cm^{-1} and 14 nm were recorded respectively from the 20×20 μm^2 sample. It is found that the amount of induced strain depends on the size of the trenches. The approach provides a platform to study the strain induced properties in 2D semiconductors.

List of Publications

Journal Articles

- H. Y. Yang, S. F. Yu, Y. Y. Hui, and S. P. Lau, *Electroluminescence from AlN nanowires grown on p-SiC substrate*, Appl. Phys. Lett **97**, 191105 (2010)
- Yeung Yu Hui, Guo'an Tai, Zhenhua Sun, Zihan Xu, Ning Wang, Feng Yan and Shu Ping Lau, *n- and p-Type modulation of ZnO nanomesh coated graphene field effect transistors*, Nanoscale **4**, 3118-3122 (2012)
- Yeung Yu Hui, Jing Ye, Rolf Lortz, Kar Seng Teng, and Shu Ping Lau, *Magnetic properties of Mg-doped AlN zigzag nanowires*, Phys. Status Solidi A **200**, 1988 (2012)
- W. Wang, K. K. Leung, W. K. Fong, S. F. Wang, Y. Y. Hui, S. P. Lau, Z. Chen, L. J. Shi, C. B. Cao and C. Surya, *Molecular beam epitaxy growth of high quality p-doped SnS van der Waals epitaxy on a graphene buffer layer*, J. Appl. Phys. **111**, 093520 (2012)
- Wenjing Jie, Yeung Yu Hui, Ngai Yui Chan, Yang Zhang, Shu Ping Lau and Jianhua Hao, *Ferroelectric Polarization Effects on the Transport Properties of Graphene/PMN-PT Field Effect Transistors,* J. Phys. Chem. C **117**, 13747

(2013)

- Wenjing Jie, Yeung Yu Hui, Yang Zhang, Shu Ping Lau and Jianhua Hao, *Effects of controllable biaxial strain on the Raman spectra of monolayer graphene prepared by chemical vapor deposition,* Appl. Phys. Lett. **102**, 223112 (2013)

- Yuda Zhao, Yizhu Xie, Yeung Yu Hui, Libin Tang, Wenjing Jie, Yifan Jiang, Ling Xu, Shu Ping Lau and Yang Chai, *Highly impermeable and transparent graphene as an ultra-thin protection barrier for Ag thin films,* J. Mater. Chem. C. **1**, 4956 (2013)

- Yeung Yu Hui, Xiaofei Lu, Wenjing Jie, Ngai Yui Chan, Jianhua Hao, Yu-Te Hsu, Lain-Jong Li, Wanlin Guo and Shu Ping Lau, *Exceptional Tunability of Band Energy in a Compressively Strained Tri-layer MoS_2 Sheet,* ACS Nano **7**, 7126 (2013)

- Chao Ping Liu, Yeung Yu Hui, Zhen Hua Chen, Jian Guo Ren, Ye Zhou, Libin Tang, Yong Bing Tang, Juan Antonio Zapien and Shu Ping Lau, *Solution-processable graphene oxide as an insulator layer for metal-insulator-semiconductor silicon solar cells*, RCS Adv. **3**, 17918 (2013)

- Kelvin K. Leung, Wei Wang, Haibo Shu, Yeung Yu Hui, Shifeng Wang, Patrick W. K. Fong, Feng Ding, Shu Ping Lau, Chi-hang Lam and Charles Surya,

Theoretical and experimental Investigations on the Growth of SnS van der Waals Epitaxies on Graphene Buffer Layer, Cryst. Growth. Des. **13**, 4755 (2013)

Acknowledgements

The graduate study at The Hong Kong Polytechnic University has been one of the most important and exciting periods in my life. I would like to express my deep appreciation to many people who have favored me with a lot of help and made these years enjoyable and fruitful.

First and foremost, I would like to express my sincerest and deepest appreciation to my supervisor, Prof. S. P. Lau, for his professional and invaluable advices throughout the past 3 years in my PhD study. Not only did he guide me in my research difficulties, but also he did help me in my hard time in my daily issues. His great broad view, deep insight and enthusiasm towards research have been a great inspiration to me in defining the most important scientific problems. His opinions helped me through many difficulties in my study and research.

I specially thank Dr. Lain-Jong Li, Ming-Hui Chiu and Chang-Lung Hsu for their help in Raman measurement and MoS_2 fabrications as well as their great interest and strong support of my work when I visited Institute of Atomic and Molecular sciences, Taipei, Taiwan.

Special thanks are also due to Dr. W. Lu for his help in the TEM measurement, Dr. Hardy for the thermal evaporation operations; Dr. F. Yan for the FET measurement; Dr. Jianhua Hao and Mrs Wenjing Jie for the PL measurement; Mr Ngai Yui Chan for the XRD measurement. Their supports to my work are highly appreciated.

I have also enjoyed working with an outstanding group of highly motivated people. I would like to thank my research companions: Mr. Au Kit, Mr. Simon Luk, Dr. L.B. Tang and Ms. Theresa Ng for their useful suggestions and assistant.

Last but not least, I would like to thank my parents for their patience and endless support throughout my life. They have been inspiring me at every moment.

Table of Contents

Certificate of Originality i

Abstract ii

List of Publications v

Acknowledgements viii

Table of Contents x

List of Figures xiii

List of Tables xxi

Chapter 1 Introduction 1

1.1 Background and motivation 1

1.2 Scope of this project 10

Chapter 2 Two-Dimensional Materials 12

2.1 Background 12

2.2 Structure 14

2.3 Growth 17

2.3.1 CVD growth of graphene 17

2.3.2 Growth of MoS_2 19

2.4 Electrical properties 21

2.5 Optical properties 24

2.6 Strained properties 25

2.6.1 Theoretical prediction of strained behavior 25

2.6.2 Local strain engineering 26

Chapter 3 Experimental Details 28

3.1 Growth of 2D materials and transfer process 28

3.1.1 Growth and transfer of graphene 28
3.1.2 Growth of tri-layer MoS_2 29
3.1.3 Growth of monolayer MoS_2 30
3.2 Structural characterization 31
3.2.1 X-ray diffraction (XRD) 31
3.2.2 Scanning Electron Microscopy (SEM) 33
3.2.3 Transmission electron microscopy (TEM) 35
3.2.4 Raman spectroscopy 36
3.3 Optical characterization 38
3.3.1 Photoluminescence (PL) 38
3.4 Substrate patterning 39
3.4.1 Focused ion beam 39
Chapter 4 Graphene Field Effect Transistors 41
4.1 Introduction 41
4.2 Experiment 43
4.3 Results and Discussion 45
4.3.1 Structural Properties of Graphene 45
4.3.2 Characterization of ZnO nanomesh Coated Graphene 48
4.3.3 Field Effect Transistor characteristics 49
4.3.4 Raman characteristics 53
4.3.5 Effect of Annealing Temperature and ZnO Thickness 57
4.4 Summary 59
Chapter 5 Biaxial Strain in MoS_2 60
5.1 Introduction 60
5.2 Experiment 62

5.3 Result and Discussion 63
5.3.1 Fabrication of electro-mechanical device 63
5.3.2 X-ray diffraction characterization 65
5.3.3 Elastic properties 68
5.3.4 Raman characterization 69
5.3.5 First-principles calculations 73
5.4 Summary 80
Chapter 6 Local Strain Profile in 2D Materials 81
6.1 Introduction 81
6.2 Experiment 83
6.3 Results and Discussions 85
6.3.1 Strain engineered MoS_2 85
6.3.2 Raman characterization 87
6.3.3 PL characterization of the strained MoS_2 94
6.4 Summary 96
Chapter 7 Conclusion and Future Work 98
7.1 Conclusion 98
7.2 Future work 100
References 101

List of Figures

Fig. 2.1 Properties of graphene and graphene nanoribbons. (a)Schematic of an armchair (ac) graphene nanoribbon (GNR) of length L_{ac} and width W_{ac}. The nanoribbon shown here has $N = 9$ carbon atoms along its width and thus belongs to the $3p$ family, where p is an integer. (b)Band structure around the K point of (i)large-area graphene, (ii)graphene nanoribbons, (iii)unbiased bilayer graphene, and (iv)bilayer graphene with an applied perpendicular field. Large-area graphene and unbiased bilayer graphene do not have a bandgap, which makes them less useful for digital electronics [8]. 16

Fig. 2.2(a)Crystal structures of the 1T and 2H crystal structures of the MX_2 family (X = yellow sphere). The metal is in octahedral coordination in the 1T structure, and trigonal prismatic coordination in the two layers per unit cell 2H crystal structure [9]. (b)Crystal structure of MoS_2 [10]. 17

Fig. 2.3 Schematic illustration showing the dissociation-dissolution-segregation on Cu and the surface-mediated growth of monolayer graphene on Cu [11]. 19

Fig. 2.4(a)A schematic illustration of the MoS_2 CVD system. (b)The temperature programming process used for a typical growth [13]. 20

Fig. 2.5(a)Growth setup and conditions. (b)Cartoon indicating the structure of the triangular monolayer crystallites. (c)Structure of monolayer MoS_2 [14]. 21

Fig. 2.6(a)Schematic illustration of cross section of MoS_2 FET. (b)Transfer characteristic of a monolayer MoS_2 transistor in linear scale [19]. 23

Fig. 2.7 Calculated band structures of (a)bulk and (b)monolayer MoS_2. The solid arrows indicate the lowest-energy transitions. (c)PL spectra for mono- and bilayer MoS_2 samples. Inset: PL quantum yield of thin layers of MoS_2 for number of layers N = 1−6 in log scale [20]. 24

Fig. 2.8(a)Biaxial strain-dependent optical absorption spectra calculated. (b)Biaxial strain-dependent quasiparticle energies for electrons and holes at the K point. Inset: atomic structure of MoS_2 monolayer [21]. 26

Fig. 2.9 Localized uniaxial strain in MoS_2. (a)Schematic diagram of the fabrication process of wrinkled MoS_2 monolayers. An elastomeric substrate is stretched prior depositing MoS_2 by mechanical exfoliation. The strain is released afterward, producing buckling-induced delamination of the MoS_2 flakes. (b)Raman spectra measured on a flat (blue) and on a wrinkled (red) region of a 40-layer-thick MoS_2 flake. Although both E^1_{2g} and A_{1g} modes are shifted towards a lower Raman shift, the E^1_{2g} presents the higher shift. (c)photoluminescence spectra measured on the flat region (blue) and on top of the wrinkle (red) in the same MoS_2 flake [22]. 27

Fig. 3.1 Schematic diagram of a tube furnace used for synthesizing graphene. 29

Fig. 3.2 Schematic illustration of the two-step thermolysis process for the synthesis of MoS_2 thin layers on insulating substrates [23]....30

Fig. 3.3 Schematic diagram showing the CVD process to fabricate monolayer MoS_2 ..31

Fig. 3.4 Schematic diagram showing the principle of XRD. 32

Fig. 3.5 Schematic diagram showing the principle of SEM. 34

Fig. 3.6 Schematic diagram showing the principle of Raman scattering. 37

Fig. 3.7 Schematic diagram showing the principle of FIB. 40

Fig. 4.1 Schematic diagram showing the fabrication process of a ZnO nanomesh coated GFET. (a)Preparation of clean hydrophilic SiO_2 (300nm)/Si substrate. (b)Transfer of CVD grown graphene. (c)Coating of monolayer PS spheres on graphene. (d)Deposition of ZnO film on PS spheres coated graphene. (e)Removal of PS spheres by chloroform for the formation of ZnO nanomesh. (f)Deposition of Au electrodes by optical lithography. 44

Fig. 4.2(a) Comparison between as-received Cu foil and graphene covered Cu foil. (b)A transferred graphene on a Si substrate with 300 nm thick of SiO_2 on top. (c)Optical image of a graphene covered with some PMMA residue. (d)Optical image of a graphene with a clean surface. 46

Fig. 4.3 Raman spectra of (a)bilayer graphene, (b)single layer graphene, (c)graphene on SiO_2/Si and (d)graphene on Cu. 47

Fig. 4.4 SEM images of (a)PS spheres coated graphene, (b)ZnO deposited PS spheres/graphene, (c)ZnO nanomesh coated graphene and (d)ZnO nanomesh coated graphene device with Au electrode separation of 5 μm. (e)AFM image of the 17 nm thick ZnO nanomesh coated on graphene. 49

Fig. 4.5 Transfer characteristics of (a)*n*-type, (b)pristine and (c)*p*-type GFETs before annealing (blue lines) and after subsequent annealing at 100 (red lines) and 200 ^{o}C (black lines) in N_2 atmosphere, which were measured at room temperature. (d)Transfer characteristic of the 200 ^{o}C annealed *n*-type, pristine and *p*-type GFETs measured at room temperature. These devices were measured with the applied V_{DS} of 0.05 V. 52

Fig. 4.6(a)Raman spectra of *n*-type, pristine and *p*-type GFETs. The corresponding magnified Raman (b)G and (c)2D bands. 57

Fig. 4.7(a)CNP as a function of annealing temperature for the *n*-type, pristine and *p*-type GFETs. (b)CNP as a function of ZnO nanomesh thickness for the ZnO nanomesh coated GFETs. 59

Fig. 5.1 Experimental setup and structural properties of tri-layer MoS_2. (a) Schematic diagram of Raman and PL measurements on MoS_2 which is sandwiched between a piezoelectric PMN-PT substrate and a graphene top electrode. (b)High-resolution TEM image at the edge of tri-layer MoS_2. (c)AFM image

of the tri-layer MoS_2. The inset shows the depth profile of the tri-layer MoS_2 which indicates a thickness of 2.1 nm..65

Fig. 5.2(a) The XRD shifts of the PMN-PT substrate at bias voltages from 0 to 500 V. (b)The XRD shifts and the corresponding induced compressive strain as a function of bias voltage. 67

Fig. 5.3(a)The XRD peak shifts of the tri-layer MoS_2 at different applied strains. (b)The corresponding XRD peak shift as a function of applied strain. The inset shows the full GIA XRD spectrum of the tri-layer MoS_2. 68

Fig. 5.4(a)The PL peak position and strain as a function of bias voltage. (b)The dependence of the PL peak position as a function of strain (step 1: increasing strain and step 2: decreasing strain). 69

Fig. 5.5 Raman spectra of tri-layer MoS_2 under different strains. (a)The Raman spectra of the tri-layer MoS_2 under various applied strains. (b)The Raman shift of E_{2g}^1 and A_{1g} modes as a function of strain. (c)The Raman shift of E_{2g}^1 and A_{1g} modes as a function of strain calculated by density functional perturbation theory. (d)1D spatial mapping of the Raman shift of E_{2g}^1 and A_{1g} modes under the applied strain of 0.2%. 71

Fig. 5.6 Photoluminescence property of tri-layer MoS_2 under strain. (a)The PL spectra of the MoS_2 under various strains. (b)The PL peak energy as a function of

compressive strain. The inset shows the PL spectra of the sample under 0.0 % and 0. 2 % strain. 73

Fig. 5.7 First-principles band structures of tri-layer MoS_2. (a)Band structures of *Ab-bA* stacking tri-layer MoS_2 under 0.0, 0.2, 0.4 and 0.6% biaxial compressive strain. (b)Energy gaps as a function of biaxial compressive strain. 75

Fig. 5.8 First-principles band structure calculations of tri-layer MoS_2. (a)Schematic illustrations of the *Ab-Ab* and *Ab-bA* stacking tri-layer MoS_2. (b)Raman shifts as a function of biaxial compressive strain. (c)Energy gaps as a function of biaxial compressive strain. 77

Fig. 5.9(a)Optical micrograph of the tri-layer MoS_2 placed on PMN-PT substrate showing the PL intensity mapping area (10×10 μm^2). The bottom graph is the PL spectrum of the sample. (b)Raman intensity mapping of the E2g1 (bottom) and A_{1g} (top) modes in the scanning area. (c)2D (top) and 3D (bottom) spatial mappings of the Raman shift of E^1_{2g} and A_{1g} modes. 79

Fig. 6.1 Schematic diagram showing the fabrication process of the strained MoS_2 layer on SiO_2/Si substrate. 85

Fig. 6.2 Schematic diagram showing our experimental configuration of the strained MoS_2 layer on top of Si/SiO_2 substrate. 87

Fig. 6.3(a)Optical image of the inclined trenches with different sizes: 5×5, 10×10 and

20×20 μm^2. (b)SEM image of the 20×20 μm^2 inclined trench. (c)Optical image of a MoS_2 transferred onto a 20×20 μm^2 inclined trench. The free standing MoS_2 layer is visible in optical microscope, which looks like a “curtain” as indicate by the red dotted rectangle. 88

Fig. 6.4(a) and (b)Raman shift mapping profile of the E_{2g}^1 and A_{1g} peaks of a strained MoS_2 on a 20×20 μm^2 inclined trench. The dark contrast in Raman shift mapping represents a shift to lower frequency (red shift, which is tensile strain). In the inclined region, the bright contrast represents a shift to higher frequency (blue shift, which is compressive strain). (c)Raman spectra of the corresponding sample in different regions of the trench...............................91

Fig. 6.5(a) Raman shifts (E_{2g}^1 and A_{1g} peaks) of the strained MoS_2 on a 20×20 μm^2 inclined trench as a function of y-direction. (b)Raman spectra of the corresponding sample in different regions. (c)Raman shift of the E_{2g}^1 and A_{1g} peaks as a function of edge length of the inclined trenches . (d)The estimated strain on the sample as a function of Raman shift [101]. 92

Fig. 6.6(a) Raman shift profile alone the y-direction of the strained MoS_2 on a 10×10 μm^2 trench of the E_{2g}^1 and A_{1g} peaks. (b) The Raman shifts as a function of strain...93

Fig. 6.7(a)Raman shift profile of the strained MoS_2 on a 10×10 μm^2 trench alone the

x-direction of the E_{2g}^{1} and A_{1g} modes. (b)Raman spectra of the strained MoS_2 along the x-direction. 94

Fig. 6.8(a)PL spectra of the MoS_2 along y-direction on a 10×10 μm^2 trench. (b)PL peak position as a function of y-direction. 95

Fig. 6.9 (a)PL spectra of the sample with 20×20 μm^2 trench size at different regions. (b)The variation of PL peak positions of the samples with different edge length of the inclined trenches: 5×5, 10×10 and 20×20 μm^2. 96

Fig. 7.1 Schematic diagram showing a free standing MoS_2 FET.................................100

List of Tables

Table. 5.1 Biaxial compressive strain correlated bandgap energy of tri-layer MoS_2......76

Chapter 1 Introduction

1.1 Background and motivation

Two-dimensional (2D) materials have the atomic organization and bond strength along two-dimensions, which are similar and much stronger than along a third dimension. The 2D materials can be single-atom-thick or polyhedral-thick layers of atoms with covalent or ionic bonding along two dimensions and van der Waals bonding along the third. These 2D materials stack with more than one atomic layer are called nanosheets. The stacking of these nanosheets can be assembly or hybrid composite formed from single to many layers of 2D materials, having the interlayer between 2D structures contacted by weak van der Waals forces. In general, these van der Waals solid can be prepared as a single-atom or single-polyhedral thick layer. These crystal structures feature neutral, single-atom-thick or polyhedral-thick layers of atoms that are covalently connected with their neighbors within each layer, whereas the layers are held together via van der Waals bonding along the third axis. The weak interlayer van der Waals energies (~40-70 meV) enable the facile exfoliation of these layers. These materials can exhibit unique and fascinating physical properties. Even at one-atom-thick, 2D materials can be fantastic electronics and thermal conductor. These materials have been proposed for a vast of applications ranging from transparent conductors to

thermal interface materials to barrister transistor-like devices. Still, there exists an entire periodic table of crystalline solid-state materials each having different electronic, mechanical, and transport properties, and the possibility to create single-atom or few-atom polyhedral thick 2D layers from any material remains.

The most famous class of van der Waals solid is the single-element-made graphene which is the first discovered single-layer material. Single-layer graphene is a purely 2D material. Its lattice consists of regular hexagons with a carbon atom at each corner. At present, the most popular approaches to prepare graphene are mechanical exfoliation, growth on metals and subsequent transfer to insulating substrates, thermal decomposition of silicon carbide (SiC) to produce so-called epitaxial graphene on top of SiC wafers. Large-area graphene is a semimetal with zero bandgap. Its valence and conduction bands are cone-shaped and meet at the K points of Brillouin zone. Because the bandgap is zero, devices with channels made of large-area graphene cannot be switched off and therefore are not suitable for logic applications. However, the band structure of graphene can be modified, and it is possible to open a bandgap in three ways by constraining large-area graphene in one dimension to form nanoribbons, by biasing bilayer graphene and by applying strain to graphene. Yet, there are still a lot of applications for graphene other than

semiconducting industry, such as using it as transparent electrode in 2D devices.

In this thesis, we mainly focus on 2D materials that can possibly have further prospects in replacing traditional bulk materials. Since silicon is approaching its limit, there are more and more efforts on finding new type of materials to replace it. 2D materials, such as graphene and molybdenum disulfide (MoS_2), have emerged as promising candidates that could solve the problem of making ever faster computers and smaller mobile devices when silicon microchip hits an inevitable wall. Graphene, a single layer of carbon atoms in a close packed hexagonal arrangement, is a highly researched material due to the fact that it has incredible electronic properties such as, theoretical speeds 100 times greater than silicon. These systems could be important for microelectronics, various types of hypersensitive sensors, catalysis, tissue engineering and energy storage. Recently, a combination of graphene and hexagonal boron nitride to produce improved transistor performance at an industrially relevant scale has been reported. The distinct properties of layer structured materials have attracted more and more interest nowadays. It will be of significant importance to investigate different kinds of 2D materials and make use of their extraordinary properties. If that is true, new kinds of devices could be fabricated.

Graphene has attracted enormous attention due to their enhanced electronic and mechanical properties compared to bulk materials. These unusual physical phenomena can occur when charge and heat transport is confined to a plane. Even at one-atom-thick, graphene can be fantastic electronics and thermal conductor. We proposed an alternative method to tune the bandgap of graphene. By controlling the thickness of the ZnO nanomesh deposited onto graphene, *n*- and *p*-type GFETs are demonstrated. The effect of thermal strain acting on the graphene by the substrate can be minimized for the devices that are covered with a layer of ZnO nanomesh. No further shifts of charge neutrality point (CNP) can be observed even the GFETs are subjected to annealing temperature of 400 ^{o}C. This suggests that the thermal stability of the ZnO nanomesh coated GFETs can be enhanced significantly. Besides, we note that the quality, cleanness and flatness of the single-layer graphene are of significant importance to influence the quality of the ZnO nanomesh which in turn affects the *n*- and *p*-type doping of the GFETs. The *n*- and *p*-type behavior of the GFETs can be explained by spectroscopic methods based on Raman D-band frequency sampling and by the transfer characteristics.

Another well-studied families of van der Waals solids is the layered metal

chalcogenides (LMDCs), the most common one being MoS_2. There are over 30 different LMDCs which have many technologically interesting properties, and an emerging body of experimental work investigating the structure and properties of single- and few-layer-thick derivatives has evolved for many of these compounds (MoS_2, WS_2 and $TiSe_2$). Correlated electronic phenomena can also be found from the layered metal dichalcogenides (LMDCs), such as charge density waves and high-temperature superconductivity. The bulk LMDCs normally has an indirect-gap, which is built up of van der Waals bonded X-M-X units (for example S-Mo-S). Each of these stable units (referred to as a MoS_2 monolayer) consists of two hexagonal planes of S atoms and an intermediate hexagonal plane of Mo atoms coordinated through ionic-covalent interactions with the S atoms in a trigonal prismatic arrangement. Because of the relatively weak interactions between these layers and the strong interlayer interactions, the formation of ultrathin crystal of MoS_2 by the cleavage technique is possible. Experiments reveal that a progressive confinement-induced shift in the indirect gap from the bulk value of 1.29 eV to over 1.90 eV is observed. The change in the indirect-gap energy was found to be significantly larger than that of the direct gap. The crossover from an indirect-gap material to a direct-gap material can increase the electronic and optical properties of the semiconducting devices. The controllability

of the band gap may also be used to optimize the materials' optoelectronic applications.

Tuning the band structure of 2D materials by subject it to strain constitutes an important strategy to enhance the performance of electronic devices. Not only the bandgap of a 2D material can be changed, but also the mobility of charge carriers can be changed by strain. By applying a strain through lattice mismatch between epitaxial films and substrates or through bending of films on elastic substrates, this strategy can be used to increase the carrier mobility in semiconductors or to lift the emission efficiency of light-emitting devices. Particularly, due to reduced dimensions, nanostructures become more flexible to be highly strained, which provides more space for strain engineering. A vast of strain effects on the electronic behaviors in quasi one-dimensional nanostructures such as carbon nanotube, GaAs nanowire and ZnO nanowire have been revealed. Technically speaking the emerging 2D crystals with a bandgap such as MoS_2 shall be more favored for strain engineering, as they only consist of one or few atoms in thickness. Whereas the strain-tunable phonon properties in MoS_2 are intensively studied by Raman scattering, the theoretically predicted bandgap tuning of MoS_2 by strain is the building block for the straining properties of MoS_2. Because of its distinctive

electronic and optical properties, its bandgap has been predicted to be highly strain-tunable. We have developed a novel electro-mechanical device to apply uniform and controllable biaxial compressive strain up to 0.2 % in tri-layer MoS_2 and performed photoluminescence (PL) and Raman detections simultaneously. The strain is applied by a piezoelectric substrate, while its transparency to PL detection is realized by using a graphene layer as transparent top electrode. The PL and Raman measurements show that the electronic structure and phonon spectrum in tri-layer MoS_2 can be smoothly modulated by strain ranging from 0 to 0.2 %, which are further confirmed by first-principles investigations. Surprisingly, the direct bandgap of tri-layer MoS_2 blue shifts remarkably by ~300 meV per 1% strain, which is unprecedentedly large among all bulk or nanostructure semiconductors under strain. Moreover, the PL intensity can be increased by 200 % accompanying with ~40 % reduction in the full-width-half-maximum (FWHM) of the emission spectrum for an applied strain of ~0.2 %. These results build up a platform generally applicable for strain engineering in the emerging 2D crystals such as transition metal dichalcogenides.

Although strain engineering in 2D materials can significantly enhance their electronic, photonic and spintronic performances, most of the strain engineering

techniques required external effort to apply strain onto the 2D materials. It will be of significance to develop a method to apply strain internally on arbitrary substrates so that the strain engineered 2D materials can be utilized for practical applications. By controlling evenly distributed strain, only the bandgap can be engineered. However, by controlling local strain, confinement potentials for excitons can also be engineered, with possibilities for trapping excitons for quantum optics and for efficient collection of solar energy. Recent discovery of semiconducting monolayer materials with a large direct band gap such as MoS_2 has open up a realm of electronic possibilities that have not been previously exploited in traditional thin film structured crystals, which allows the fabrication of conventional electronic devices. Simulation has reported that the mobility of monolayer MoS_2 can be tuned under strain. This could further increase the transistors performance of monolayer MoS_2. The large rupture strength of 2D crystals allows one to induce large local strains by bending or folding the material like a piece of paper, which allows it to bend to a large degree without breaking even it is free standing. Moreover, the direct nature of the band gap of monolayer MoS_2 allows tunable PL at visible wavelengths, which will be useful for the fabrication of conventional LEDs and photodetectors. These shifts have been well established in 2D materials phonon modes, allowing Raman spectroscopy to detect

and to estimate the strain applied.

Furthermore, we developed a completely new system that can apply continuous strain to any 2D materials with arbitrary substrates, using CVD grown monolayer MoS_2 as an example. We intentionally transfer monolayer MoS_2 onto inclined trenches with different sizes ranging from 5×5 to 20×20 μm^2 so as to produce continuous uniaxial strains. Trenches with different sizes are patterned using focused ion beam (FIB) system on arbitrary substrates before the transfer of MoS_2. Depending of the depth of the trenches, compressive and tensile strains are induced in the MoS_2. The applied strain is quantified by a combination of Raman and PL spectroscopies. The effect of the non-uniform strain on the bandgap is also spatially resolved. Experimental results show that the strain applied on the MoS_2 is localized in different areas of the patterned substrate. Raman shift in MoS_2 on trenches with various sizes varied from 1 to 12 cm^{-1}, whereas the PL peak shifts from 3 to 14 nm. This is due to the localized strains applied onto the MoS_2 in the patterned substrate. The high strain tunability of electronic band structure in 2D materials provides a wide range of applications in functional nanodevices and the developed methodology should be generally applicable to other 2D semiconductors.

1.2 Scope of this project

In this project, we have synthesized graphene and MoS_2 layered materials. Their electrical and optical properties are characterized. Graphene based FETs and MoS_2 based electromechanical device are demonstrated. The optical and structural properties of the strained MoS_2 are also studied.

In Chapter 2, the brief information of 2D materials is described, including the structural, optical, electrical properties of 2D materials. Also, the growth of 2D materials is described.

In Chapter 3, the experimental details are described; including the techniques for the optical and structural characterizations, such as x-ray diffraction (XRD), Raman spectroscopy, scanning electron microscopy (SEM), transmitting microscopy (TEM), focused ion beam (FIB) and photoluminescence (PL). The experimental setup and procedures for the growth of 2D materials are also described.

In Chapter 4, the synthesis and characterization of graphene by chemical vapor deposition (CVD) are described. Also, the fabrication of the ZnO nanomesh coated GFET and the properties of the ZnO nanomesh coated GFET will be discussed. It is

suggested that the fabrication of *n*- and *p*-type graphene based transistor devices is possible.

In Chapter 5, the synthesis and characterization of tri-layer MoS_2 are discussed. Also, the fabrication of the MoS_2 electromechanical device and the properties of the MoS_2 are described. It is suggested that strain engineering in MoS_2 is possible, which is suitable for the development of MoS_2 optoelectronic device applications.

In Chapter 6, the synthesis and characterization of strained monolayer MoS_2 are discussed. Also, the properties of the localized strain will be discussed. The strained MoS_2 may enhance the performance of electronic and optoelectronic devices.

In Chapter 7, the work in this thesis is concluded and the future work is discussed.

Chapter 2 Two-Dimensional Materials

2.1 Background

The requirements for more compact and powerful systems in electronic and optical devices have been growing since silicon has reached its limit. There are new branches of material researches in the development of nanoscale devices in order to make the devices smaller and more powerful. Two-dimensional (2D) materials have emerged as a powerful class of materials that are creating substantial opportunities for nanoscale photonic and electronic devices due to their unusual physical phenomena that occur when heat transport and charge transport is confined into a plane. Many 2D materials such as the layered metal dichalcogenides (LNDCs), copper oxides and iron pnictides possessed correlated electronic phenomena such as high-temperature superconductivity [1-3]. The discovery of monolayer graphene in 2004 by Novoselov and Geim has shown that it is possible to exfoliate stable, single-atom or single-polyhedral-thick 2D materials from van der Waals solids. At the same time [4], these materials can exhibit unique and fascinating physical and mechanical properties. Even at one-atom-thick, graphene is an excellent electronic and thermal conductor. For example, graphene-based materials have also been proposed for a vast majority of applications ranging from transparent conductors to thermal interface materials to

barristor transistor-like devices [5-7]. Since 2D materials are entirely surface area, its properties and reactivity profoundly depend on the substrate, its local electronic environment and mechanical deformations.

The past few years of researches have yielded many methods for synthesizing, transferring, detecting, characterizing, and manipulating the properties of layered van der Waals materials. There are many novel methods invented to synthesize 2D materials, including solution-based, solvothermal, and surface epitaxial approaches. These methods have unlashed the potential to create new van der Waals solids and single-layer-thick materials. This makes many novel materials that had only been existed in the realm of theory possible to utilize in experiment. These materials included group IV and II-VI semiconductors such as silicene and germanane. Similarly, the properties at the single layer are also distinct from the bulk just like graphene. Most importantly, these 2D materials can be restacked and integrated into composites for a wide range of applications.

However, the bandgap of the 2D materials are not large enough for some of the optoelectronic applications, which hinders the application of the 2D materials. Yet, various reports emphasize that the electronic structure of the 2D materials are

highly dependent on strain. The ability to continuously control the bandgap in optoelectronic materials in a low-cost manner is highly desirable for a wide range of energy and sensing applications. For example, the efficiency of photovoltaic devices comprising a single *p-n* junction is subject to a limited value because only a small portion of solar energy is absorbed. Therefore, it would be of significant importance to fine tune the bandgap within a single semiconducting material. This can be utilized by introducing continuous elastic strain on 2D materials. The key advantage of 2D materials in this area is that they can sustain a high enough elastic strain to induce sufficient changes to their physical properties before they deform plastically or break, which cannot be easily achieved by the bulk-scale materials.

2.2 Structure

There are two major classes of single- and few-layer 2D materials. The first one is the layered van der Waals solids. This is the well-known class of crystalline structures that can be exfoliated by Scotch tape method and become stable single- or few-layer structure. These crystal structures are made of neutral, single-atom-thick or polythedral-thick layers of atoms that be covalently or ionically connected with their neighbors within each layer by van der Waals bonding along the third axis. This allows the interlayer to be exfoliated mechanically by the Scotch tape method. Single- and

few-layer-thick 2D materials can be obtained by this way. The samples created by this method are the best for studying their properties because it is less destructive than other methods. Samples of around 10 μm^2 can be prepared easily by this method.

Single-layer graphene is a purely 2D material. Its lattice consists of only carbon atom at each corner with regular hexagons. The bond length between adjacent carbon atoms is 1.42 Å, which is denotes by L_b, where the lattice constant, a, is 2.46 Å (Fig. 2.1(a)). Large-area graphene is a semimetal with zero bandgap. Its valence and conduction bands are cone-shaped and meet each other at the K points of Brillouin zone (Fig. 2.1 (b)). Since the bandgap is zero, devices with channels made of large-area graphene cannot be switched off effectively and make it not suitable for logic applications. However, the bandgap of graphene can be increased by varying its band structure. There are three ways to do so: (1) constrain large-area graphene in one dimension to form graphene nanoribbons, (2) bias bilayer graphene and (3) apply strain to graphene.

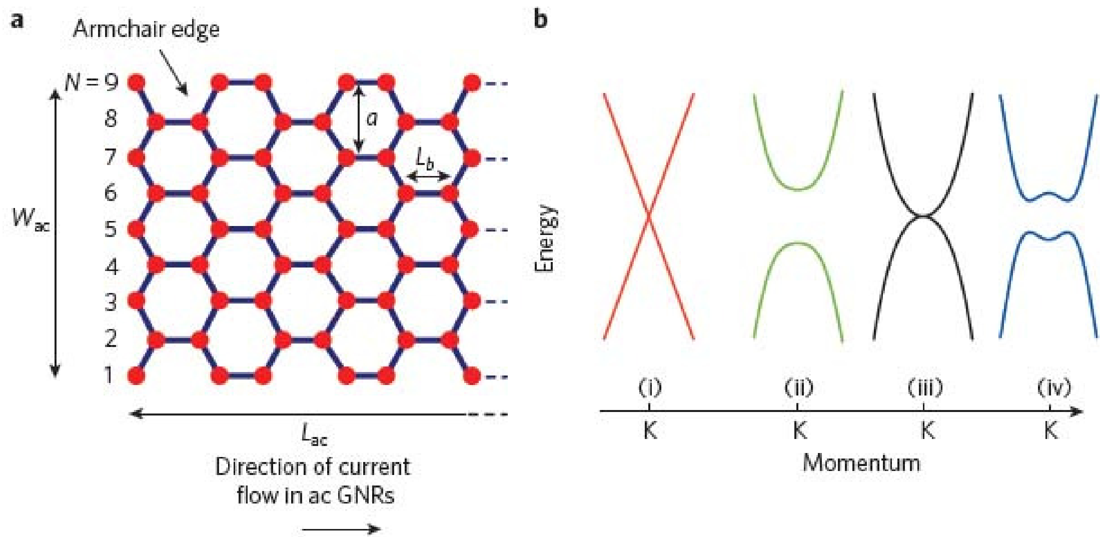

Fig. 2.1 Properties of graphene and graphene nanoribbons. (a)Schematic of an armchair (ac) graphene nanoribbon (GNR) of length L_{ac} and width W_{ac}. The nanoribbon shown here has $N = 9$ carbon atoms along its width and thus belongs to the 3*p* family, where *p* is an integer. (b)Band structure around the K point of (i)large-area graphene, (ii)graphene nanoribbons, (iii)unbiased bilayer graphene, and (iv)bilayer graphene with an applied perpendicular field. Large-area graphene and unbiased bilayer graphene do not have a bandgap, which makes them less useful for digital electronics [8].

Another most studied 2D materials is the layered metal chalcogenides (LMDCs), the most well-known being MoS_2. Most of the transition metal dichalcogenides with stoichiometry MX_2 (M = Ti, Zr, Hf, V, Nb, Ta, Re; X = S, Se, Te) crystallize into layered 2D structures in which hexagonally packed MX_6 octahedra (for d^0, d^3, and some d^1 metals) or trigonal prisms (for d^1 and d^2 metals) share edges with their six nearest MX_6 neighbors within each layers, which is shown in Fig. 2.2(a). For MoS_2, their honeycomb structure composed of staked S-Mo-S units. Two layers of sulphur atoms in a 2D hexagonal lattice are stacked over each other in an eclipsed fashion. Each Mo locates in the center of a trigonal prismatic cage surrounded by six sulphur atoms (Fig. 2.2(b)).

Because of the weak van der Waals interactions between the sheets of sulfide atoms, bulk MoS_2 has a low coefficient of friction, producing its lubricating properties. Meanwhile layered MoS_2 can be obtained by mechanical exfoliation.

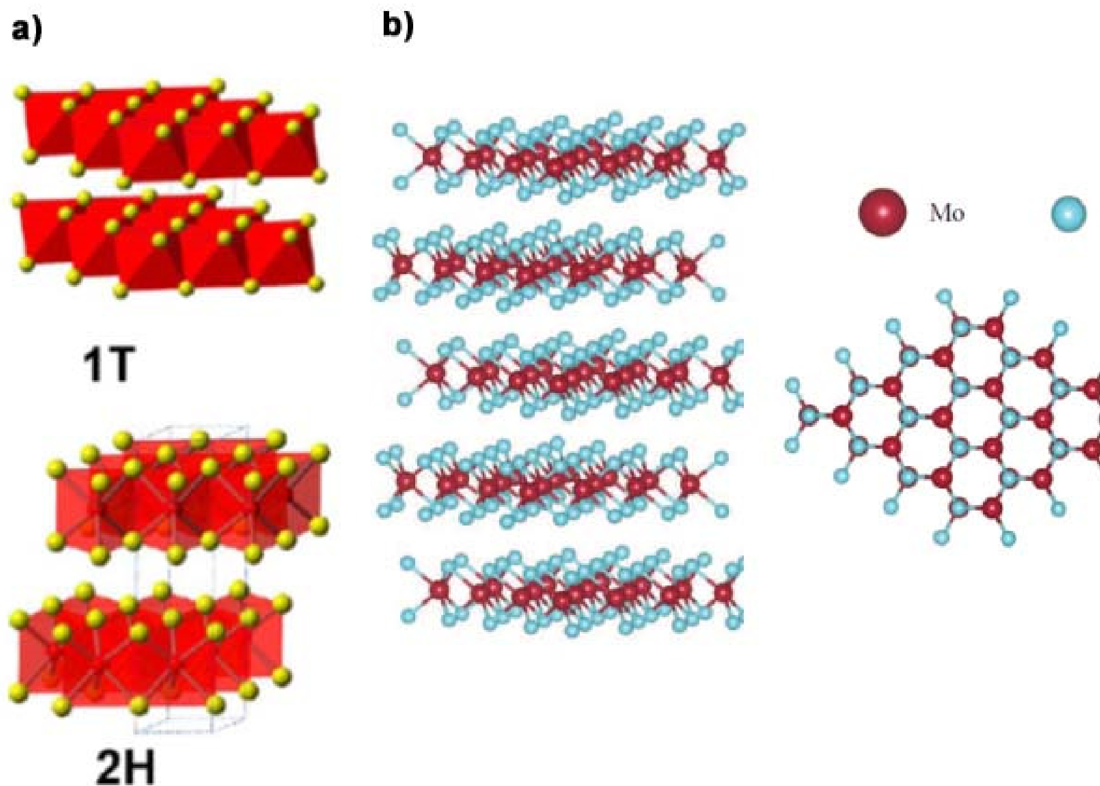

Fig. 2.2(a)Crystal structures of the 1T and 2H crystal structures of the MX_2 family (X = yellow sphere). The metal is in octahedral coordination in the 1T structure, and trigonal prismatic coordination in the two layers per unit cell 2H crystal structure [9]. (b)Crystal structure of MoS_2 [10].

2.3 Growth

2.3.1 CVD growth of graphene

The large-area growth of 2D materials is essential for commercialization and would also benefit fundamental studies of their phenomena. It is worthwhile to grow large area graphene by vapor deposition. By understanding the growth mechanism of

graphene, we can develop methods to grow other van der Waals 2D systems. The typical growth mechanism of CVD graphene is as shown in Fig. 2.3. Thin carbon films are originally grown on single-crystal transition metals such as copper and nickel by exposing the metal surface to a hydrocarbon source at high temperature (~1000 ^{o}C) in ultrahigh vacuum (UHV) conditions, or under the flow of hydrogen in low vacuum. The formation of graphene layers is due to the dissociation of the hydrocarbon on the metal surface, into which the carbon diffused and segregation during cooling or by carbon supersaturation. The dissociation of the hydrocarbon followed by carbon species diffusion on the surface leads to nucleation, island growth, and finally completion of a monolayer graphene. This is due to the extremely low carbon solubility in copper even at the growth temperature of ~1000 ^{o}C [11, 12].

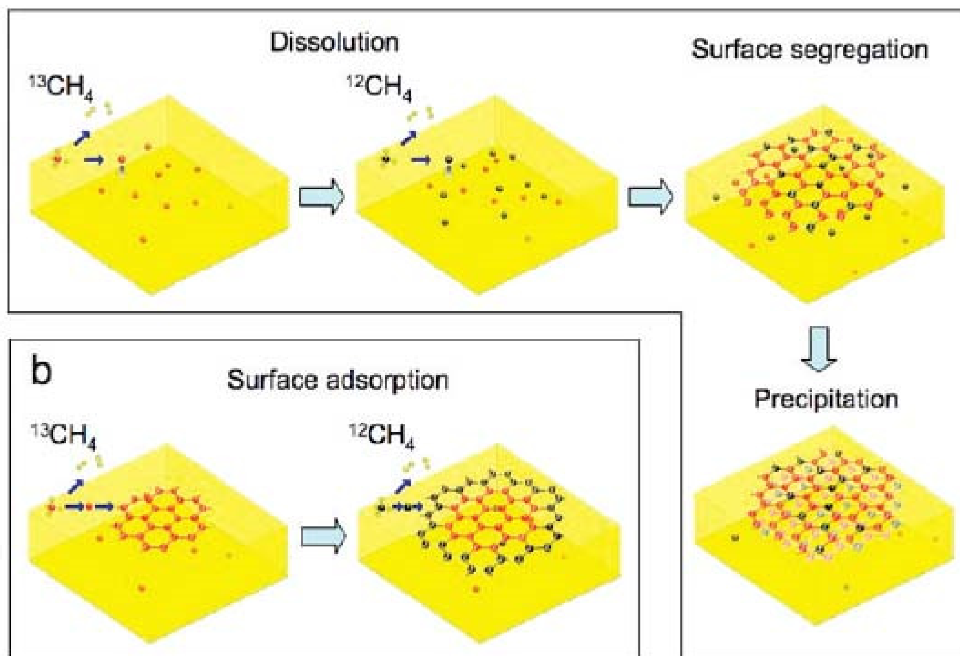

Fig. 2.3 Schematic illustration showing the dissociation-dissolution-segregation on Cu and the surface-mediated growth of monolayer graphene on Cu [11].

2.3.2 Growth of MoS_2

Growth of large area MoS_2 with seed layer by CVD: For the layered materials which are composed of two or more elements, the synthesis methods are usually more complex. For example, MoS_2 might be one of the most studied layered materials with two elements. The layered MoS_2 can be synthesized in CVD system (Fig. 2.4(a)) on single-crystal substrates, using MoO_3 and sulphur powder as precursors under flow of Ar as a carrier gas. The growth temperature was controlled at 650 ^{o}C. The process temperature profile is shown in Fig. 2.4(b). A continuous, large-area monolayer can be achieved using perylene-3,4,9,10-tetracarboxylic acid tetrapotassium salt (PTAS)

seeding promoters. MoS_2 particles are grown on the substrate instead if no PTAS is used (Fig. 2.4 (b)) [13].

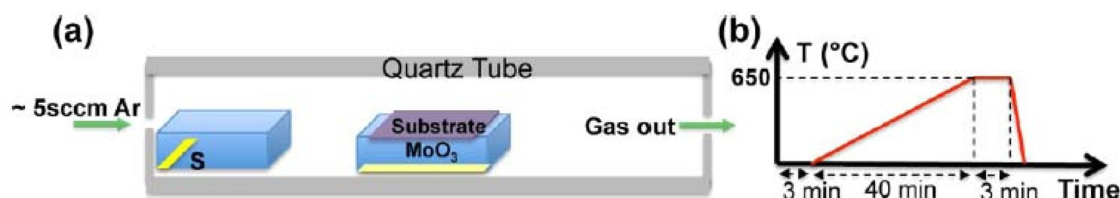

Fig. 2.4(a)A schematic illustration of the MoS_2 CVD system. (b)The temperature programming process used for a typical growth [13].

Growth of single crystal MoS_2 without seed layer by CVD: Fig. 2.5(a) schematically illustrates an experimental setup for the growth of MoS_2. MoO_3 powder is placed in an alumina boat at the center of a horizontal quartz tube furnace with 1 inch tube diameter. The insulating substrate is cleaned in acetone, isopropyl alcohol, and deionized water and is placed downstream far from the oven center in a cooler zone (at ~650 ^{o}C during growth). The tube is initially pumped to a base pressure of 20 mTorr and flushed with Ar carrier gas (~20 sccm) repeatedly at room temperature to remove oxygen contamination. With the carrier gas flowing and the pressure maintained at ~20 Torr, the furnace temperature is then increased to ~ 900 ^{o}C (~35 ^{o}C/min) and held there for 15-20 min before being allowed to cool naturally. Single crystals MoS_2 of triangular shape without extended defects or grain boundaries can be synthesized as shown in Fig. 2.5(b) and (c) [14].

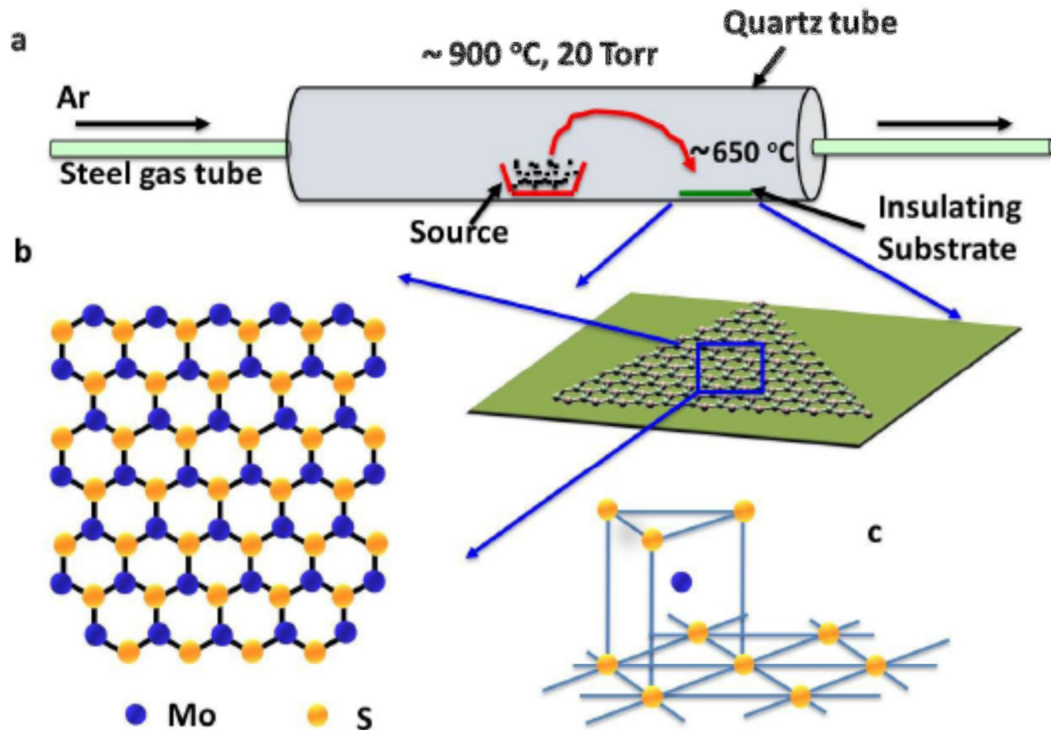

Fig. 2.5(a)Growth setup and conditions. (b)Cartoon indicating the structure of the triangular monolayer crystallites. (c)Structure of monolayer MoS_2 [14].

2.4 Electrical properties

The reduced dimensionality and symmetry of 2D materials lead to the appearance of the transformation of their band structures, as single layer is approached. Moreover, the interface between the surface and the substrate and the presence of adatoms and defects can dramatically alter the materials' inherent properties since a 2D material is merely made up of its surface. These materials possess high electron mobilities, topologically protected states, tunable band structures and high thermal conductivities. The development of 2D materials is expected to improve current device technology,

spintronic devices and quantum computing [15].

The 2D materials have two major advantages over bulk materials. The first advantage is that the 2D materials can approach the ideal effective screening length λ. To reduce the channel length in today's typical silicon-on-insulator transistors, the thickness of the semiconductor must be reduced to minimize the electrostatic screening effects [16]. This leaves 2D materials as the best candidates to make λ as small as possible, which is approximated by

$$\lambda = \sqrt{\frac{\varepsilon_{ox} d_s d_{ox}}{\varepsilon_{ox}}}$$

(Eq. 2.1)

Here, ε_s and d_s denote the dielectric constant and thickness of the semiconductor, respectively, and ε_{ox} and d_{ox} are the respective quantities for the dielectric oxide. In either case, minimizing d_s will minimize λ. Thus, single-layer-thick 2D materials represent the best possible scenario that nature has to offer [16].

The second advantage is that the 2D materials can be operated beyond the quantum capacitance limit (QCL). The limit at which the oxide capacitance is equal to the quantum capacitance, the capacitance due to gate-voltage-induced free charges in the channel [17]. In the QCL regime, the intrinsic gate delay (τ) is reduced, whereas the $P \cdot \tau$

(where *P* is the dynamic power) now decreases linearly with channel length in the QCL regime [17]. Therefore, the energy consumption required for switching is minimized in the QCL. For example, the bandgap of MoS_2 is larger than that of Si, this property could result in a much lower direct source-to-drain leakage current, which is especially important for transistors [18]. Fig. 2.6(a) shows a schematic diagram of a MoS_2 FET. The drain current (I_D) versus grate voltage (V_G) characteristic for a simulated MoS_2 transistor is shown in Fig. 2.6(b), giving an incredibly large ON/OFF ratio (~10^{10}).

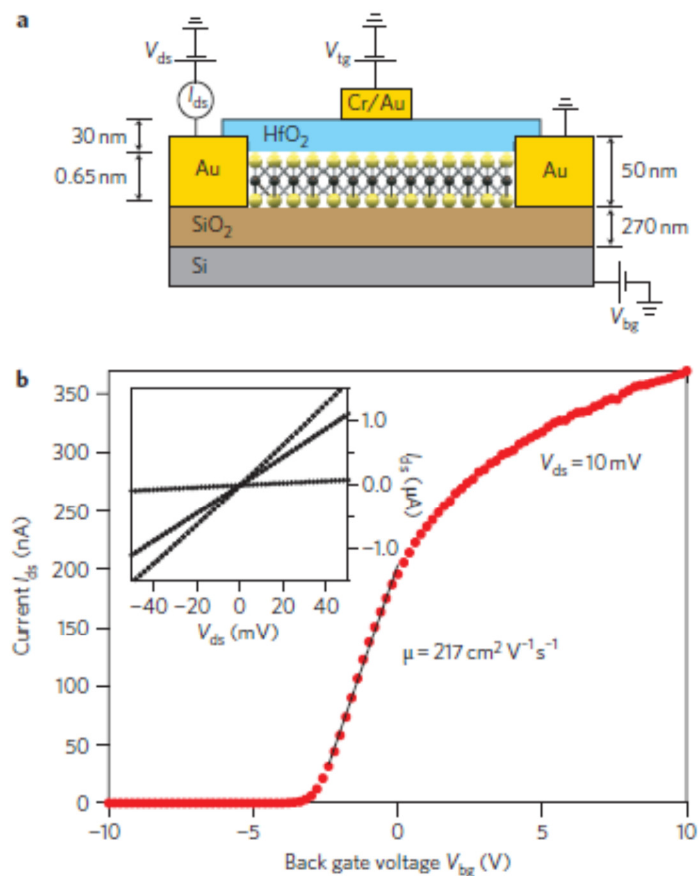

Fig. 2.6(a)Schematic illustration of cross section of MoS_2 FET. (b)Transfer characteristic of a monolayer MoS_2 transistor in linear scale [19].

2.5 Optical properties

The electronic structure of one of the LMDCs changes with the number of layers. The LMDCs shows diverse electronic properties ranging from metals to semiconductors to insulators. Moreover, they exhibit strongly correlated electron phenomena, such as charge density waves and superconductivity. Among them, MoS_2 has attracted the most attention due to its distinctive optical and transport characteristics [15, 20]. For example, the bandgap of MoS_2 can be changed from indirect to direct one when it scales down to monolayer [20]. With decreasing thickness, the indirect bandgap shifts upward by more than 0.6 eV, which are shown in Fig. 2.7(a) and (b). The change of band structure to direct transition increases the PL intensity of the sample, which is shown in Fig. 2.7(c).

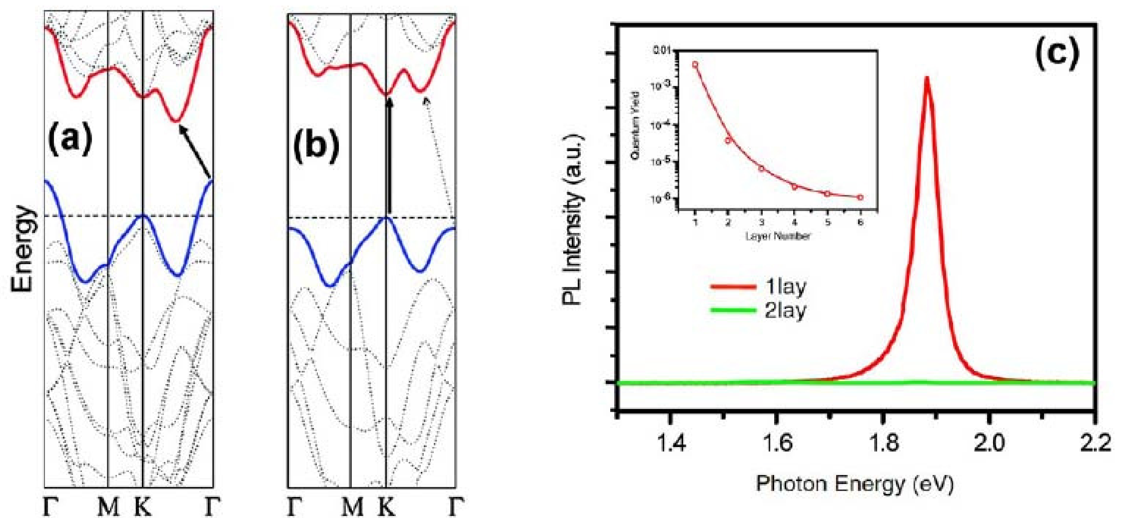

Fig. 2.7 Calculated band structures of (a)bulk and (b)monolayer MoS_2. The solid arrows indicate the lowest-energy transitions. (c)PL spectra for mono- and bilayer MoS_2 samples. Inset: PL quantum yield of thin layers of MoS_2 for number of layers N = 1–6 in log scale [20].

2.6 Strained properties

2.6.1 Theoretical prediction of strained behavior

It is proven theoretically that the electronic structure of MoS_2 can be changed upon the addition of strain. On the application of a biaxial strain, Poisson contraction is expected. Due to the symmetry of the hexagonal structure, the MoS_2 monolayer has isotropic in-plane elasticity. Thus, the bandgap depends only on the 2D hydrostatic strain invariant to the linear order. First-principles density functional theory (DFT) calculations indicate that both direct and indirect DFT bandgaps decrease. Therefore, a transition from direct bandgap to indirect bandgap occurs once the biaxial strain is applied. The change of bandgaps can be demonstrated by the change of excitation energy from 2.0 eV at zero strain to 1.1 eV at 9 % biaxial strain as shown in Fig. 2.8(a). Moreover, the quasiparticle energies are also reduced when the MoS_2 is under biaxial strain, which makes the strain-engineered MoS_2 applicable as solar energy funnel [21] (Fig. 2.8(b)).

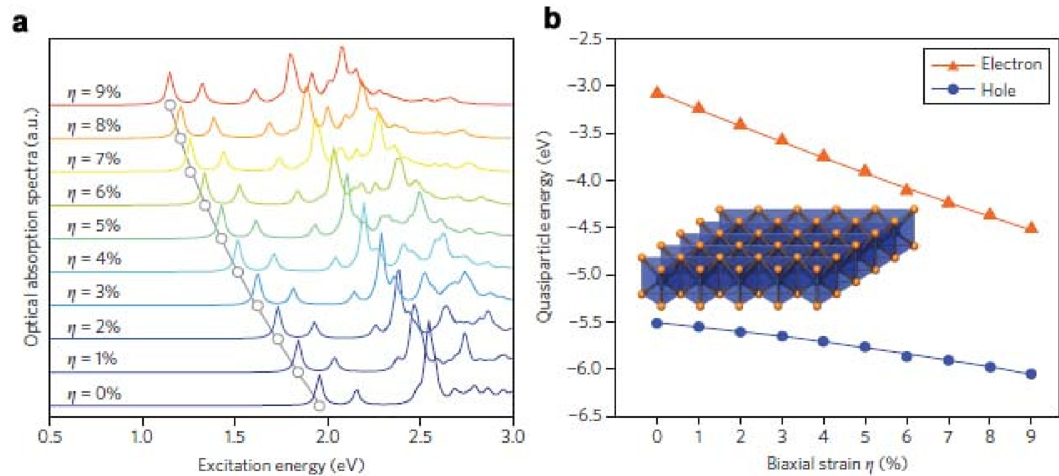

Fig. 2.8(a)Biaxial strain-dependent optical absorption spectra calculated. (b)Biaxial strain-dependent quasiparticle energies for electrons and holes at the K point. Inset: atomic structure of MoS_2 monolayer [21].

2.6.2 Local strain engineering

Localized uniaxial tensile strain up to 2.5 % in few-layer MoS_2 has been achieved in following way: (1) MoS_2 flakes are deposited onto an elastomeric substrate which is prestretched by 100%. (2) The tension in the substrate is suddenly released, generating well-aligned wrinkles in the MoS_2. Layers perpendicular to the initial uniaxial strain axis in the substrate are shown in Fig. 2.9(a). The corresponding Raman spectra measured on the flat region and on top of a wrinkle of a few-layer MoS_2 are shown in Fig. 2.9(b). Red-shifted E_{2g}^1 and A_{1g} modes are observed on top of the wrinkle, which represents a tensile strain. Not only do the Raman peaks experience a shift, but also do the PL spectra experience a shift due to the strain. The direct gap transition of the MoS_2 is shifted towards higher wavelengths, which is shown in Fig. 2.9(c). This indicates that

the uniaxial strain localized on the top of the wrinkle modifies the band structure, reducing the energy of the direct band gap transition.

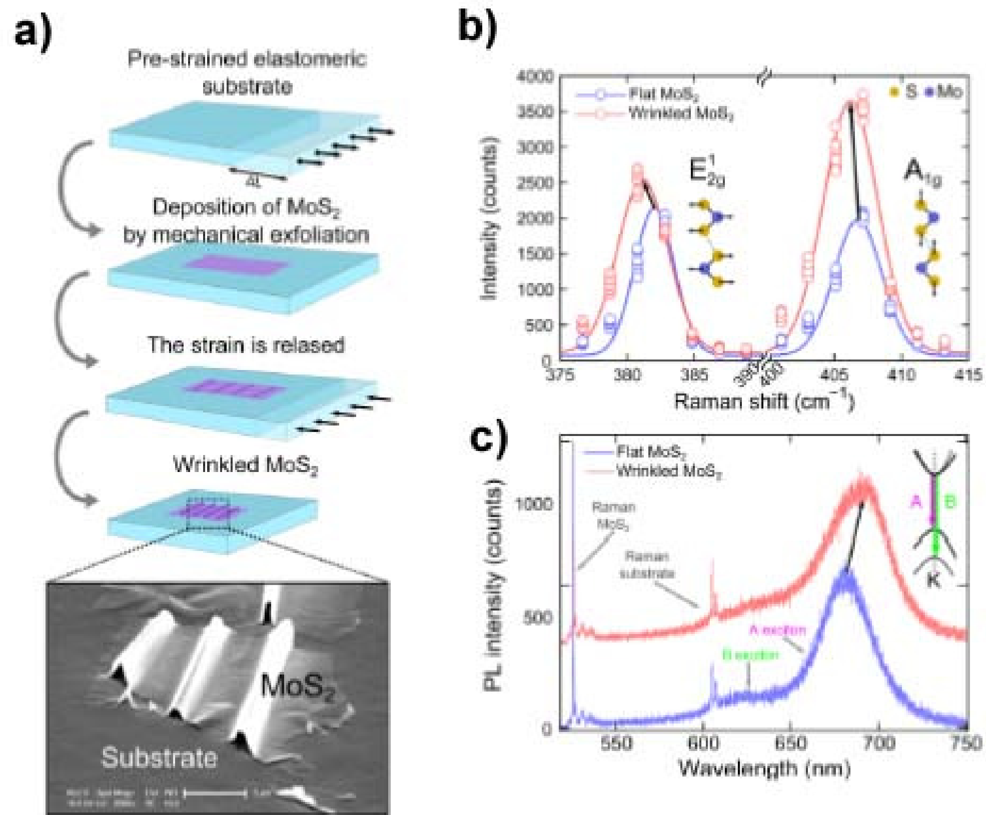

Fig. 2.9 Localized uniaxial strain in MoS_2. (a)Schematic diagram of the fabrication process of wrinkled MoS_2 monolayers. An elastomeric substrate is stretched prior depositing MoS_2 by mechanical exfoliation. The strain is released afterward, producing buckling-induced delamination of the MoS_2 flakes. (b)Raman spectra measured on a flat (blue) and on a wrinkled (red) region of a 40-layer-thick MoS_2 flake. Although both E_{2g}^{1} and A_{1g} modes are shifted towards a lower Raman shift, the E_{2g}^{1} presents the higher shift. (c)photoluminescence spectra measured on the flat region (blue) and on top of the wrinkle (red) in the same MoS_2 flake [22].

Chapter 3 Experimental Details

3.1 Growth of 2D materials and transfer process

3.1.1 Growth and transfer of graphene

The chemical vapor deposition (CVD) grown graphene was fabricated with typical process: (i)loading the quartz tube with Cu foil (25-μm thick, Alfa Aesar, item No. 13382); (ii)annealing the Cu foil to 1000 °C for 30 min with the flow of H_2(g)/Ar(g) at a flow rate of 10:50 SCCM (standard center cubic per minute); (iii)introduce CH_4(g) at 1000 °C for 10 min; (iv)after the reaction was completed, the quartz tube containing the Cu foil was pulled out of the hot zone from the furnace and cooled naturally under the flow of H_2(g)/Ar(g); (v)graphene films were spin-coated with a layer of poly-methyl methacrylate (PMMA) before the removal of the Cu foils by etching in an aqueous solution of iron chloride ($FeCl_3$) over night; (vi)after the Cu foil is dissolved, the PMMA coated graphene is subjected into cleaning with de-ionized (DI) water. Fig. 3.1 shows the schematic diagram of the CVD process.

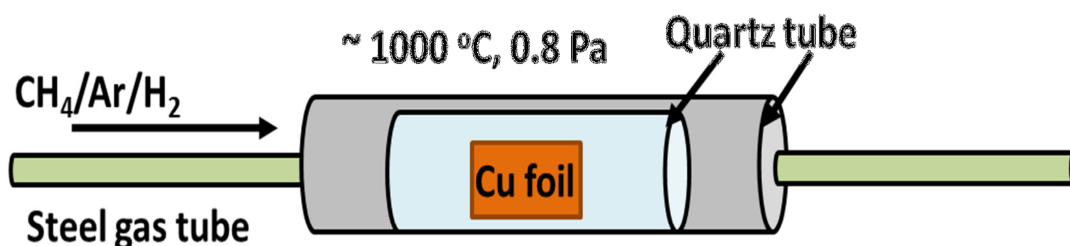

Fig. 3.1 Schematic diagram of a tube furnace used for synthesizing graphene.

3.1.2 Growth of tri-layer MoS_2

The preparation of the tri-layer MoS_2 was carried out in Dr Lain-Jong Li's group. The precursor $(NH_4)_2MoS_4$ was dip-coated on sapphire substrates followed by the two-step annealing process as shown in Fig. 3.2. The as-grown MoS_2 film can be transferred onto other arbitrary substrates. First, the dip-coated sapphire was annealed at 500 ^oC for 1 hr under the flow of Ar/H_2 (1 Torr). Second, the sample was then subjected to annealing temperature of 1000 ^oC for 30 min (500 Torr) under the flow of Ar gas.

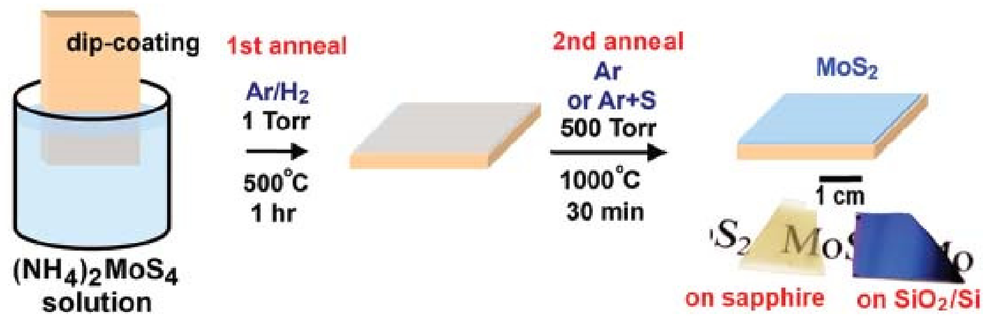

Fig. 3.2 Schematic illustration of the two-step thermolysis process for the synthesis of MoS_2 thin layers on insulating substrates [23].

3.1.3 Growth of monolayer MoS_2

The CVD grown of monolayer MoS_2 was fabricated with typical process as shown in Fig. 3.3: (i)load the rear side quartz boat with sapphire substrate (500-μm thick, 1 cm × 2 cm) and front side quartz boat with sulphur powder; (ii)heat up the sapphire substrate to 650 ^{o}C using heating element for 10 min with the flow of Ar(g) at a flow rate of 70 SCCM; (iii)heat up the sulphur powder to 200 ^{o}C using heating element for 10 min; (iv)after the reaction was completed, the cover of the tube furnace was opened and the quartz boat containing the sapphire substrate was cooled naturally under the flow of Ar(g); (v)MoS_2 films were spin-coated with a layer of PMMA before the removal of the sapphire by etching in an aqueous solution of sodium hydroxide (NaOH) with a concentration of 2 M for 1 hr at 100 ^{o}C; (vi)after the PMMA was detached from the sapphire substrate, the PMMA coated MoS_2 was subjected into cleaning with de-ionized (DI) water and

transferred to the desired substrate.

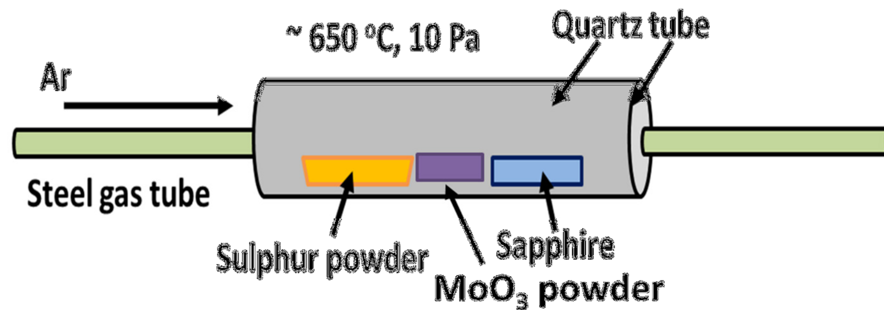

Fig. 3.3 Schematic diagram showing the CVD process to fabricate monolayer MoS_2

3.2 Structural characterization

3.2.1 X-ray diffraction (XRD)

X-ray diffraction (XRD) is a method to determine the arrangement of atoms within a crystal, which can be either single crystalline or polycrystalline structure. It works when an x-ray beam strikes into a crystal and diffracts into many specific directions, see Fig. 3.4. From the angles and intensities of these diffracted beams, a crystallographer of a certain material can be produced in a three-dimensional (3D) picture by reconstructing each unit cell within the crystal. From the XRD, the positions of the atoms in the crystal, chemical bonding and disordering can be determined. Another advantage of this method is that it is a non-destructive technique which reveals information regarding unit cell dimension, crystalline structure and phase identification of materials precisely. The structural properties of the 2D materials were characterized by a Bruker D8 Discover and

a Philip X'pert X-ray Diffractometer in a four-circle mode. The x-ray source gives out K_α radiation of copper (Cu) at wavelength of 1.54 Å [24].

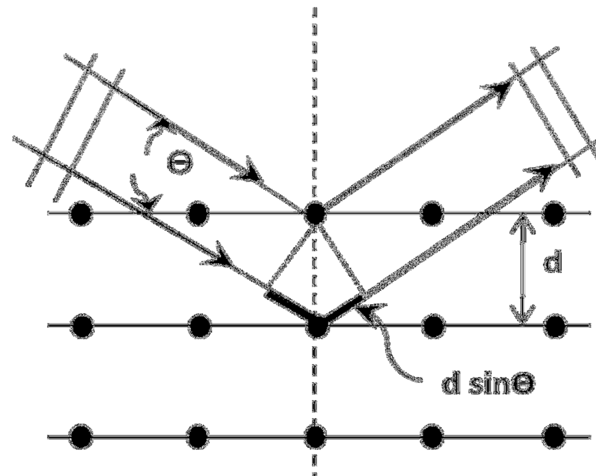

Fig. 3.4 Schematic diagram showing the principle of XRD.

The XRD works when there is a parallel monochromatic x-ray beam hitting on a sample, part of the beam will be diffracted by different crystal planes of the sample. The diffracted rays will interfere with each other to form diffraction centers and form constructive interferences in certain angles. These constructive diffraction interferences of the sample should obey the Bragg's Law:

$$2d_{hkl} \sin\theta = n\lambda \qquad \text{(Eq. 3.1)}$$

where d_{hkl} is the inter-planar spacing, n is an integer which represents the number of diffraction mode, θ is the angle of diffracted beam, λ is the wavelength of the incident x-ray beam. For a material with a cubic structure, the inter-planar spacing can de deduced from this equation:

$$d_{hkl} = \frac{a}{\sqrt{h^2+k^2+l^2}} \quad \text{(Eq. 3.2)}$$

where *h*, *k* and *l* are the Miller indices.

But for hexagonal structure, the formula should be the following:

$$\frac{1}{d_{hkl}} = \sqrt{\frac{4}{3}\left(\frac{h^2+k^2+l^2}{a^2}\right) + \frac{l^2}{c^2}} \quad \text{(Eq. 3.3)}$$

where *h*, *k* and *l* are the Miller indices.

Two different scanning modes, θ-2θ mode and rocking mode, were used to characterize the crystal structure of the 2D materials. The first mode is to identify the crystalline phases and orientation of the film. In this mode, the x-ray source is fixed, where the sample holder is moving in the speed of ω and the detector is moving in the speed 2ω. The second mode is the crystalline structure measurement of the sample by determining the full width half maximum (FWHM) from the rocking peak. In this mode, The x-ray source and detector are fixed at a selected angle, where the sample holder is rocked back and forth in a few degrees about the θ direction so as to obtain the crystallinity of the sample from the full width half maximum (FWHM) in the rocking curve [25].

3.2.2 Scanning Electron Microscopy (SEM)

Scanning electron microscopy (SEM) is a high resolution electron microscope that

is able to image the sample surface at a relatively larger area by scanning it with high-energy beam of electronsthat generated from an electron gun. The sample's surface topography, composition and other properties such as electrical conductivity can be obtained when the electrons from the electron gun interact with the atoms from the sample, which is shown in Fig. 3.5 [26].

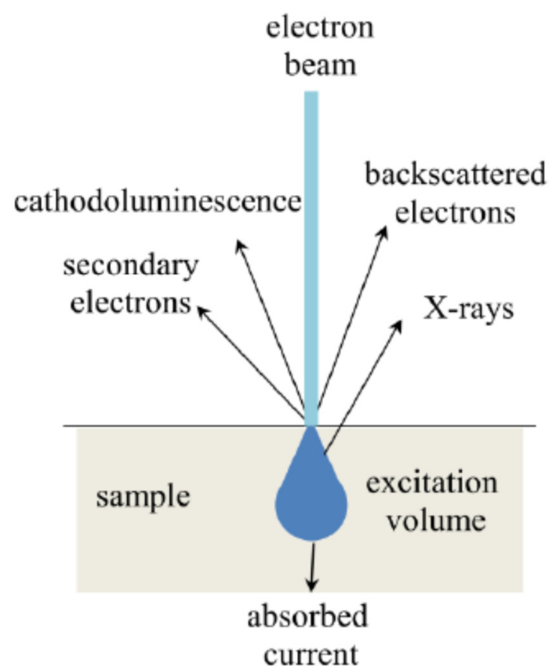

Fig. 3.5 Schematic diagram showing the principle of SEM.

Typically, there are several types of signals produced by SEM, including secondary electrons (SE), back-scatteredelectrons (BSE), cathodoluminescence (CL), characteristic x-rays, specimen current and transmitted electrons as shown in Fig. 3.5. Since the 2D materials can conduct electricity, gold coating of the samples is not necessary. Yet, higher

resolution image can be obtained if gold is coated onto the samples to reduce the localized charge up on the sample surface. All the samples were characterized by JSM-6335F Field Emission Scanning Electron Microscope by sticking them onto a conducting carbon tape.

3.2.3 Transmission electron microscopy (TEM)

Transmission electron microscopy (TEM) is a very high resolution microscope, having higher resolution than SEM, which depends on electron beam emitted from an electron gun to transmit through an ultra-thin sample (with a carbon grip underneath). The electron beam will be diffracted as it passes through the sample so that a diffraction image and crystalline structure image can be formed, which can be detected by a CCD sensor [27].

Transmission electron microscopy (TEM, JEOL JEM-2010) was used to determine the diffraction pattern, sample geometry, crystalline structure and the elements of the 2D materials. The diffraction patterns of the 2D materials were taken by selected area electron diffraction (SAED) method so as to obtain the diffraction pattern of a particular 2D material. Hence, the planar separation and the lattice constants of the 2D materials could be calculated. The sample geometries were taken with the typical TEM image to

study their lengths and diameters whereas the crystalline lattices were taken with the high-resolution TEM (HR-TEM) image to study their growth direction and the crystalline structures. Energy-dispersive x-ray spectroscopy (EDX) was used to determine the elements of the 2D materials. This is an analytical technique used for the elemental analysis or chemical characterization of a sample by analyzing the X-ray emitted from a sample when it is hit with an electron from the electron gun [28].

3.2.4 Raman spectroscopy

Raman scattering is a convenient and non-destructive characterization technique for chemical bonding identification, structural characterization, stress analysis and vibration mode detection. This technique bases on the inelastic scattering nature of visible, near ultraviolet and near infrared light. The Raman spectroscopy works when monochromatic light, usually from a visible laser, incidents on a molecule, it will interact with the electron cloud of that molecule and its bonding. The molecule will be excited to a virtual state by the incident photon. For spontaneous Raman effect, the excited molecule will relax to a lower or higher stationary state accompany with the emission of a photon as shown in. The shift in energy gives information about the phonon modes in the molecule. Therefore, by calculating the energy of the final state, the shift of energy of the initial state can be obtained as shown in Fig. 3.6. The

frequency shift is called Raman shift and can be described by the following equation:

$$|\hbar\omega_l - \hbar\omega_s| \qquad \text{Eq (3.4)}$$

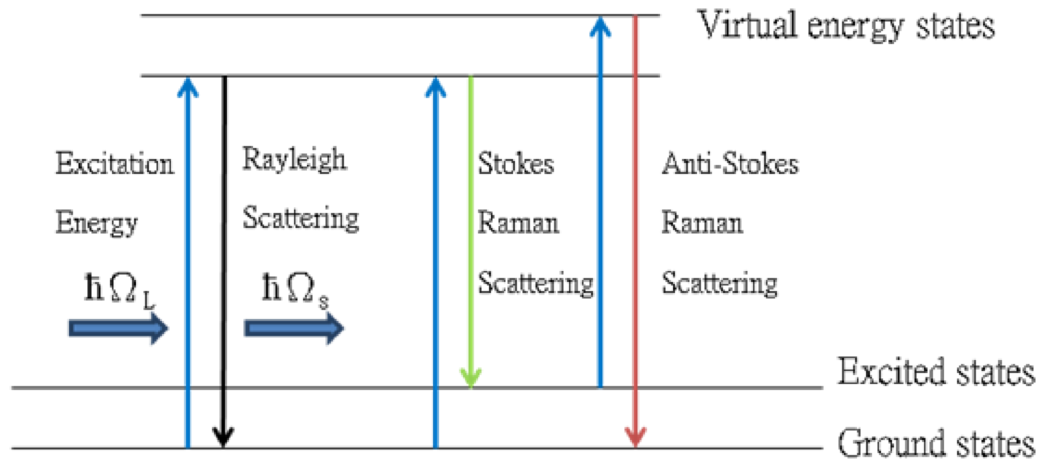

Fig. 3.6 Schematic diagram showing the principle of Raman scattering.

Horiba HR800 Raman microscope system was used to measure the Raman shift of the 2D materials. This spectrometer has a spectral resolution < 0.2 cm^{-1}, which embedded with a 488 nm Ar^+ laser as incident photons for the excitation of specimens. The emitted light from the sample is collected by a typical microscope via the 100× objective lens with a numerical aperture of 0.9 at room temperature. The spot size of ~1 μm with a laser power of 180 mW was used. For the Raman mapping, same parameters were used. The spatial resolution of 0.5 μm per step was used for the micro-Raman mapping.

3.3 Optical characterization

3.3.1 Photoluminescence (PL)

The Photoluminescence (PL) spectra of the 2D materials were measured by the same Raman system simultaneously. PL is a process that a semiconducting material absorbs photons generated by either a light source or laser source and then re-radiates photons of the same energy after an electron is excited from valence band to conduction band [29].

This is one of many forms of luminescences and is distinguished by photoexcitation, which the sample is excited by photon. The period between absorption and emission can be extremely short, for example, in an order of 10 nanoseconds. However, this period can be extended into minutes or hours under special circumstances [29]. It is an important technique to study the energy band structures of semiconductors by calculating their band energies from the emission wavelength with the following equations [30]:

$$E = hv \qquad \text{(Eq. 3.5)}$$

$$E = h\frac{c}{\lambda} \qquad \text{(Eq. 3.6)}$$

3.4 Substrate patterning

3.4.1 Focused ion beam

A Jeol JIB-4500 Focused Ion Beam (FIB) system was used to produce inclined trenches of different sizes on arbitrary substrates for the fabrication of strained 2D materials. FIB system operates in a similar way as a SEM does. Instead of a beam of electrons hitting on the sample, FIB uses a finely focused beam of ions, usually gallium, that can be operated at different beam currents for imaging, sputtering or milling. Usually a high beam current will be used for milling and sputtering.

As shown in Fig. 3.7, the gallium (Ga^+) primary ion beam hits the substrate surface and sputters a small amount of substrate based material, which leaves the surface as either secondary ions (i^+ or i^-) or neutral atoms (n^0). The primary beam also produces secondary electrons (e^-). When the primary beam tasters on the substrate surface, the signal from the secondary electrons or sputtered ions is collected to form an image.

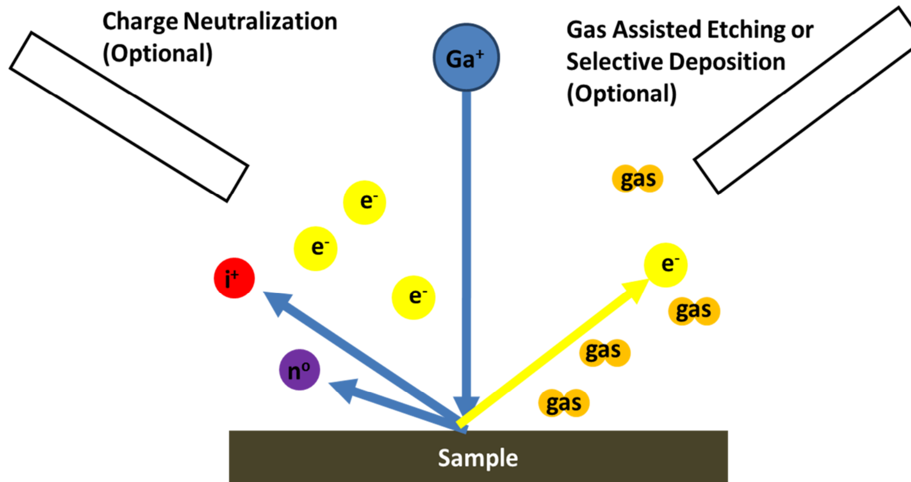

Fig. 3.7 Schematic diagram showing the principle of FIB.

Chapter 4 Graphene Field Effect Transistors

4.1 Introduction

Graphene has attracted much attention not only because of its perfect two-dimensional carbon crystalline structure, but also its potential in post-silicon nanoelectronics [4, 31, 32]. Single-layer graphene is sensitive to surrounding environment and its electronic properties can be significantly affected by interface and surface effects induced by underlying substrates [33], surface charges [34, 35] and adsorbed gas molecules [36]. Several concepts of extrinsic doping on graphene surface have been proposed such as depositing nanoparticles and chemical doping using thionyl chloride and aromatic molecules to modulate its electronic structure, which give rise to significant changes in electrical properties and Raman spectra [37-39]. Therefore, the realization of enhanced performance and controllable graphene based field-effect transistors (GFETs) has opened up new and interesting physics [40-46]. The understanding and quantifying the influence of immediate environment on graphene is of significant importance. This could be done by accurately controlling the surface dopants on graphene surface to utilize controllable *n*- and *p*-type GFETs. The method of patterning a semiconductor array on graphene surface could be one of the possible methods to control the surface dopants and fabricate controllable *n*- and *p*-type GFETs.

In order to fully explore the potentials of GFETs, the removal of contamination on graphene surfaces by thermal annealing to restore its clean surfaces is of central importance. Recently, a wide range of annealing conditions has been reported along with diverse thermal effects on GFETs [36, 39]. Yet, there is a common problem that although the contaminant can be eliminated upon annealing at temperature higher than 200 ^{o}C, it simultaneously brings graphene in close contact with corrugated SiO_2 substrates. Accordingly it induces large perturbation to the electrical properties of graphene devices and leads to degradation of electrical performance, which is inevitable [33]. However, there are still no solutions to eliminate the effect of thermal strain from the substrate.

The realization of *n*- and *p*-type GFETs by controlling merely the thickness of zinc oxide (ZnO) nanomesh deposited on the graphene has been demonstrated. The effect of thermal strain acting on the graphene by the substrate could be minimized for the devices that were covered with a layer of ZnO nanomesh. No further shifts of charge neutrality point (CNP) could be observed even the GFETs were subjected to annealing temperature of 400 ^{o}C. This suggests that the thermal stability of the ZnO nanomesh coated GFETs could be enhanced significantly. Besides, we note

that the quality, cleanness and flatness of the single-layer graphene were of significant importance to influence the quality of the ZnO nanomesh which in turn affected the *n*- and *p*-type doping of the GFETs. We also demonstrated that the electronic structure of the single-layer graphene could be differentially modulated by controlling the thickness of the ZnO nanomesh upon the graphene surface. The *n*- and *p*-type behavior of the GFETs could be explained by spectroscopic methods based on Raman D-band frequency sampling and by the transfer characteristics [47].

4.2 Experiment

Fabrication of ZnO nanomesh coated GFET: The fabrication process is shown by Fig. 4.1. To fabricate the ZnO nanomesh coated GFETs, *p*-doped silicon (Si) wafers covered with 300 nm thermally grown silicon dioxide (SiO_2) were used as substrate. The substrate was cleaned by standard method with acetone, isopropyl alcohol (IPA), DI water prior to the treatment with oxygen (O_2) plasma for 5 min. Subsequently, the CVD grown graphene was transferred on top of the cleaned substrate. The single-layer graphene was identified using optical microscopy. Monolayer polystyrene (PS) spheres with diameter of 500 nm were deposited on the graphene by allowing them to self-assemble on the graphene/SiO_2/Si substrate

via a dip-coating method [48]. Subsequently, the samples were subjected to the deposition of ZnO by the filtered cathodic vacuum arc (FCVA) technique at room temperature [49]. After the removal of the PS spheres by chloroform, the Au electrodes were fabricated by photolithography and thermo-evaporation, using lift-off method.

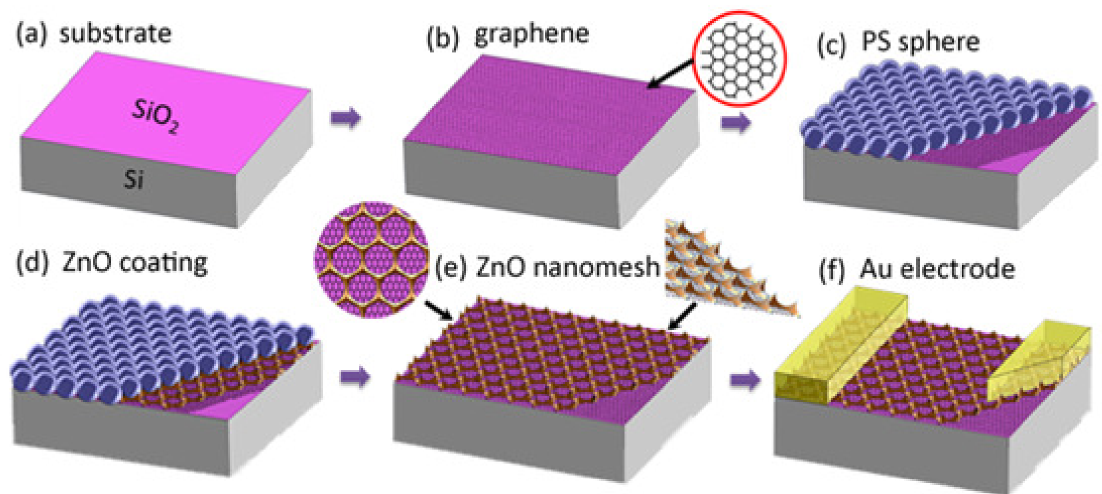

Fig. 4.1 Schematic diagram showing the fabrication process of a ZnO nanomesh coated GFET. (a)Preparation of clean hydrophilic SiO_2 (300nm)/Si substrate. (b)Transfer of CVD grown graphene. (c)Coating of monolayer PS spheres on graphene. (d)Deposition of ZnO film on PS spheres coated graphene. (e)Removal of PS spheres by chloroform for the formation of ZnO nanomesh. (f)Deposition of Au electrodes by optical lithography.

Characterization methods: The thickness of the as-fabricated ZnO nanomesh was measured by atomic force microscopy (AFM, DI Nanocope 8). The electrodes for both drain and source were made by thermally evaporating gold (Au) with thickness of 150 nm. The channel length and width of the devices were 5 μm and 2

mm respectively. Silver (Ag) paste was used as the electrode for bottom gate. Prior to the electrical measurement, the devices were annealed at 200 ^{o}C for 15 min to improve the contact resistance between Au and the samples. A HP 4156c semiconductor parameter analyzer was used to determine the transfer characteristics of the devices. The samples were characterized in a quasi-four probe configuration with invasive contact electrodes in a glove box filled with N_2. The transfer curves were measured at a constant source drain voltage of 0.05 V at room temperature with a V_G step of 10V.

4.3 Results and Discussion

4.3.1 Structural Properties of Graphene

Fig. 4.2(a) shows the difference between as-received Cu foil and the Cu foil covered with graphene. It is found that the Cu foil with graphene on it shows darker color when compared to the as-received Cu and the surface becomes shinier. Fig. 4.2(b) shows a transferred graphene on top of a Si substrate with 300 nm thick of SiO_2. Graphene appears to be invisible in most of the substrates. Only Si substrate with a thickness of 300 nm SiO_2 can make graphene visible due to the feeble interference-like contrast with respect to an empty wafer. Graphene appears to be dark purple when compare the light purple of the bare substrate. If we observe

graphene with an optical microscope, we can easily find some PMMA residue on it if the cleaning process is not complete as shown in Fig. 4.2(c). Optical image of a clean graphene should show uniform color as shown in Fig. 4.2(d).

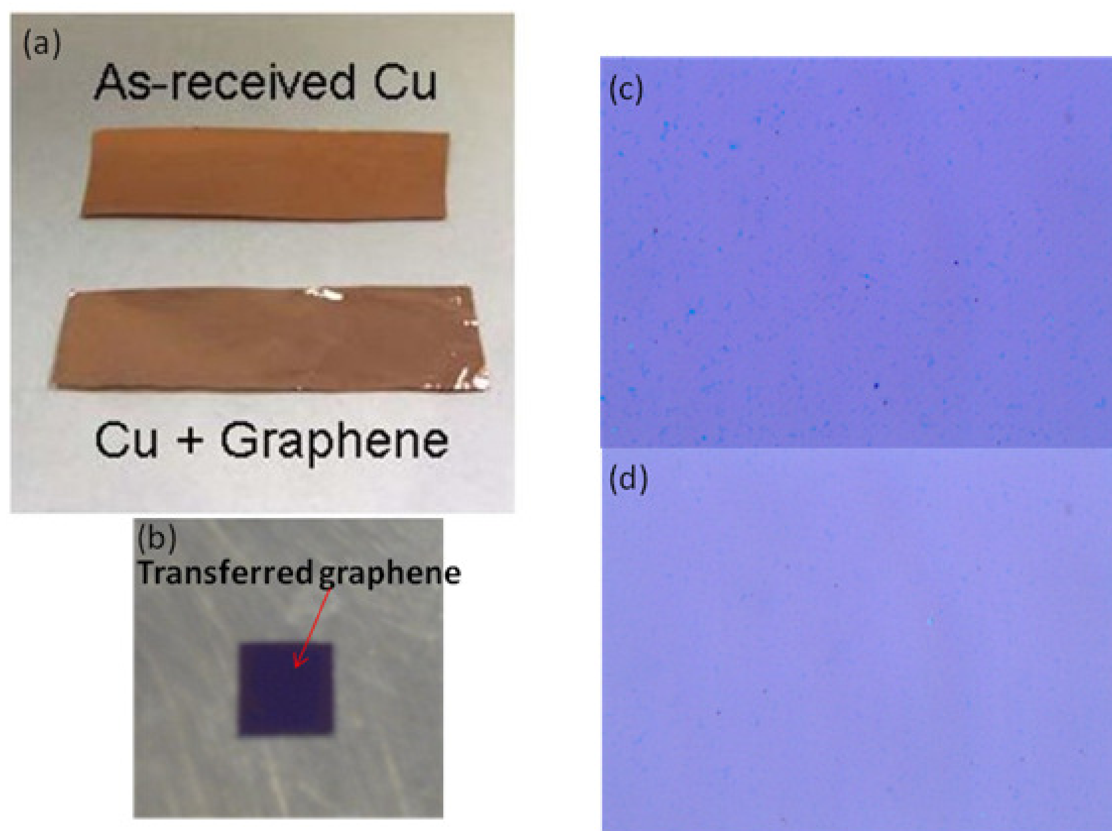

Fig. 4.2(a) Comparison between as-received Cu foil and graphene covered Cu foil. (b)A transferred graphene on a Si substrate with 300 nm thick of SiO_2 on top. (c)Optical image of a graphene covered with some PMMA residue. (d)Optical image of a graphene with a clean surface.

The number of layers of graphene can be determined by Raman spectroscopy. This technique is useful for quick inspection of graphene thickness. For bilayer graphene grown by CVD method, the G and 2D peak are found be 1:1 in ratio. For

single layer graphene, the G and 2D peak intensity are found to be 1:2 in ratio as shown in Fig. 4.3(a) and (b) respectively. Sometimes it is time consuming to transfer the graphene onto Si substrate. Therefore, it is useful to determine the number of layers of graphene on Cu foil by Raman spectroscopy. Fig. 4.3(c) and (d) shows the different between the Raman peak for a graphene on a Cu foil and on Si substrate. Although the peak intensity is much lower for the graphene grown on Cu foil, the G and 2D peak ratio remains the same before and after transfer. Therefore, it is still relevant to determine the number of layers of graphene on Cu foil.

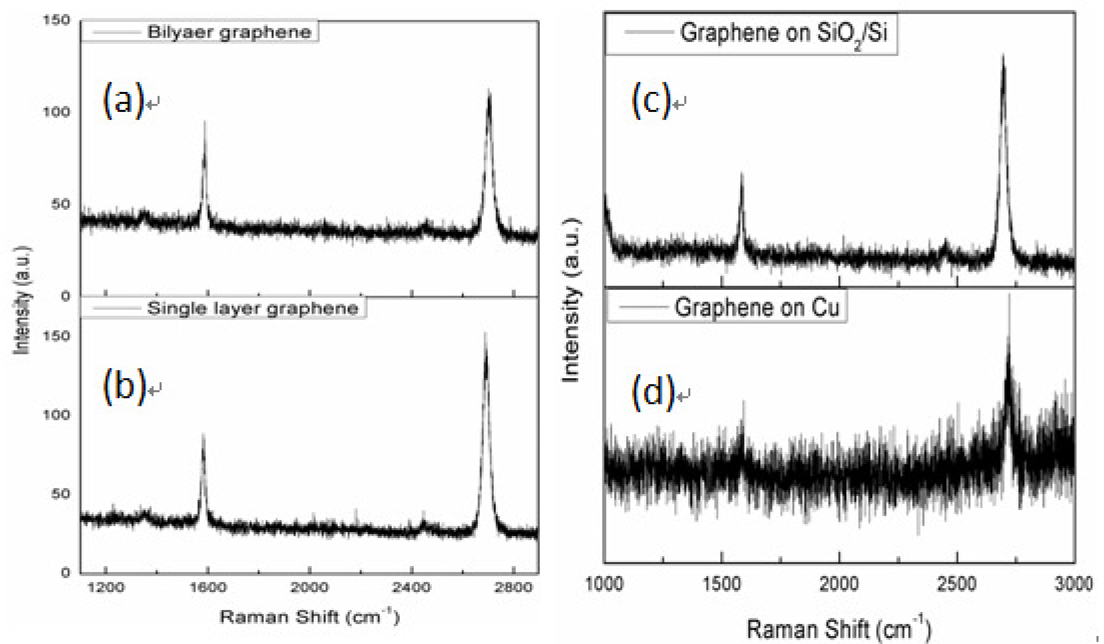

Fig. 4.3 Raman spectra of (a)bilayer graphene, (b)single layer graphene, (c)graphene on SiO_2/Si and (d)graphene on Cu.

4.3.2 Characterization of ZnO nanomesh Coated Graphene

Fig. 4.4(a-d) shows the scanning electron microscopy (SEM) images of a ZnO nanomesh coated GFET at various fabrication stages. Monolayer of PS spheres with the diameter of 500 nm was coated regularly onto the graphene surface (Fig. 4.4(a)). After the deposition of the ZnO, PS sphere array remained (Fig. 4.4(b)) [50]. Fig. 4.4(c) shows the formation of the ZnO nanomesh on the graphene after the removal of PS spheres. We note that this step is crucial because not only chloroform could remove the PS spheres, but also it can remove other impurities on the graphene surface. Fig. 4.4(d) gives the surface morphology of the ZnO nanomesh coated graphene with the gold electrode separation of 5 μm. To further investigate the surface morphology of the corresponding device, AFM was carried out. As shown in Fig. 4.4(e), a regular hexagonal structure of ZnO nanomesh is observed from the surface of the graphene. The thickness of the ZnO nanomesh coated GFET is 17 nm.

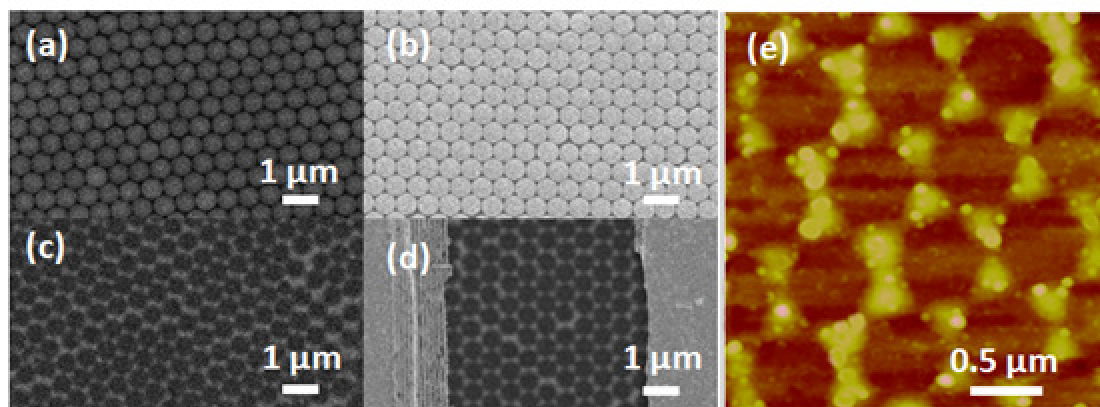

Fig. 4.4 SEM images of (a)PS spheres coated graphene, (b)ZnO deposited PS spheres/graphene, (c)ZnO nanomesh coated graphene and (d)ZnO nanomesh coated graphene device with Au electrode separation of 5 µm. (e)AFM image of the 17 nm thick ZnO nanomesh coated on graphene.

4.3.3 Field Effect Transistor characteristics

When the GFETs were coated by a thin layer (~17 nm) of ZnO nanomesh, the GFETs exhibited *n*-type behavior. It is worth noting that the GFET also exhibits *n*-type behavior if the ZnO nanomesh is around 10 nm but the ZnO nanomesh is not homogenously deposited on the graphene. When the ZnO nanomesh reached the thickness of 24 nm, the GFETs became *p*-type. However, it is difficult to remove the PS spheres completely when the ZnO is thicker than 24 nm, whereas the ZnO nanomesh is not in perfect hexagonal shape when the ZnO is thinner than 17 nm. Thus, we will only discuss the optimized GFET samples with thickness of 17 and 24 nm. To ensure that the observed effect was related to the ZnO nanomesh on the graphene but not the impurities from the atmosphere, the GFETs were

annealed together at several temperatures under nitrogen (N_2) ambient to remove the contaminations of water moisture and oxygen molecules adhered to the graphene surface [36]. All the devices were annealed consecutively *in-situ* at 100 and 200 °C. The electrical performances of the devices upon stepwise annealing are shown in Fig. 4.5 (a)-(c). After the thermal annealing, not only the CNP of the devices shifts toward the left, but also the conductivity of the CNP decreases. The source drain current (I_{DS}) at the charge neutrality point voltage (V_{CNP}) reduced from 5.2 to 2.4 mA, 6 to 2 mA and 0.8 to 0.3 mA for *n*-type, pristine and *p*-type devices respectively. It is well known that the water moisture and oxygen contamination from air could lead to an increase of conductivity for the single-layer graphene at the CNP [33]. Therefore, after the removal of contaminants on the surface of the graphene, the conductivity of the devices was reduced [39]. The CNP of the *n*-type (Fig. 4.5(a)), pristine (Fig. 4.5(b)) and *p*-type (Fig. 4.5(c)) devices was located at -16, 0 and +15 V respectively. As the CNP of the pristine graphene was shifted toward zero back gate bias (V_G) when the annealing temperature reached 200 °C [40], the *n*- and *p*-type GFETs were also subjected to the annealing temperature of 200 °C.

Although there was a drop of on/off ratio for the *n*-type device when compared

with the pristine device, the field effect mobility $\mu = [L/(WC_{OX}V_{SD})][d(I_{SD})/d(V_G)]$ of the *n*-type device did not change much and remain in the same range as the pristine device, approximately from 110 to 330 $cm^2/(Vs)$ [51, 52]. The source drain voltage (V_{DS}) was fixed at 0.05 V. This relatively low mobility obtained from the CVD grown graphene compared with the exfoliated graphene could be due to the contact resistance, surface impurities and the residue of PMMA left on the graphene surface [42, 53, 54]. The *n*-type field effect behavior of the device could be due to the doping of the *n*-type ZnO nanomesh. Since the conduction band of ZnO is located at -4.38 eV and it is intrinsically *n*-type, whereas the Fermi level of the pristine graphene is located at about -4.6 eV, it is possible that the electrons can move from the ZnO nanomesh to the graphene [55, 56]. Here C_{OX} denoted the back gate capacitance per area (11.5 $nFcm^{-2}$ for our devices). Exceptionally, there was a drop in mobility and conductivity for the *p*-type devices, having a mobility ranging from 20-60 $cm^2/(Vs)$. The appearance of the D peak is the main reason for the reduction in the conductivity for the *p*-type GFET. Moreover, based on the I_{DS}-V_G curves in Fig. 4.5(d), the excess electron and hole concentration $n_{ex\text{-}h} = (\varepsilon_o\varepsilon_r/ed_{ox})\Delta V_{CNP}$ of the *n*- and *p*-type GFETs were calculated to be 1.15 $\times 10^{12}$ and 7.86 $\times 10^{11}$ cm^{-2} respectively with $\varepsilon_r = 3.9$ and $d_{ox} = 300$ nm [57-59]. It should be noted that no CNP could be observed from the device covered by the ZnO thin film

without mesh-like structure. The device characteristics of the ZnO coated GFET will be dominated by the ZnO rather than graphene. Thus, ZnO nanomesh plays an important role in the characteristics of the GFETs.

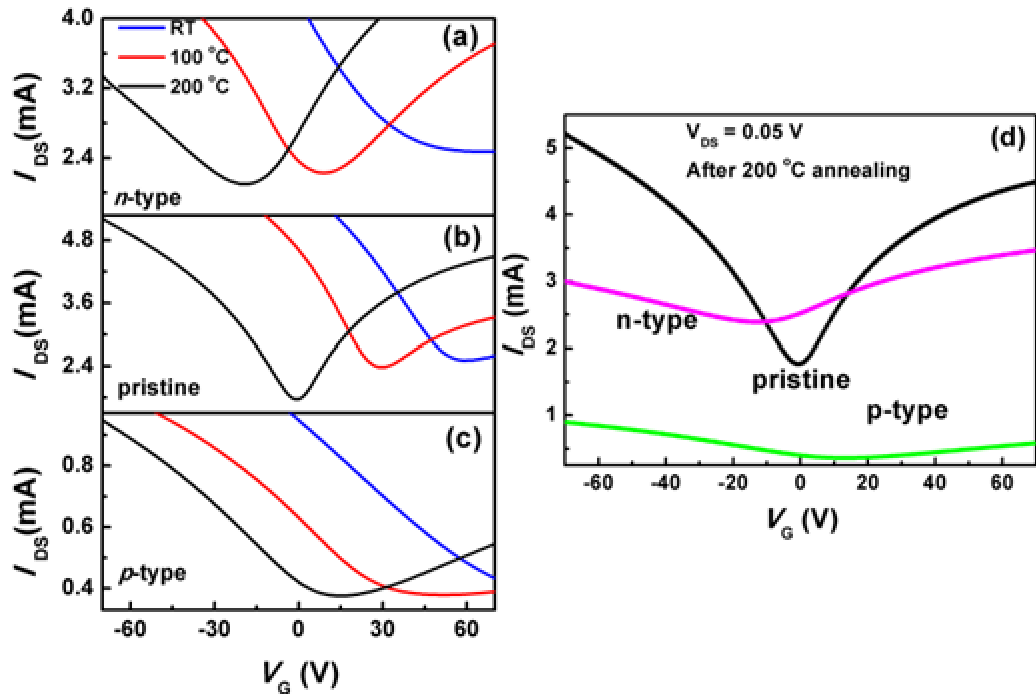

Fig. 4.5 Transfer characteristics of (a)*n*-type, (b)pristine and (c)*p*-type GFETs before annealing (blue lines) and after subsequent annealing at 100 (red lines) and 200 ^{o}C (black lines) in N_2 atmosphere, which were measured at room temperature. (d)Transfer characteristic of the 200 ^{o}C annealed *n*-type, pristine and *p*-type GFETs measured at room temperature. These devices were measured with the applied V_{DS} of 0.05 V.

Fig. 4.5(d) shows the transfer characteristics of the GFETs coated with different thicknesses of the ZnO nanomesh at room temperature after the devices annealed at 200 ^{o}C for 15 min [39]. The GFETs had a channel length of 5 μm and width of 2 mm. In each curve, the V_{DS} was fixed at 0.05 V and the V_G was scanned from -70 V

to 70 V at steps of 1 V. The effect of the ZnO nanomesh on the CNP and conductivity become obvious when the transfer curve of the *n*-type, pristine and *p*-type GFETs are plotted together as shown in Fig. 4.5(d). The transfer characteristic of the pristine device is a typical GFET, which exhibits minimum conductivity at the CNP, locating at zero V_G [8]. After the deposition of the ZnO nanomesh layer with thicknesses of 17 and 24 nm on top of the graphene, *n*- and *p*-type GFETs can be observed respectively. For the GFET with 17 nm thick ZnO nanomesh, the CNP of the GFET is shifted to -16 V and conductivity of the device at the CNP is also increased. However, the GFET with 24 nm thick ZnO nanomesh coated GFET exhibits *p*-type characteristic as the CNP is shifted to +15 V. Moreover, there is a change in conductivity at the CNP for different types of GFETs. For the *n*-type GFET, the conductivity at CNP is increased. On the contrary, the conductivity at CNP for the *p*-type GFET is decreased when compared with the pristine GFET.

4.3.4 Raman characteristics

Raman spectroscopy is an important tool to differentiate the number of layers of graphene by means of inelastic light scattering. This can be done by comparing the ratio of the graphitic (G) band which appears at 1591 cm^{-1} and the 2D band

locating at 2700 cm^{-1} as shown in Fig. 4.6(a), which comes from the second-order Raman scattering near the boundary of the Brillouin zone of graphene. To understand the effect of the ZnO nanomesh on the GFETs, Raman spectroscopy of each device was investigated [60]. The Raman spectra of the GFETs were obtained by directing the laser beam onto the channel (7μm) of the GFET. Since the channel size is comparable to the laser beam profile and the open-structure of the ZnO nanomesh does not cover the entire surface of the graphene, the corresponding Raman spectra can be obtained. As observed from Fig. 4.6(a), the G/2D ratio of all the *n*-type, pristine and *p*-type GFETs are smaller than 0.5, which imply that all the layers are single-layer graphene. The absence of splitting in the 2D band indicates that there are no negative effects on the number of graphene layers for the decorated graphene [61]. Since O_2 plasma exposure of the graphene surface is inevitable during the growth of ZnO nanomesh, D band can be observed from the decorated graphenes. The shape of the Raman spectrum of the *n*-type GFET is similar to the pristine GFET, except that the D peak increases slightly. As for the *p*-type GFET, the D band is increased substantially from the sample**.** This sample was covered by a 24 nm thick ZnO nanomesh which was exposed longer time (~5 min) to the oxygen plasma as compared with the *n*-type GFET that was covered by a 17 nm thick ZnO nanomesh (~3 min). Thus the substantial increase in the D peak

is attributed to the extensive O_2 plasma exposure during the deposition of ZnO nanomesh. In turn, oxygen-related defect sites were generated in the graphene surface which led to *p*-type GFET. The defects could not be annealed out even at the annealing temperature of 400 ^{o}C in N_2 environment, which are doped permanently on the graphene layer [62].

Electron (*n*-type) and hole (*p*-type) doping not only introduce different shifts in V_{CNP} but also have distinct effects on the Raman modes of the ZnO nanomesh coated GFETs. The blue- and red- shifts of G and 2D bands can be attributed to the hole and electron dopings respectively [63]. In Fig. 4.6(b) and 4.6(c), red- and blue-shifts can be obtained from the 10 and 17 nm thick ZnO nanomesh coated GFETs respectively, which corresponds to *n*- and *p*-type GFETs. The ZnO nanomesh can alter the CNP point of GFETs while keeping the other properties of graphene unchanged. Therefore, we believe that the shift of the Raman spectra observed in Fig. 4.6(b) and 4.6(c) for the decorated graphene layers are attributed to the introduction of the ZnO nanomesh. Fig. 4.6(b) shows the shift of G band for the decorated samples compared with the pristine one, where Fig. 4.6(c) shows the shift of 2D band for the corresponding samples. As shown in Fig. 4.6(b) and (c), a red-shift of 5 and 2 cm^{-1} were recorded from the G and 2D band respectively for

the *n*-type GFET. This implies the graphene is *n*-doped by coating ZnO nanomesh of 17 nm thick. On the contrary, a blue-shift of 4 and 9 cm^{-1} were recorded from the G and 2D respectively for the *p*-type GFET, which was covered with a ZnO nanomesh of 24 nm thick. This suggests that longer exposure of O_2 plasma could lead to *p*-type doping in the graphene.

Furthermore, former studies from other group has shown that the strain-induced shift of the G band would be ~2 times smaller than that of the 2D band, which is inconsistent with our results [63]. We therefore attribute the blue- and red-shifted G and 2D bands in Fig. 4.6 to a high level of hole and electron doping in the GFETs.

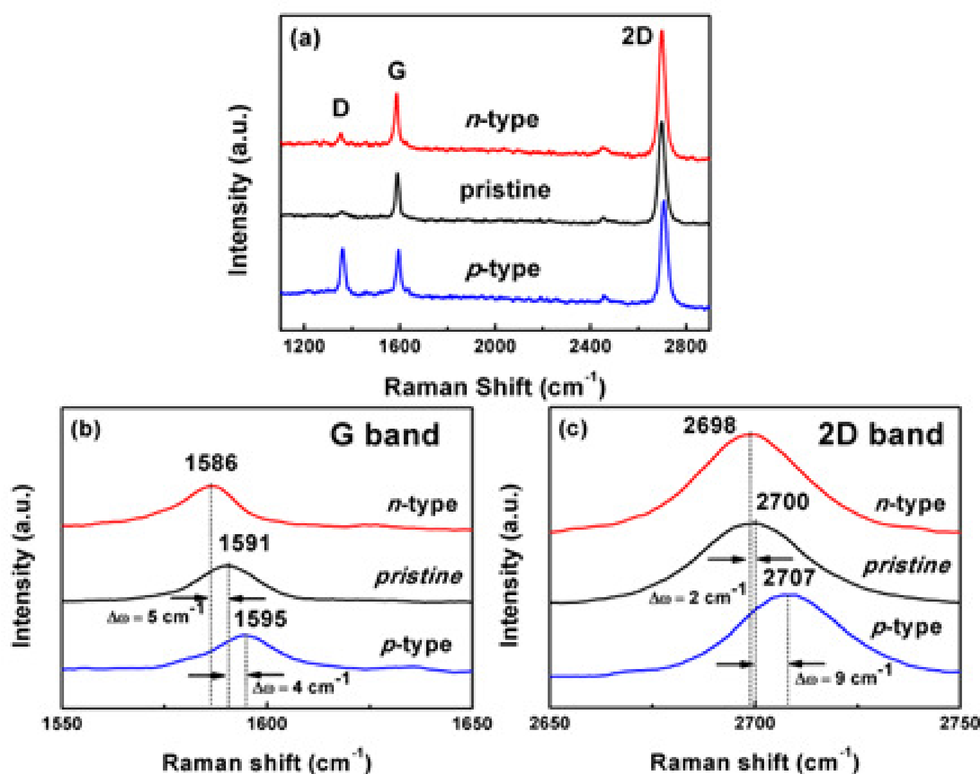

Fig. 4.6(a)Raman spectra of *n*-type, pristine and *p*-type GFETs. The corresponding magnified Raman (b)G and (c)2D bands.

4.3.5 Effect of Annealing Temperature and ZnO Thickness

The relationship between CNP of the GFETs and the annealing temperature are shown in Fig. 4.7(a). The GFETs were annealed at different temperatures from 100 ^{o}C to 400 ^{o}C for 15 min. For the pristine sample, the CNP decreases proportionally with the annealing temperature. When the annealing temperature was above 200 ^{o}C, the CNP of the pristine graphene became negative. This large perturbation to the electrical properties of the pristine GFET could be due to the induced strain by closer contact of the graphene with the silicon substrate or *n*-type doping under the

thermal annealing in N_2 environment [33, 64]. This perturbation is found to be compensated by the deposition of the ZnO nanomesh as shown in Fig. 4.7(a).The CNP remains almost constant even though the annealing temperature was above 200 ^{o}C for both ZnO nanomesh coated *n*-and *p*-type GFETs. Therefore, the ZnO nanomesh could enhance the stability of the GFETs. The effect of the induced strain is believed to be compensated by the ZnO nanomesh on top of the graphene surface.

A more detailed relationship between the thicknesses of ZnO nanomesh and CNP are represented in Fig. 4.7(b). Four different GFETs were fabricated, including pristine GFET and 11, 17 and 24 nm thick ZnO nanomesh coated GFETs, which correspond to 0, 1, 3 and 5 min deposition time of the ZnO. We note that a linear relationship was observed between the CNP and the thickness of the ZnO nanomesh. When the deposition thickness (time) for the ZnO was decreased, the CNP was shifted to a more negative value and vice versa. The CNP of the decorated GFET could vary from -45 to +15 V by tuning the thickness of the ZnO nanomesh.

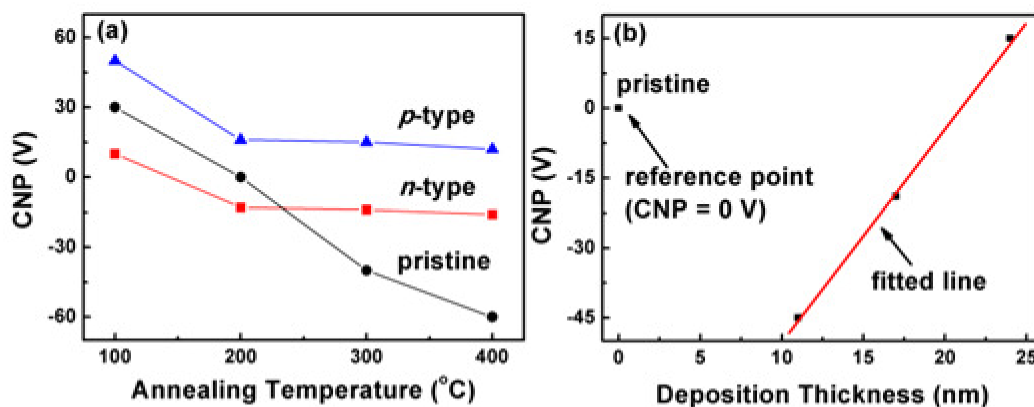

Fig. 4.7(a)CNP as a function of annealing temperature for the *n*-type, pristine and *p*-type GFETs. (b)CNP as a function of ZnO nanomesh thickness for the ZnO nanomesh coated GFETs.

4.4 Summary

In summary, *n*- and *p*-type GFETs can be controlled by tuning the thickness of the ZnO nanomesh coated on the graphene surface. The thermal stability of the ZnO nanomesh coated GFETs can be enhanced substantially up to 400 °C as compared to the pristine GFETs. This nanopatterning technique could open up new opportunities for reliable interfaces between graphene and substrate or even between graphene and adsorbates for controllable field effect properties.

Chapter 5 Biaxial Strain in MoS_2

5.1 Introduction

Strain engineering is a powerful and widely used strategy for boosting the performance of electronic, optoelectronic and spintronic devices [65-68]. By applying a strain through lattice mismatch between epitaxial films and substrates or through bending of films on elastic substrates, this strategy can be used to increase the carrier mobility in semiconductors [65] or to lift the emission efficiency of light-emitting devices [68]. Particularly, due to reduced dimensions, nanostructures become more flexible to be highly strained, which provides more space for strain engineering. A vast of strain effects on the electronic behaviors in quasi one-dimensional nanostructures such as carbon nanotube, GaAs nanowire and ZnO nanowire have been revealed [69, 70]. Technically speaking the emerging two-dimensional (2D) crystals such as graphene, hexagonal boron nitride and molybdenum disulfide (MoS_2) shall be more favored for strain engineering [71], as they only consist of one or few atoms in thickness. Whereas the strain-tunable phonon properties in graphene are intensively studied by Raman scattering, the theoretically predicted bandgap opening in graphene by strain has not been achieved in experiments [6, 71, 72]. On the other hand, 2D atomic layers of MoS_2, one of transition metal dichalcogenides, have attracted great interest because of its

distinctive electronic and optical properties; especially its bandgap has been predicted to be highly strain-tunable [15, 73]. Hence, developing effective routes to apply tunable strain in 2D atomic layers like MoS_2 is highly desirable for strain engineering.

We develop a novel electro-mechanical device to apply uniform and controllable biaxial compressive strain up to 0.2 % in tri-layer MoS_2 and perform photoluminescence (PL) and Raman detections simultaneously. The strain is applied by a piezoelectric substrate, while its transparency to PL detection is realized by using a graphene layer as transparent top electrode. The PL and Raman spectra measurements show that the electronic structure and phonon spectrum in tri-layer MoS_2 can be smoothly modulated by strain ranging from 0 to 0.2 %, which are further confirmed by first-principles investigations. Surprisingly, the direct bandgap of tri-layer MoS_2 blue shifts remarkably by ~300 meV per 1% strain, which is unprecedentedly large among all bulk or nanostructure semiconductors under strain. Moreover, the PL intensity can be increased by 200% accompanying with ~40 % reduction in the full-width-half-maximum (FWHM) of the emission spectrum for an applied strain of ~0.2 %. These results build up a

platform generally applicable for strain engineering in the emerging 2D crystals such as transition metal dichalcogenides.

5.2 Experiment

Characterization methods: High resolution x-ray diffractometer (Rigaku, SmartLab, 9 kW) equipped with a Ge (220) 2 bounce monochromator was used to obtain 2θ scanning patterns of the single-crystal PMN-PT substrate. The electrical measurements were performed in ambient conditions using a Keithley 2410 Source Meter to provide a dc voltage for the graphene/MoS_2/PMN-PT electro-mechanical device.

First-principles calculations: The first-principles calculations were performed by Xiaofei Liu upon collaboration. The first-principles calculations for the band structure of tri-layer MoS_2 was performed within the framework of density functional theory as implemented in the VASP code [74, 75]. The projector-augmented wave method [76, 77] for the core region and the Perdew-Burke-Ernzerh of functional [78] for the exchange-correlation potential

were employed in calculations. The kinetic energy cutoff of the plane-wave expansion is set to be 500 eV. The conjugate gradient method was used to fully relax the geometry until the force on each atom is less than 0.01 eV/Å. Convergence with respect to the mesh of *K*-points was carefully tested before the calculations. The calculations of Raman modes were performed with density functional perturbation theory.

5.3 Result and Discussion

5.3.1 Fabrication of electro-mechanical device

Fig. 5.1(a) depicts the configuration of our electro-mechanical device. The starting point for the fabrication of our electro-mechanical device was the chemical vapor deposition (CVD) of large-area tri-layer MoS_2 [23]. The layer number was clearly identified from the high-resolution transmission electron microscopy (TEM) image at the edge of the MoS_2 sample (Fig. 5.1(b)) and verified by atomic force microscopy (AFM) with a thickness of ~2.1 nm (Fig. 5.1(c)). Then, the MoS_2 sample was transferred onto a piezoelectric substrate ($[Pb(Mg_{1/3}Nb_{2/3})O_3]_{0.7}$-$[PbTiO_3]_{0.3}$, PMN-PT) and covered by a monolayer graphene as the top electrode. When a bias voltage was applied between the graphene top electrode and the gold bottom electrode, a biaxial compressive strain

could be applied to the substrate due to piezoelectricity [79] and then transferred to the tri-layer MoS_2. In our experiments, the PMN-PT was not polarized before the measurement, which guaranteed that the PMN-PT could only generate an in-plane compressive stress regardless of the bias voltage directions. Indeed we obtained nearly the same results when the polarity was reversed in our experiments. It is worth mentioning that the top graphene electrode was essential for the electro-mechanical device. Firstly, while graphene was conductive as an electrode, it was transparent without blocking the PL and Raman signal from the MoS_2. Secondly, the atomically thin graphene is relatively soft compared with other conductive films as an electrode. As a result, the strain from the substrate could be fully transferred to the MoS_2 sheet without being blocked by other thick electrodes. Another advantage of this device structure was that the resistance of the monolayer graphene (~kΩ) and the tri-layer MoS_2 (~MΩ) were low as compared with the insulating PMN-PT substrate (~GΩ) that the voltage drop from the intermediate MoS_2 or graphene sheets could be neglected.

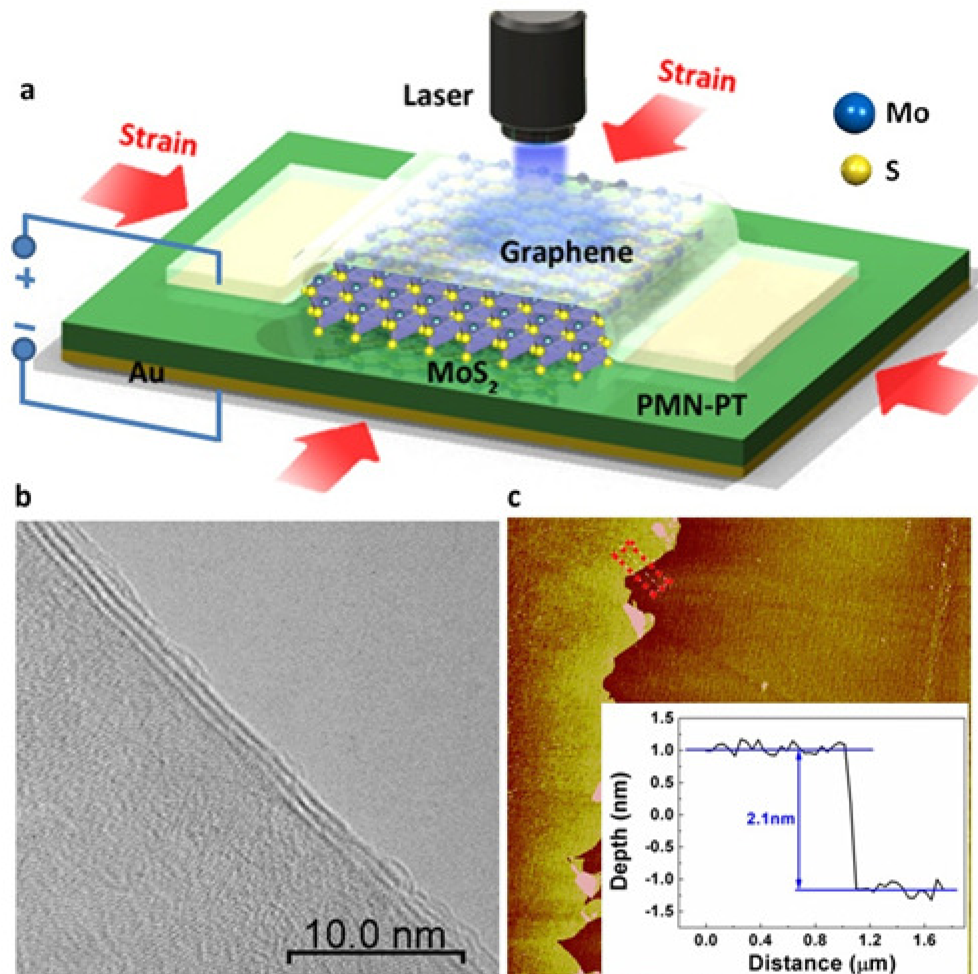

Fig. 5.1 Experimental setup and structural properties of tri-layer MoS_2. (a) Schematic diagram of Raman and PL measurements on MoS_2 which is sandwiched between a piezoelectric PMN-PT substrate and a graphene top electrode. (b)High-resolution TEM image at the edge of tri-layer MoS_2. (c)AFM image of the tri-layer MoS_2. The inset shows the depth profile of the tri-layer MoS_2 which indicates a thickness of 2.1 nm.

5.3.2 X-ray diffraction characterization

The polarization-induced strain in the lattices of piezoelectric substrate and tri-layer MoS_2 was probed by x-ray diffraction (XRD) measurement (Fig. 5.2(a) and (b)). As the vertical voltage increased, the XRD peak that corresponds to the

(002) plane (i.e. *c*-axis) of the PMN-PT substrate shifted to lower angles [80], which indicated that the out-of-plane lattice constant *c* and the in-plane lattice constant in the substrate were expanding and shrinking, respectively. The relation [81] between the polarization-induced out-of-plane strain $\varepsilon_{\perp}$ and in-plane strain $\varepsilon_{\parallel}$ in the PMN-PT substrate can be written as $\varepsilon_{\parallel} \approx -0.7\varepsilon_{\perp}$. When the biased voltage reached 500 V (i.e. 10 kV/cm), the in-plane compressive strain was estimated to be about 0.2%. In the case of MoS_2, the characteristic XRD peak of the MoS_2 (i.e. (105)) also shifted to lower angles compared with that in the strain-free status, which implied that the compressive strain was transferred from the PMN-PT to the MoS_2. However, it was not possible to estimate the strain magnitude induced in the MoS_2 sheet directly by its XRD characterization, since we could only observe one prominent (105) peak. Although it was still unclear whether the interfacial mechanic interaction was strong enough to completely transfer the strain produced in the PMN-PT to the target MoS_2, for simplicity, the strain values in the tri-layer MoS_2 was assumed to be equal to the strain measured from the PMN-PT.

A large lattice strain could be induced by ferroelectric polarization of the PMN-PT substrate due to the rotation of polarization direction toward the direction of electric field [66]. Fig. 5.2(a) shows the XRD spectra of the PMN-PT substrate under various biasing voltages. The peak position corresponds to the (002) plane

(i.e. *c*-axis) of the PMN-PT [82]. The XRD peak position was shifted to smaller angles as the bias voltage increased as shown in Fig. 5.2(a), which suggested that the lattice constant *c* of the substrate was expanding under a tensile stress. Fig. 5.2(b) presents the in-plane strain and XRD shifted as a function of bias voltage. The results indicated that the electric-field-induced ferroelectric polarization gave rise to a large decrease in the 2θ angle of the PMN-PT substrate, which corresponded to an increase of strain in the in-plane direction. When the biased voltage reached 500 V, the compressive strain is about 0.2 %.

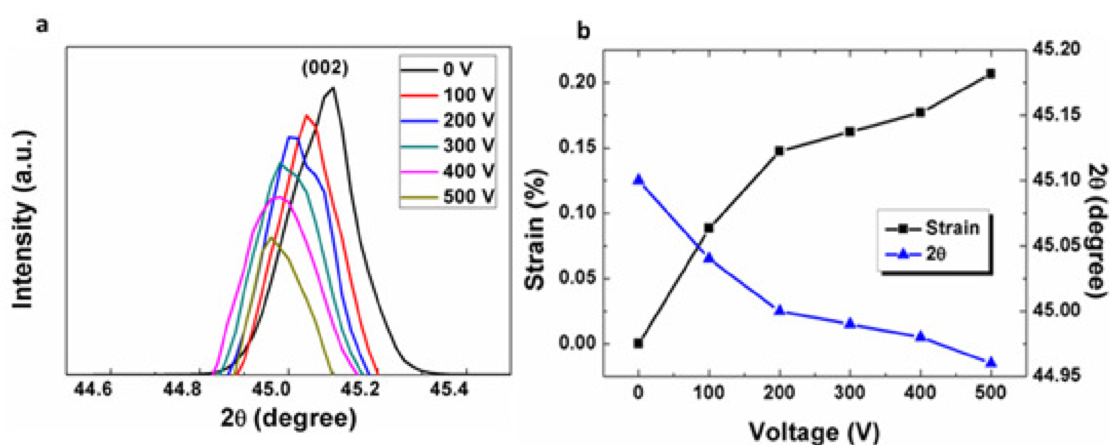

Fig. 5.2(a) The XRD shifts of the PMN-PT substrate at bias voltages from 0 to 500 V. (b)The XRD shifts and the corresponding induced compressive strain as a function of bias voltage.

Fig. 5.3(a) shows the XRD shifts of the tri-layer MoS_2 at different applied strains. It is found that the strain from the PMN-PT was transferred to the MoS_2

layer because a blue-shift in the XRD peak position could be observed. It is found the (105) plane of the MoS_2 is shifted to lower angle as the strain increased as shown in Fig. 5.3(b). The XRD (105) peak was obtained by glancing incident angle (GIA) mode in XRD. The full XRD spectrum of the MoS_2 sheet is shown in the inset of Fig. 5.3(b).

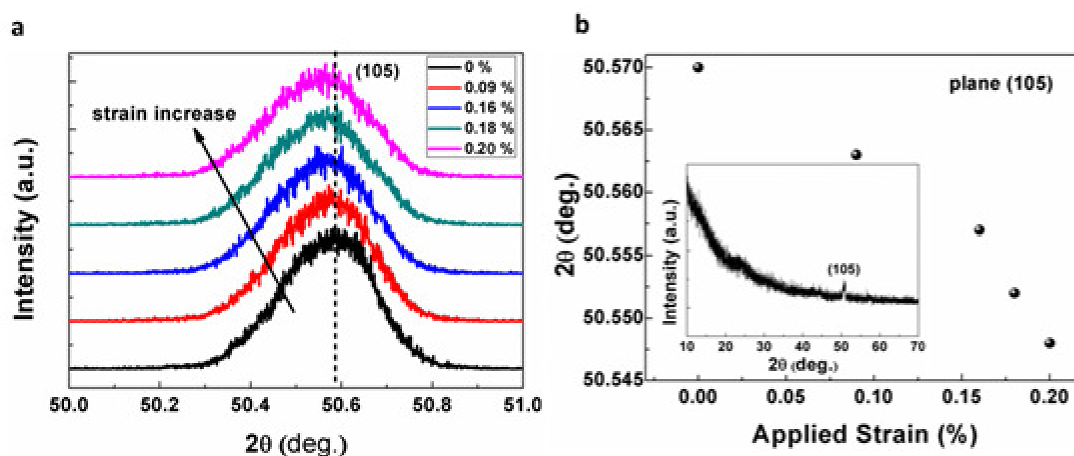

Fig. 5.3(a)The XRD peak shifts of the tri-layer MoS_2 at different applied strains. (b)The corresponding XRD peak shift as a function of applied strain. The inset shows the full GIA XRD spectrum of the tri-layer MoS_2.

5.3.3 Elastic properties

Fig. 5.4(a) shows the strain and PL peak position as a function of bias voltage. Both the strain and PL peak position increase monotonically with the bias voltage. Therefore, the PL shift of the MoS_2 is attributed to the increase in strain induced by the PMN-PT substrate. Fig. 5.4(b) shows the elastic properties of the MoS_2 device.

The PL peak position is increased linearly with the increase in strain (step 1). The PL peak position follows the similar path as step 1 as the strain decreases from the maximum point to zero. The strain applied to the MoS_2 is elastic as the PL peak position can return to its original position while the strain is removed. It should be noted that the PL peak position follow the path very well even after several months of repeated measurements.

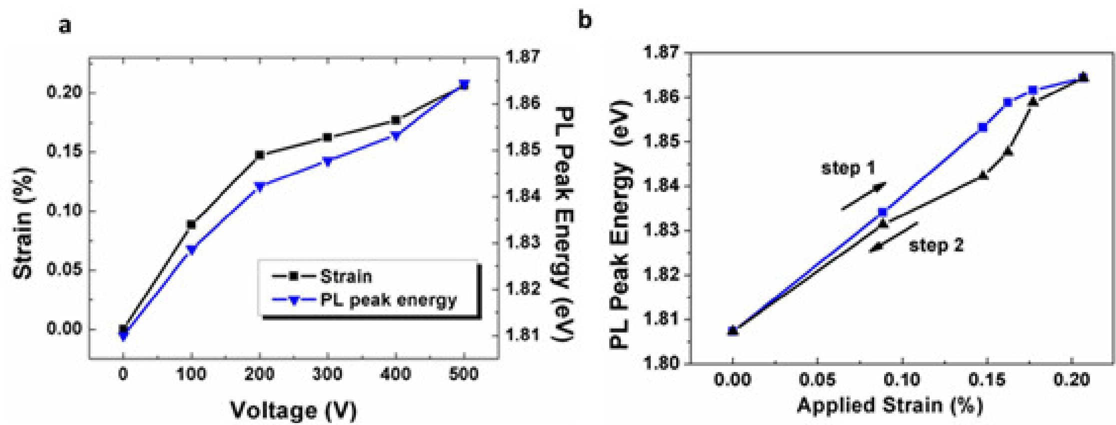

Fig. 5.4(a)The PL peak position and strain as a function of bias voltage. (b)The dependence of the PL peak position as a function of strain (step 1: increasing strain and step 2: decreasing strain).

5.3.4 Raman characterization

Fig. 5.5(a) presents the typical Raman spectra of the MoS_2 at different strains. Among the four Raman-active modes of bulk MoS_2, the E_{2g}^1 and A_{1g} modes for

the strain-free tri-layer MoS_2 were observed at 382.4 and 405.4 cm^{-1}, respectively. The difference between the two modes is 23 cm^{-1}, in good agreement with that found in mechanically exfoliated tri-layer MoS_2 [83, 84]. Both the two modes shifted to higher frequencies Fig. 5.5(b) as compressive strain being applied. For the applied strain of 0.2 %, the E_{2g}^1 and A_{1g} modes shifted by ~3 and ~2 cm^{-1} respectively, with a shift ratio of E_{2g}^1 to A_{1g} of ~1.5. Since the blue-shift of the two modes was previously observed in MoS_2 nanotubes and MoS_2 bulk crystal at high pressure [85, 86], the observed change in the Raman modes were surely attributed to the presence of compressive strain. To further confirm this, we calculated the responses of Raman modes at strains ranging from 0.0 to 0.6 % (Fig. 5.5(c)). The calculated Raman modes exhibit a similar trend of blue-shifts as observed in the experiment, but with a higher Raman shift ratio of E_{2g}^1 to A_{1g} of ~2.5. In general, the calculated Raman frequencies were underestimated (Fig. 5.5(c)), but the deviation from experiments was only a few cm^{-1}. Likely, the calculated blue-shift rates in tri-layer MoS_2 were also underestimated that the blue-shifts for E_{2g}^1 and A_{1g} were ~0.93 and ~0.35 cm^{-1} at the 0.2% strain, respectively.

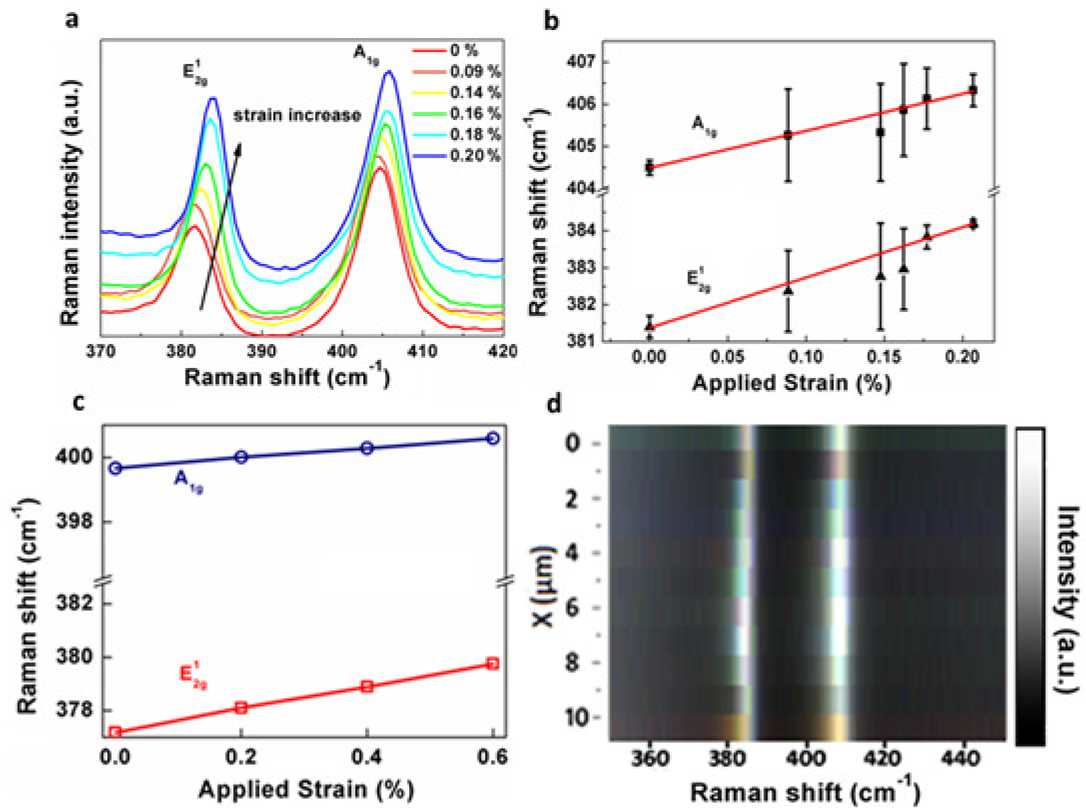

Fig. 5.5 Raman spectra of tri-layer MoS_2 under different strains. (a)The Raman spectra of the tri-layer MoS_2 under various applied strains. (b)The Raman shift of E^1_{2g} and A_{1g} modes as a function of strain. (c)The Raman shift of E^1_{2g} and A_{1g} modes as a function of strain calculated by density functional perturbation theory. (d)1D spatial mapping of the Raman shift of E^1_{2g} and A_{1g} modes under the applied strain of 0.2%.

The evolution of the electronic structure in the tri-layer MoS_2 under biaxial compressive strain was investigated by PL spectroscopy. At the strain-free state, a broad PL peak centered at 1.8 eV was observed, which can be assigned to the direct band emission (E_{dir}) of MoS_2 [23, 87, 88]. As the strain increased, the PL emission peak shifted to higher energy remarkably and near linearly and a total shift of ~60 meV (~20 nm change in wavelength) was recorded with an applied strain of 0.2%

(Fig. 5.6(a)). Upon slow release of strain, the PL peak could return to the original position approximately following the original path even after several cycles of repeated measurements (Fig. 5.4). Therefore, the strain transferred into the tri-layer MoS_2 was in its elastic region and fully controlled by the electro-mechanical device. In addition to the effective control of the E_{dir}, an increase of the PL emission intensity up to ~200% and a reduction of FWHM by 40% were observed (see the inset in Fig. 5.6(b)). The enhancement of the emission efficiency is attributed to the change of the electronic structure under applied strain. It is worth noting that the tunability of E_{dir} by strain was ~300 meV per 1% strain, which was the highest value ever reported for strained semiconductors to the best of our knowledge. For instance, bandgap tunability in semiconductors, such as GaAs/AlGaAs quantum dots (~70 meV/%) [81], GaAs nanowires [69] (~85 meV/%), and ZnO nanowires (~35meV/%) [89] were reported.

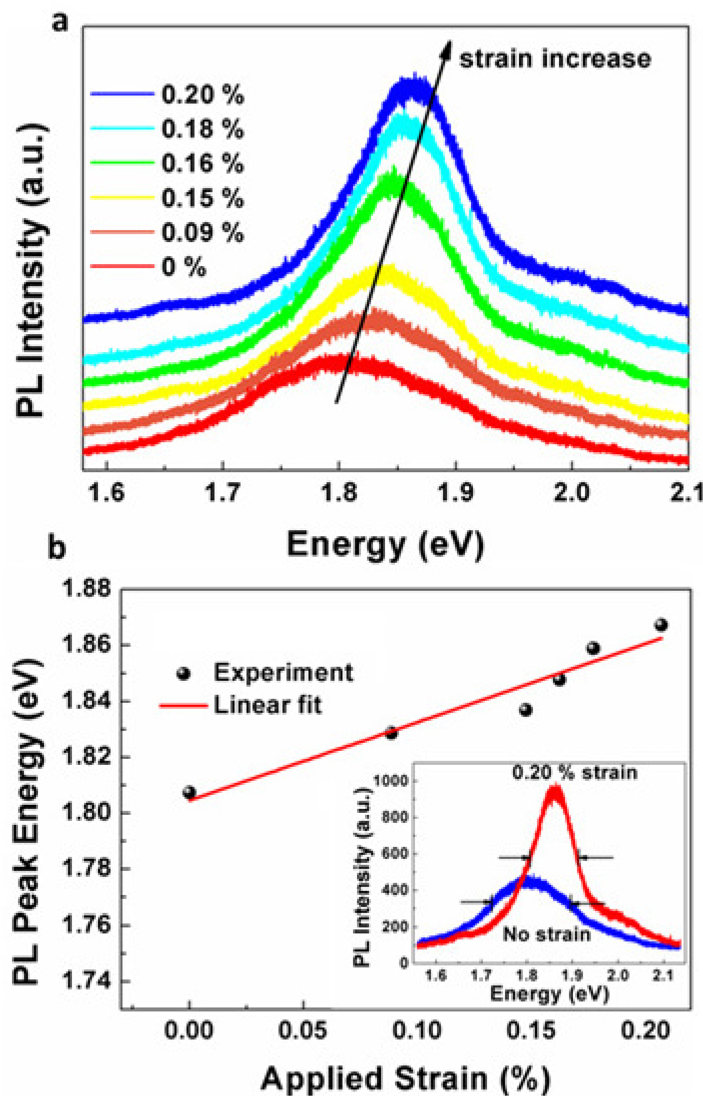

Fig. 5.6 Photoluminescence property of tri-layer MoS_2 under strain. (a)The PL spectra of the MoS_2 under various strains. (b)The PL peak energy as a function of compressive strain. The inset shows the PL spectra of the sample under 0.0 % and 0. 2 % strain.

5.3.5 First-principles calculations

To understand the strain dependence of the PL spectra, we carried out first-principles calculations for band structures of tri-layer MoS_2 under different

biaxial strains. Consistent with pervious researches, the tri-layer MoS_2 is shown to be an indirect semiconductor, with the indirect bandgap (E_{id}) determined by the valence band maximum (VBM) at the Γ point and the conduction band minimum (CBM) at the K point. Although the first-principles calculations usually under estimated the bandgaps, the trend of change in E_{dir} under applied strain agrees with the PL emission peak shifts. As shown in Fig. 5.7(a), with increased compressive strain, both VBM and CBM shift to higher energies, but the CBM is more sensitive to strain, resulting in an enlargement of E_{dir}. At applied strain of 0.2 %, the calculated blue-shift of E_{dir} and E_{id} are 18 and 36 meV, respectively, severely underestimated as compared with the experimentally observed shift for E_{dir} (~60 meV). The computational results also imply that the tri-layer MoS_2 remains to be an indirect semiconductor under compressive strain up to 0.6%, but the energy difference between E_{id} and E_{dir} is reducing as the strain increases (Fig. 5.7(b)).

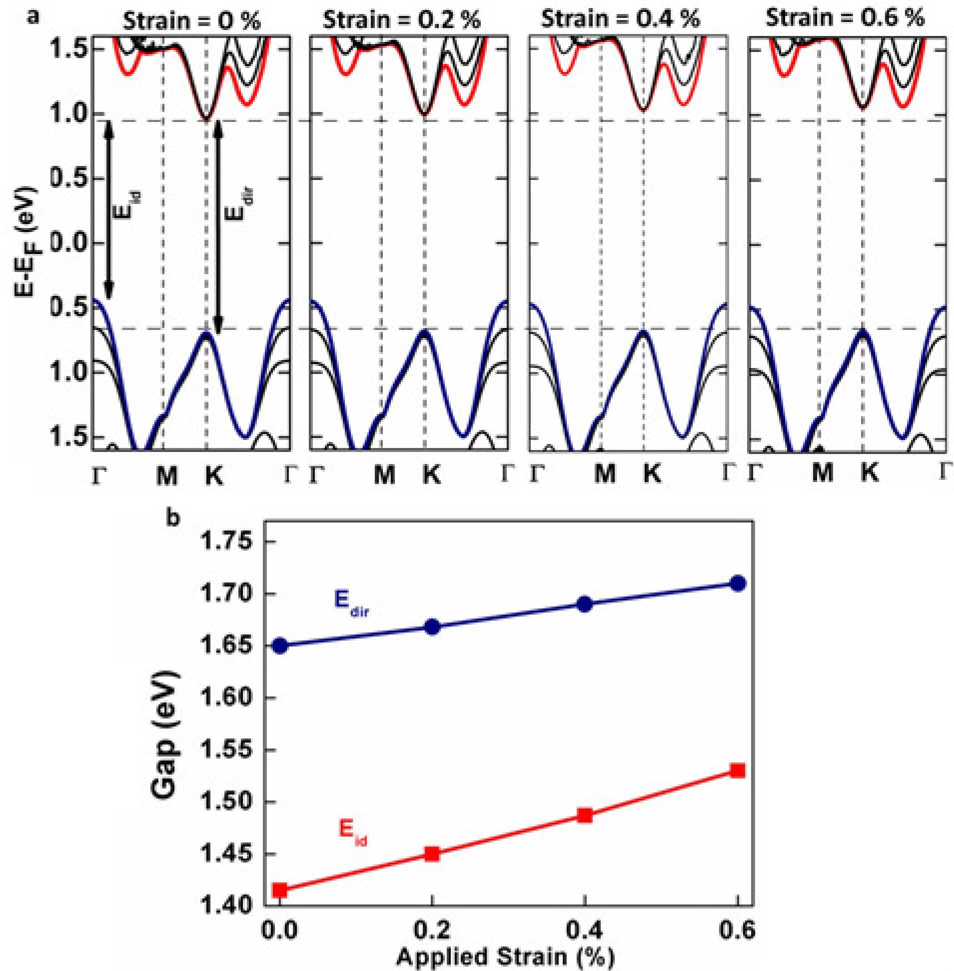

Fig. 5.7 First-principles band structures of tri-layer MoS_2. (a)Band structures of *Ab-bA* stacking tri-layer MoS_2 under 0.0, 0.2, 0.4 and 0.6% biaxial compressive strain. (b)Energy gaps as a function of biaxial compressive strain.

Moreover, the strain-tunability of E_{id} in tri-layer MoS_2 is twice the value of E_{dir} according to the first-principles results (Table. 5.1). It is noteworthy that there were two possible stacking sequences for tri-layer MoS_2, namely *Ab-bA* and *Ab-Ab* as shown in Fig. 5.8(a) and the above band structures were results about *Ab-bA* stacking MoS_2. While the bandgaps of *Ab-Ab* stacking MoS_2 were slightly larger, the trend of bandgaps under strain was the same.

Table SII. Biaxial compressive strain correlated bandgap energy of tri-layer MoS_2					
Strain (%)	**E_{dir}(eV)** (*Ab-bA*) (simulation)	**E_{dir}(eV)** (*Ab-Ab*) (simulation)	**E_{id}(eV)** (*Ab-bA*) (simulation)	**E_{id}(eV)** (*Ab-Ab*) (simulation)	**E_{dir}(eV)** (experiment)
0.0	1.650	1.655	1.415	1.455	1.807
0.2	1.668	1.672	1.451	1.510	1.867
0.4	1.690	1.702	1.487	1.565	N/A
0.6	1.710	1.725	1.532	1.610	N/A

Table. 5.1 Biaxial compressive strain correlated bandgap energy of tri-layer MoS_2.

Fig. 5.8(a) shows the schematic illustrations of the two possible stacking sequences for tri-layer MoS_2, namely *Ab-Ab* and *Ab-bA* stacking. Fig. 5.8(b) shows the calculated Raman frequencies of the two Raman modes (E^1_{2g} and A_{1g}) as a function of strain for the two stacking sequences of MoS_2. The two Raman modes increased linearly with the applied strain regardless of the stacking sequence. The Raman frequencies of the *Ab-Ab* stacked MoS_2 were slightly higher than that of the *Ab-bA* stacking. As for the band gap energy, the E_{dir} and E_{id} increased linearly with the applied strain for the two stacking orders as shown in Fig. 5.8(c). In general,

the *Ab-Ab* stacked MoS_2 also exhibited higher bandgap (E_{dir} and E_{id}) than that of the *Ab-bA* stacking.

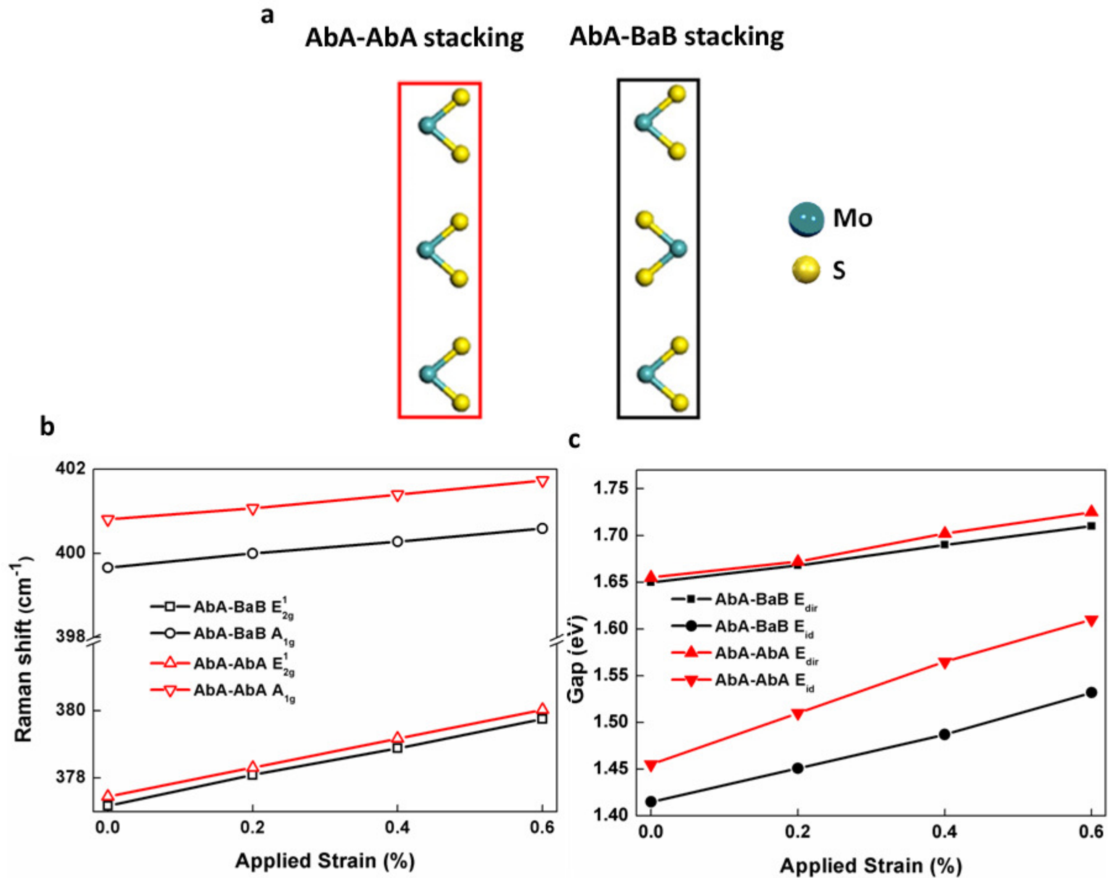

Fig. 5.8 First-principles band structure calculations of tri-layer MoS_2. (a)Schematic illustrations of the *Ab-Ab* and *Ab-bA* stacking tri-layer MoS_2. (b)Raman shifts as a function of biaxial compressive strain. (c)Energy gaps as a function of biaxial compressive strain.

It is of significance that the observed strain-induced shifts of band energy in our experiment was from a large-area and homogenous tri-layer MoS_2 rather than from

a non-uniform MoS_2 with a mixture of number of layers which usually happens in mechanically exfoliated MoS_2 sheets. To verify that our sample contained only uniform tri-layer MoS_2, we measured the PL and Raman mappings of the sample. The typical mapping results showed that over a 10×10 μm^2 scanning area, the PL and Raman peak intensities were uniform and the positions of the two Raman modes were constant in the entire scanning area on their respective frequencies (Fig. 5.9). The uniformity of the tri-layer MoS_2 is revealed by the Raman and PL mapping measurements. Fig. 5.9(a) (top) shows the optical image of the MoS_2. Inside the square is the PL mapping (10×10 μm^2). The PL spectrum of the MoS_2 is shown in the bottom of Fig. 5.9(a). Fig. 5.9(b) shows the Raman peak intensity mapping of the E^1_{2g} and A_{1g} Raman modes, the intensities were uniform with little variation. The 2D and 3D Raman shift mappings were shown in Fig. 5.9(c). The two vibration modes (E^1_{2g} and A_{1g}) are located at almost the same position throughout the scanning area as reveal from two bands as shown in top graph of Fig. 5.9(c). More importantly, we found that the applied strain were also uniform and homogenous, which was clearly shown by the 2D spatial Raman mapping of the MoS_2 under strain of 0.2% in Fig. 5.9(d). Similar strain induced PL shift was observed in MoS_2 nanosheets recently [32]. Finally, we could rule out the possibility that the band structures of the tri-layer MoS_2 could be influenced by the

applied vertical electric field, considering that the bandgap of bi-layer MoS_2 could only be reduced by a field four orders of magnitude larger than that used in our device [90]. Furthermore, when we replaced the piezoelectric PMN-PT substrate with sapphire and applied an electric voltage, no PL or Raman shifts in the tri-layer MoS_2 were observed.

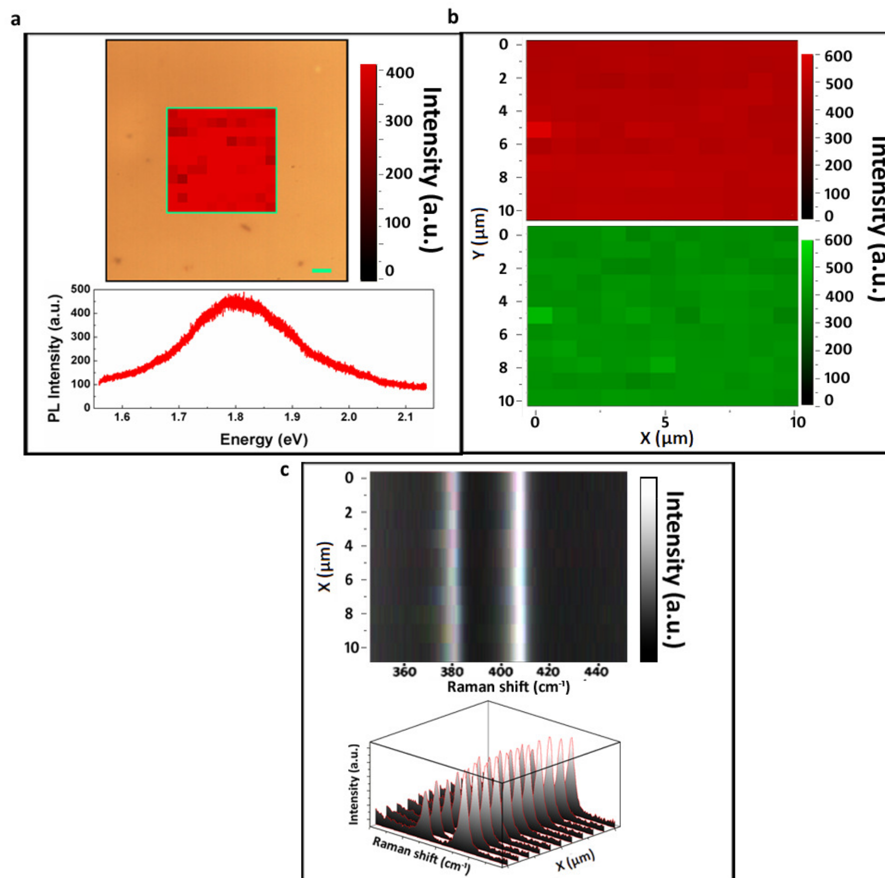

Fig. 5.9(a)Optical micrograph of the tri-layer MoS_2 placed on PMN-PT substrate showing the PL intensity mapping area (10×10 μm^2). The bottom graph is the PL spectrum of the sample. (b)Raman intensity mapping of the E^1_{2g} (bottom) and A_{1g} (top) modes in the scanning area. (c)2D (top) and 3D (bottom) spatial mappings of the Raman shift of E^1_{2g} and A_{1g} modes.

5.4 Summary

In summary, the experimental approach demonstrated here was based on the use of piezoelectric actuators made of single crystal PMN-PT, which were capable of providing controllable compressive strain up to 0.2 %. In addition to the ability to tune the emission energy over a large range of 60 meV, the applied strain could enhance the PL intensity. The developed methodology could be employed on a wide range of 2D crystals. Besides the band structure, it would also allow us to investigate in detail the effects produced by tunable strains on other important physical properties of 2D crystals such as ferromagnetism [91, 92]. We envision its use in high-performance electronic, piezoelectric, photovoltaic, optoelectronic and spintronic devices.

Chapter 6 Local Strain Profile in 2D Materials

6.1 Introduction

Strain engineering in two-dimensional (2D) materials can significantly enhance their electronic, photonic and spintronic performances [15]. By controlling their band structures with the use of strain, it constitutes an important strategy to enhance the performance of electronic devices [93]. By controlling local strain, confinement potentials for excitons can be engineered, with possibilities for trapping excitons for quantum optics and for efficient collection of solar energy [66, 94]. Recent discovery of semiconducting monolayer materials with a large direct band gap has open up a realm of electronic possibilities that have not been previously exploited in traditional thin film structured crystals, which allows fabrication of conventional electronic devices [19, 95-97]. For example, simulations have predicted that the mobility of monolayer MoS_2 can be tuned under strain [66, 73]. This could further increase the transistors performance of monolayer MoS_2; the large rupture strength of monolayer MoS_2 allows one to induce large local strains by bending or folding the material like a piece of paper, which allows it to bend to a large degree without breaking even it is free standing [97, 98]. This allows tunable PL at visible wavelengths, which will be useful for the fabrication of conventional LEDs and photodetectors [20]. Nowadays, the shifts of optical wavelengths have been well

established in 2D materials phonon modes, allowing micro-Raman spectroscopy to detect the strains applied. While strain perturbs the band structure of 2D materials such as MoS_2 that can sustain strains greater than 11 %, allowing exceptional control of material properties by strain engineering [99]. As described in Chapter 5, externally efforts are required to apply strain onto MoS_2 via piezoelectric substrate. Although the method can enable us to study the strained behavior of any 2D materials, a specific substrate is required which limits the applications of 2D materials under strain.

We have developed an alternative approach that could apply continuous strain to any 2D materials on arbitrary substrates, using CVD grown monolayer MoS_2 as an example. We intentionally transferred monolayer MoS_2 onto trenches with different sizes, 5×5, 10×10 and 20×20 μm^2 so as to produce localized strains by allowing the MoS_2 to be free standing. Prior to transferring the MoS_2 nanosheet onto a substrate, trenches on arbitrary substrates with different sizes were etched using FIB system. Depending of the depth of the trenches, compressive and tensile strains could be induced into the MoS_2. The applied strain was quantified by a combination of Raman and PL spectroscopies. The effect of the non-uniform strain on the bandgap was also spatially resolved. Experimental results showed that the strain applied on

the MoS_2 can be tuned in a large scale once that the MoS_2 became free standing. The Raman shift in MoS_2 transferred on trenches with various sizes is ranging from 1 to 12 cm^{-1}, whereas the PL shift varied from 3 to 14 nm. This is due to the different amount of strains induced into the free standing MoS_2. The exceptional high strain tunability of electronic band structure in 2D materials provide a wide range of applications in functional nanodevices and the developed methodology should be generally applicable for other 2D semiconductors.

6.2 Experiment

Fabrication of free standing MoS_2: Fig. 6.1 shows the fabrication process of the strained MoS_2. (1)Monolayer MoS_2 nanosheets grown on sapphire substrates are prepared by CVD process as described in Chapter 3.1.3 [23]. (2)CVD grown graphene (as described in Chapter 3) is coated with a layer of PMMA (Micro Chem. 950L A4) by spin-coating (Step 1: 500 rpm for 10 s; step 2: 3000 rpm for 60 s), followed by baking at 100 ^{o}C for 10 min. After that, the copper foil is etched by iron chloride ($FeCl_3$) and the PMMA-capped graphene is then allowed to float on DI water. The MoS_2/sapphire substrate is brought into contact with the graphene film and it is "pulled" from the DI water solution. The graphene is allowed to dry naturally on top of the MoS_2 and subjected to further annealing at

100 °C for 15 min. (3)The graphene/MoS_2/sapphire is then put into a NaOH (2 M) solution at 100 °C for 30 min. The PMMA/graphene-capped MoS_2 film is transferred to DI water to dilute and remove the etchant and residues to detach the film from the sapphire substrate (1×1 mm^2 and 0.5 mm thick substrate). The film is allowed to flow on the etchant and then rinsed by DI water solution for a few times. (4)Meanwhile, a silicon substrate or PMN-PT substrate is treated with O_2 plasma for 5 min which is then used to lift the PMMA/graphene-capped MoS_2 film, followed by drying on a hot-plate (100 °C for 10 min). The PMMA is removed by acetone, isopropyl alcohol, and then DI water carefully to avoid breaking the free standing MoS_2. (5)Silicon substrates with 300 nm silicon dioxide on top or PMN-PT substrates are milled by FIB. A beam current of 1000 pA with a dose of 2 nC/μm^2 is used. The trenches with sizes of 5×5, 10×10 and 20×20 μm^2 are produced. (6)The PMMA/graphene-capped MoS_2 film is brought into contact with the patterned substrate and it is "pulled" from the DI water solution. It is allowed to dry naturally and then baked for 15 min at 100 °C. The graphene here is acted as a protective layer to avoid breaking of the free standing MoS_2 while removing the PMMA by immersing the sample into acetone carefully.

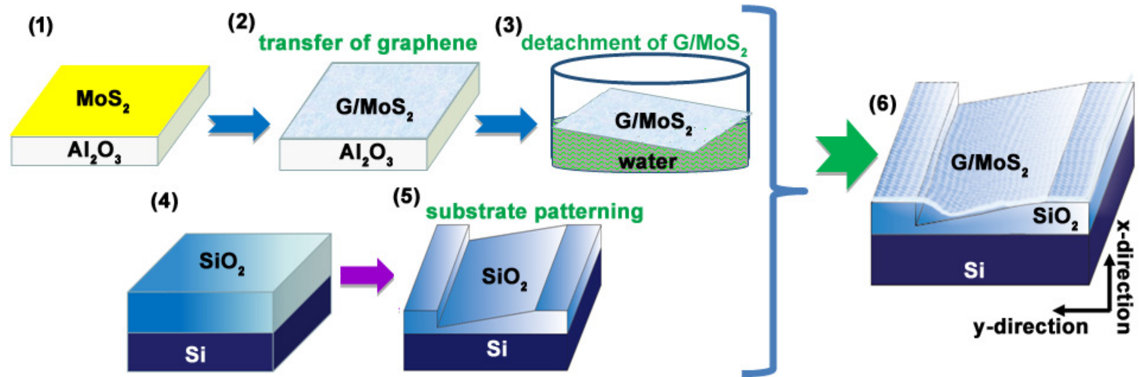

Fig. 6.1 Schematic diagram showing the fabrication process of the strained MoS_2 layer on SiO_2/Si substrate.

6.3 Results and Discussions

6.3.1 Strain engineered MoS_2

Fig. 6.2 depicts the configuration of the monolayer MoS_2 on the patterned substrate. The starting point is the fabrication of inclined trenches on SiO_2/Si substrate. The MoS_2 layer covered by a monolayer of graphene is transferred onto a SiO_2/Si substrate. The graphene layer is as a protective layer because of its strong mechanical strength and good thermal conductivity. A localized continuous uniaxial strain from compressive to tensile strain can be induced in the MoS_2. In our experiments, the uniaxial strain could also be induced to the MoS_2 coated onto a PMN-PT substrate with trenches. To simplify the process, an inclined trench with gradual change of depth was milled in order to create free-standing MoS_2 with inhomogeneous local strain. It is noted that if a trench with a fixed depth is used as the supporting substrate, the maximum size of the free standing MoS_2 can be

fabricated is around 5×5 μm^2. The free standing MoS_2 layers can be as large as 20×20 μm^2 if the inclined trenches are used. It is found that for the region with shallower depth (contact region) in the inclined trench, the MoS_2 will be in contact with the substrate and a compressive strain is induced. In contrast, tensile strain is induced for the deeper depth (free standing region) in the inclined trench. The intrinsically strain induced in the MoS_2 was probed by Raman spectroscopy. When the strain was compressive, Raman peaks would shift to higher frequencies such that a blue shift was recorded. On the contrary, Raman peaks would shift to lower frequencies such that a red shift was recorded when the strain was tensile. These shifts would go further away as the strain was getting larger. It is noted that a layer of transparent graphene was also transferred on top of the MoS_2 as a protective layer to increase the strength of the free standing MoS_2, making it possible to suspend on the 20×20 μm^2 trench without breaking. We found that without the use the graphene layer, the free standing MoS_2 would be broken if it was transferred to a 20×20 μm^2 inclined trench. Moreover, the graphene layer is essential for the mapping characterization to release the heat created by the laser as graphene is a good thermal conductor [100].

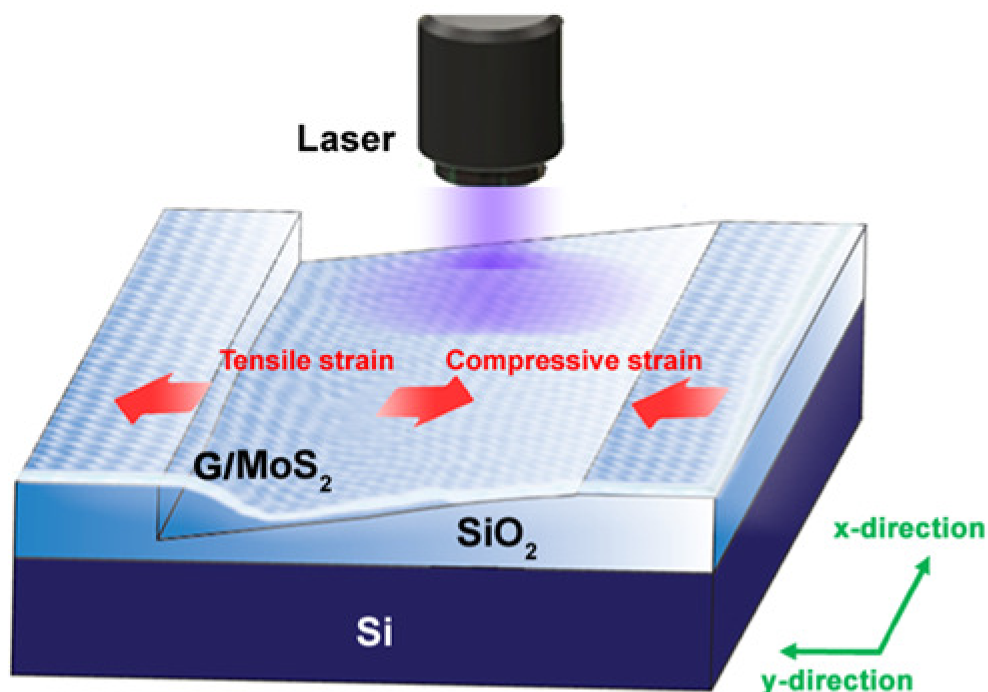

Fig. 6.2 Schematic diagram showing our experimental configuration of the strained MoS_2 layer on top of Si/SiO_2 substrate.

6.3.2 Raman characterization

Fig. 6.3(a) shows the fabricated inclined trenches with dimensions 5×5, 10×10 and 20×20 μm^2. It is noted that the maximum depth of each trench is kept constant as 0.8 μm. Hence, the smaller is the size of the trench, the steeper the slope is. The contrast of the depth variation along the y-direction could be observed clearly in the SEM image as shown in Fig. 6.3(b). After the transfer of the MoS_2 onto the patterned substrate (trench size of 20×20 μm^2), a "curtain" like thin film could be observed in an optical microscope as shown in Fig. 6.3(c), as indicated by a red dotted rectangle.

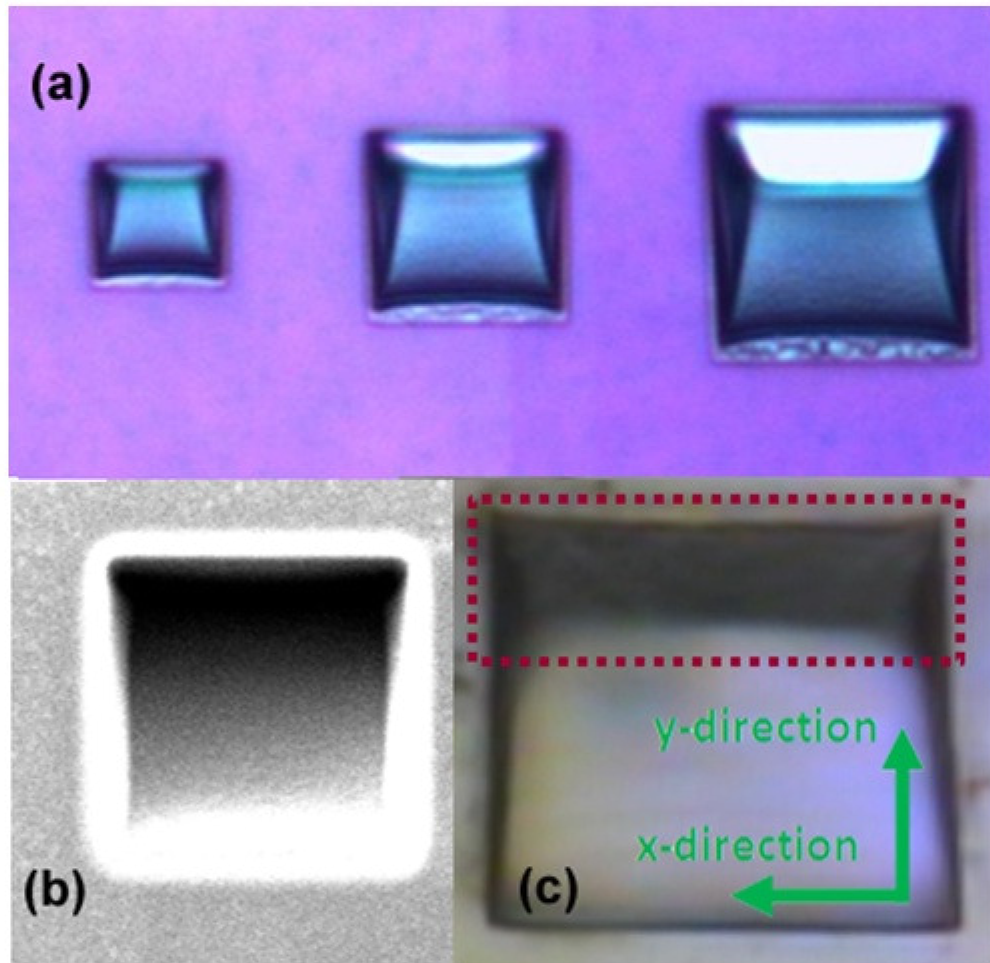

Fig. 6.3(a)Optical image of the inclined trenches with different sizes: 5×5, 10×10 and 20×20 μm^2. (b)SEM image of the 20×20 μm^2 inclined trench. (c)Optical image of a MoS_2 transferred onto a 20×20 μm^2 inclined trench. The free standing MoS_2 layer is visible in optical microscope, which looks like a "curtain" as indicate by the red dotted rectangle.

Fig. 6.4(a) and (b) present the typical spatial maps of the Raman A_{1g} and E_{2g}^1 modes of the MoS_2 on a 20×20 μm^2 inclined trench on top of a SiO_2/Si substrate. The Raman maps show that the E_{2g}^1 mode is more sensitive to the strain induced by the patterned substrate as indicated by its darker contrast in the spatial map. The maps also demonstrate that the frequencies of the two modes exhibit a large variation of Raman shift as a function of y-direction along the sample.

Inhomogeneous uniaxial strain on the MoS_2 is generated in this way. This permits the shift of the Raman frequencies to be used as an indicator of induced strain. The Raman shift along the y-direction could be attributed to the variation in depth of the trenches. It is found that the strain acting on the MoS_2 is compressive while it is in contact with the substrate at the shallow region as indicated by the blue dotted square as shown in Fig. 6.4(a) and (b). As the depth of the trench increases, the strain is crossed over from compressive to tensile while the MoS_2 is free standing as indicated by the red dotted square as shown in Fig. 6.4(a) and (b).

To investigate the crossover of compressive to tensile strain, the Raman spectra of the MoS_2 on the patterned PMN-PT substrates were measured. Fig. 6.4(c) shows the Raman spectra at the inclined, free standing and substrate regions. At the substrate region, a strong Raman background intensity from the PMN-PT was detected in addition to the two Raman vibration modes of the MoS_2. The positions of the two Raman peaks were consistent with the two vibration modes of MoS_2 without strain. This indicated that the MoS_2 was still in contact with the substrate at this region. At the free standing region, there was no Raman signal from the PMN-PT substrate. The two Raman peaks from the MoS_2 were detected. These two modes were significantly red shifted to a lower frequency as compared to the

Raman peaks obtained from the substrate region, which indicated that a large amount of tensile strain was induced to the MoS_2. At the inclined contact region, the MoS_2 was still in contact with the substrate therefore the Raman signal from the PMN-PT was still detected although the intensity is weaker. In contrast to the result obtained before, a slight blue shift was observed due to the inclined geometry of the trench. As a result, the absence of the Raman signal from the substrate could be an indicator for the free standing nature of the MoS_2.

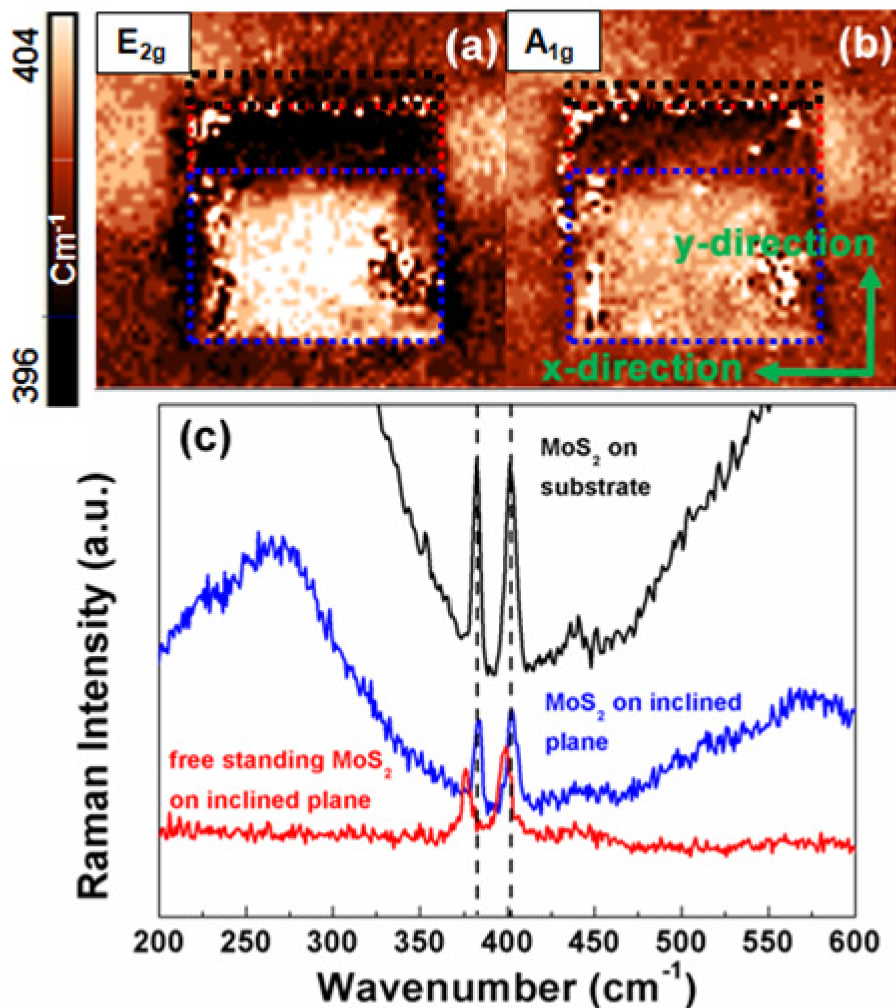

Fig. 6.4(a) and (b)Raman shift mapping profile of the E_{2g}^{1} and A_{1g} peaks of a strained MoS_2 on a 20×20 μm^2 inclined trench. The dark contrast in Raman shift mapping represents a shift to lower frequency (red shift, which is tensile strain). In the inclined region, the bright contrast represents a shift to higher frequency (blue shift, which is compressive strain). (c)Raman spectra of the corresponding sample in different regions of the trench.

Fig. 6.5 shows the E_{2g}^{1} and A_{1g} vibration modes of the MoS_2 as a function of the distance across the trench. The Raman behavior as a function of y-direction has several intriguing characteristics. Most strikingly, the induced strain in the MoS_2 can be crossed over from compressive to tensile once it reaches the free standing region as shown in Fig. 6.5(a). In other words, both of the E_{2g}^{1} and A_{1g} modes originally observed at 380.3 and 400.8 cm^{-1} respectively are shifted to higher frequencies (383.9 and 403.0 cm^{-1}) at compressive region. Meanwhile, the E_{2g}^{1} and A_{1g} modes are shifted to lower frequencies (372.7 and 396.7 cm^{-1}) at free standing region. Fig. 6.5(b) presents the typical Raman spectra of the corresponding MoS_2 at different regions of the inclined trench. The regions of the sample can be differentiated by observing the Raman intensity attributed to the PMN-PT substrate. These linear mapping results corresponded well with the spatial mapping results obtained above (Fig. 6.4). The inclined trench with various sizes could be used to create different strain profiles on the MoS_2 as shown in Fig. 6.5(c). With increasing trench size, the Raman shift (tensile region) increases rapidly as the trench size reached 20×20 μm^2. It should be due to the increase of free standing

region for larger trench size, which could give rise to a larger tensile strain. Fig. 6.5(d) shows the estimated uniaxial strain on the MoS_2 using the Raman shift. The strain is estimated using the linear relationship of the Raman shift against the uniaxial in-plane strain on monolayer MoS_2 established by Yang *et al.* [101] . The maximum tensile and compressive strain induced on the sample can be as large as ~4.85 and ~-1.6 % respectively.

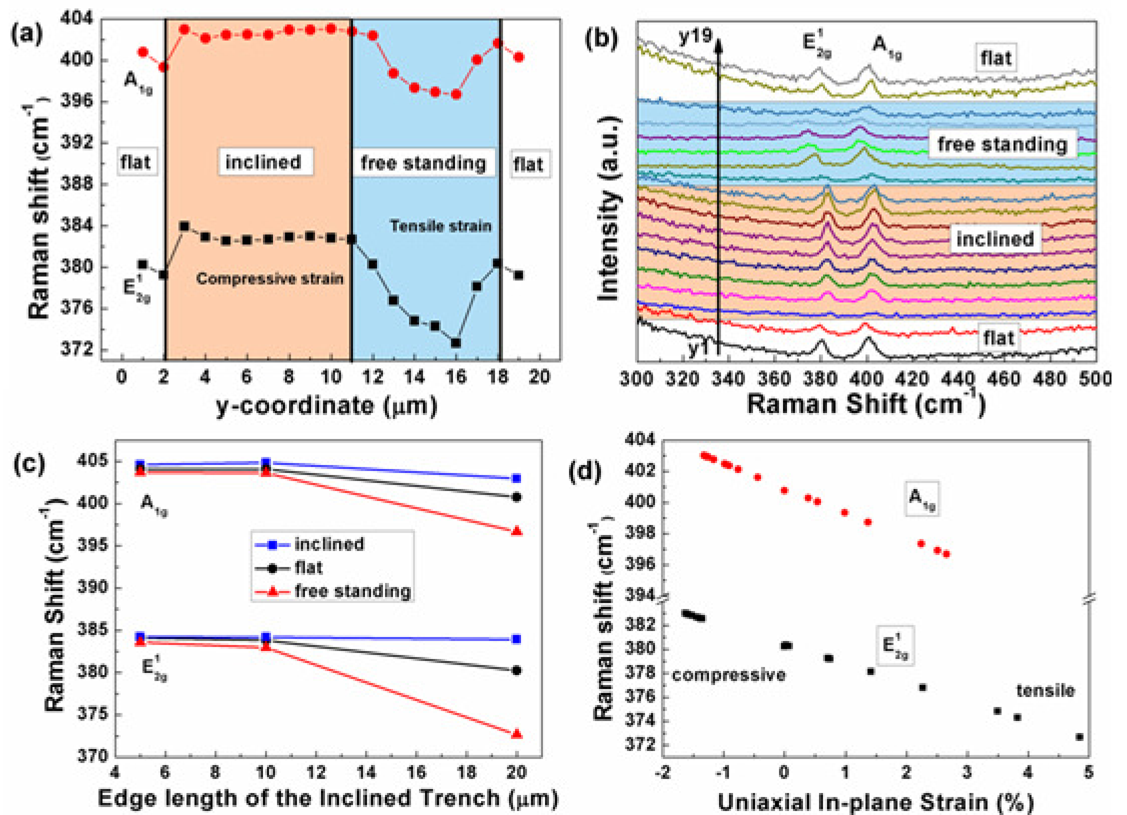

Fig. 6.5(a) Raman shifts (E_{2g}^1 and A_{1g} peaks) of the strained MoS_2 on a 20×20 μm^2 inclined trench as a function of y-direction. (b)Raman spectra of the corresponding sample in different regions. (c)Raman shift of the E_{2g}^1 and A_{1g} peaks as a function of edge length of the inclined trenches . (d)The estimated strain on the sample as a function of Raman shift [101].

Fig. 6.6(a) shows the Raman shifts of the E_{2g}^{1} and A_{1g} vibration modes for the sample on a 10×10 μm^2 inclined trench. It is noted that only tensile strain is induced onto the MoS_2. The E_{2g}^{1} and A_{1g} modes observed at observed at 384.6 and 404.8 cm^{-1} are shifted to lower frequencies of 383.0 and 403.6 cm^{-1} respectively under maximum strain. As mentioned before, the maximum depth of each trench is the same. The smaller the size of the trench is, the steeper is the slope. Thus, the trench with smaller size exhibit steeper slope can become free standing more easily. It also means that no compressive strain is induced in the 10×10 and 5×5 μm^2 samples. Moreover, the inclined trench (10×10 μm^2) with smaller size will lead to smaller induced strains as shown in Fig. 6.6(b). The maximum induced tensile strain is ~1.08 %.

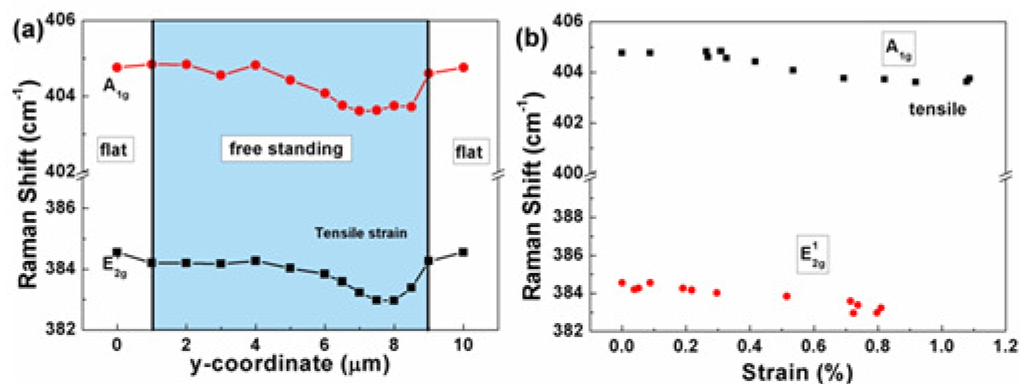

Fig. 6.6(a) Raman shift profile alone the y-direction of the strained MoS_2 on a 10×10 μm^2 trench of the E_{2g}^{1} and A_{1g} peaks. (b) The Raman shifts as a function of strain.

As shown in Fig. 6.7(a), the strain profile of the MoS_2 is almost unchanged along the x-direction. In other words, the E_{2g}^1 and A_{1g} modes originally observed at 380.3 and 400.8 cm^{-1} respectively were unchanged along the lateral direction. Fig. 6.7(b) shows the Raman spectra of the MoS_2 in the x-direction on a 20×20 μm^2 inclined trench at the free standing region. The linear mapping result is corresponding well with the spatial mapping results obtained above.

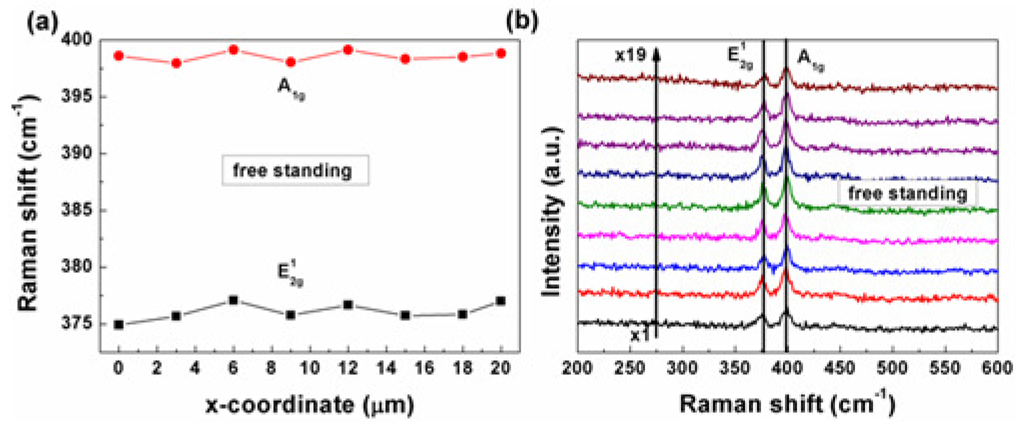

Fig. 6.7(a)Raman shift profile of the strained MoS_2 on a 10×10 μm^2 trench alone the x-direction of the E_{2g}^1 and A_{1g} modes. (b)Raman spectra of the strained MoS_2 along the x-direction.

6.3.3 PL characterization of the strained MoS_2

The evolution of the electronic structure in the MoS_2 under uniaxial strain was also investigated by PL spectroscopy. At the strain-free state, a broad PL peak centered at around 558 nm is observed, which could be assigned to the direct band

emission of MoS_2. Fig. 6.8(a) presents the PL spectra of the MoS_2 sample on a 10×10 μm^2 trench along the y-direction. As the strain increases, the PL emission peak shifts to higher wavelength from 663 to 672 nm. A shift of 9 nm is recorded for the tensile strain. Upon slow release of the strain, the PL peak position is generally return to its original position as shown in Fig. 6.8(b).

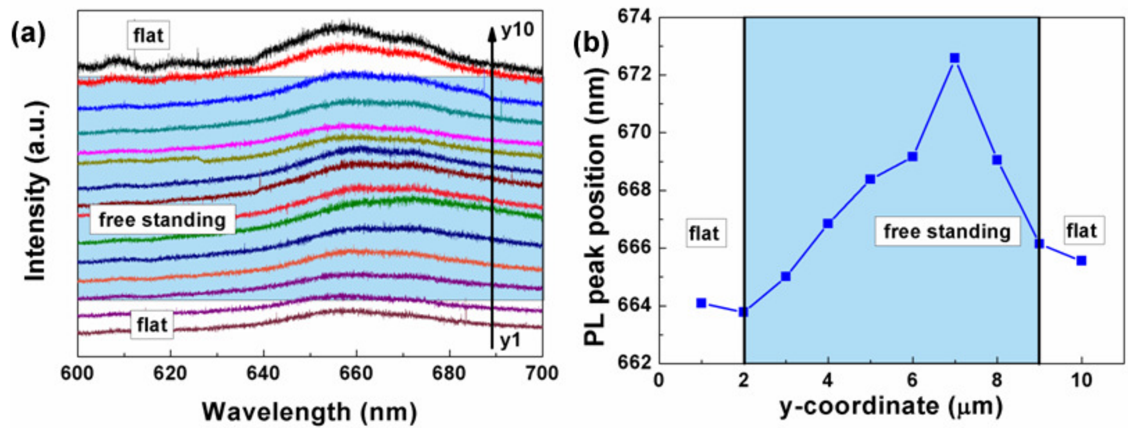

Fig. 6.8(a)PL spectra of the MoS_2 along y-direction on a 10×10 μm^2 trench. (b)PL peak position as a function of y-direction.

Fig. 6.9(a) shows the PL spectra of the 20×20 μm^2 sample at different regions of the trench. The PL peak position is shifted from ~660 to 663 nm under ~-1.6 % compressive strain, whereas the peak position is shifted from 663 to 674 nm under ~4.85 % tensile strain. The total PL shift is 14 nm. The magnitude of the tensile strain is much larger than that of the compressive strain. The PL shift of 11 nm under tensile strain is corresponded to a shift of 8 cm^{-1} in Raman shift of the E_{2g}^{1}

mode. Fig. 6.9(b) shows the PL peak positions of the samples with different trench sizes at different regions. Similar to the Raman results, no compressive strains could be observed from the 5×5 and 10×10 μm^2 trenches because the slope of the inclined trenches are steeper. It is found that as the trench size becomes larger, the shift of the peak position is larger. This result corresponds well with the size dependent Raman shift results obtained above.

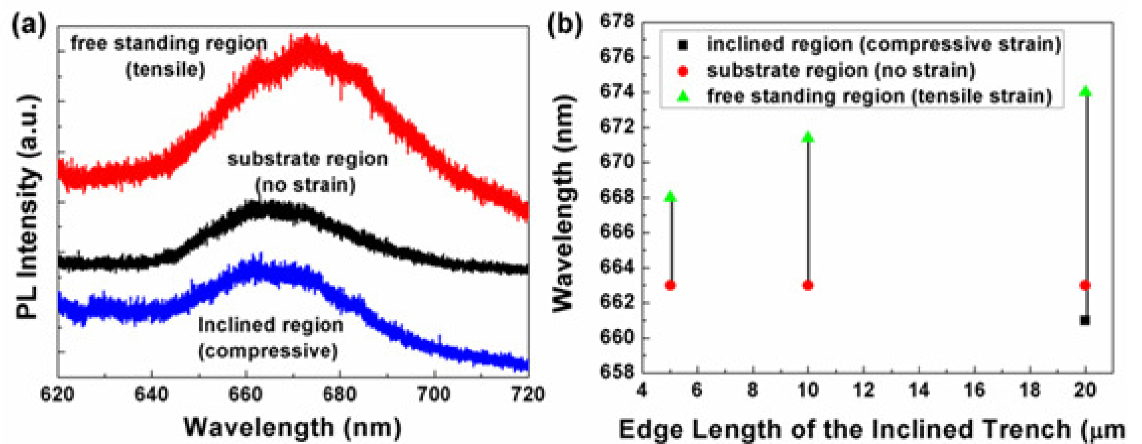

Fig. 6.9 (a)PL spectra of the sample with 20×20 μm^2 trench size at different regions. (b)The variation of PL peak positions of the samples with different edge length of the inclined trenches: 5×5, 10×10 and 20×20 μm^2.

6.4 Summary

In summary, the approach described in this chapter is based on the inclined trenches which induced local compressive and tensile strains continuously on 2D material. In addition to the ability to tune the Raman shift over a large range of ~12 cm^{-1}, the applied strain could also tune the emission energy over a range of ~14 nm. The

Raman and PL shift of the MoS_2 created by this method are the largest among all the reports. Most importantly, no external agent is needed to create such large amount of strain. The methodology could be employed on a wide range of 2D crystals and substrates. Besides, the band structure is useful for us to investigate in detail the effects produced by tunable uniaxial strains on other important physical properties of 2D crystals such as ferromagnetism and fabrication new generation semiconducting devices. We envision its use in high-performance electronic, piezoelectric, photovoltaic, optoelectronic, and spintronic devices.

Chapter 7 Conclusion and Future Work

7.1 Conclusion

In this work, large area monolayer graphene, monolayer MoS_2 and tri-layer MoS_2 were obtained using CVD methods. Samples of few centimeters were obtained. Graphene can be used as transparent electrode and protective layer for the strained devices that we have fabricated. Therefore, the application of graphene in 2D semiconductor is demonstrated

We demonstrated the application of graphene in GFETs. The realization of n- and *p*-type graphene field-effect transistors (GFETs) by controlling merely the thickness of a zinc oxide (ZnO) nanomesh deposited on the graphene was established. It is found that the effect of thermal strain acting on the graphene by the substrate can be minimized for the devices that are covered with a layer of ZnO nanomesh. We also demonstrated that the electronic structure of the single-layer graphene can be differentially modulated by controlling the thickness of the ZnO nanomesh upon the graphene surface. It suggests that graphene can also be used in other applications although it does not have a bandgap.

We also applied graphene as a transparent electrode for an electromechanical

device that we have developed. The electromechanical device can apply biaxial compressive strain to MoS_2 supported by a piezoelectric substrate and covered by a transparent graphene electrode. Large blue shift of the PL peak per strain (~ 300 meV per 1%) was obtained. First principles investigations confirmed the blue-shift of the direct bandgap and revealed a higher tunability of the indirect bandgap than the direct one. The exceptionally high strain tunability of the electronic structure in MoS2 is revealed.

Not only graphene could be utilized as transparent electrode, it could also be used as protective layer. We developed a novel approach to apply continuous strain to 2D materials on arbitrary substrates. Monolayer MoS_2 was transferred onto patterned SiO_2/Si substrates with inclined trenches of different sizes, ranging from 5×5 to 20×20 μm^2. This structure created continuous strain from tensile to compressive. Exceptional Raman and PL shift of 12 cm^{-1} and 14 nm were recorded respectively, where the Raman shift was the largest among the literature reports. It is found that the amount of strain applied depends on the size of the trenches. The approach provides a platform to study the strain induced properties in 2D semiconductors. Most importantly, it can apply to any 2D materials and arbitrary substrates, which can open up new opportunities for the fabrication of new generation nanoelectronic devices.

7.2 Future work

It is believed that the FET properties of the MoS_2 can be tuned by strain. For example, the mobility of the charge carriers can be tuned by applying strain into MoS_2. By doing so, our strain engineering method for MoS_2 can be applied to the strain-assisted FET. The advantage of our method is that no external agent is needed to create the required strain on the MoS_2. Fig 7.1 shows the proposed strain-assisted MoS_2 FET. A uniform trench is used to create the required strain so that the electrical properties will be symmetric on both end of the sample. We anticipated that the speed of the FET can effectively be enhanced in this way.

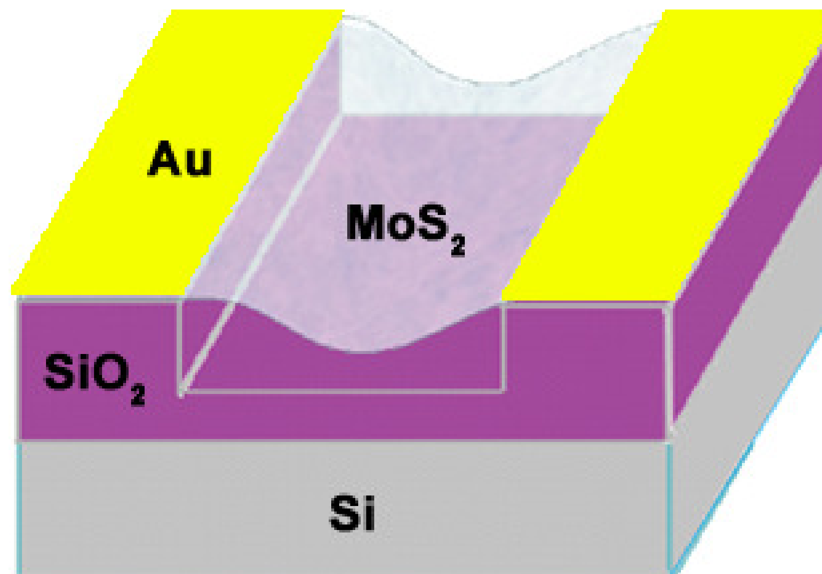

Fig. 7.1 Schematic diagram showing a free standing MoS_2 FET.

References

1. Zeming, G., *A Discussion of the Relationship between the Structure of the Transition-Metal Dichalcogenides and Their Lubrication Performance,* Asle Transactions **25,** 207-212 (1982)
2. Bednorz, J.G. and K.A. Muller, *Possible High-Tc Superconductivity in the Ba-La-Cu-O System,* Zeitschrift Fur Physik B-Condensed Matter **64,** 189-193 (1986)
3. Kamihara, Y., H. Hiramatsu, M. Hirano, R. Kawamura, H. Yanagi, T. Kamiya, and H. Hosono, *Iron-based layered superconductor: LaOFeP,* Journal of the American Chemical Society **128,** 10012-10013 (2006)
4. Geim, A.K., K.S. Novoselov, S.V. Morozov, D. Jiang, Y. Zhang, S.V. Dubonos, I.V. Grigorieva, and A.A. Firsov, *Electric field effect in atomically thin carbon films,* Science **306,** 666-669 (2004)
5. Stankovich, S., D.A. Dikin, G.H.B. Dommett, K.M. Kohlhaas, E.J. Zimney, E.A. Stach, R.D. Piner, S.T. Nguyen, and R.S. Ruoff, *Graphene-based composite materials,* Nature **442,** 282-286 (2006)
6. Kim, K.S., Y. Zhao, H. Jang, S.Y. Lee, J.M. Kim, K.S. Kim, J.H. Ahn, P. Kim, J.Y. Choi, and B.H. Hong, *Large-scale pattern growth of graphene films for stretchable transparent electrodes,* Nature **457,** 706-710 (2009)
7. Yang, H., J. Heo, S. Park, H.J. Song, D.H. Seo, K.E. Byun, P. Kim, I. Yoo, H.J. Chung, and K. Kim, *Graphene Barristor, a Triode Device with a Gate-Controlled Schottky Barrier,* Science **336,** 1140-1143 (2012)
8. Schwierz, F., *Graphene transistors,* Nature Nanotechnology **5,** 487-496 (2010)
9. Butler, S.Z., S.M. Hollen, L.Y. Cao, Y. Cui, J.A. Gupta, H.R. Gutierrez, T.F. Heinz, S.S. Hong, J.X. Huang, A.F. Ismach, E. Johnston-Halperin, M. Kuno, V.V. Plashnitsa, R.D. Robinson, R.S. Ruoff, S. Salahuddin, J. Shan, L. Shi, M.G. Spencer, M. Terrones, W. Windl, and J.E. Goldberger, *Progress, Challenges, and Opportunities in Two-Dimensional Materials Beyond Graphene,* Acs Nano **7,** 2898-2926 (2013)
10. Eknapakul, T., P.D.C. King, M. Asakawa, P. Buaphet, R.H. He, S.K. Mo, H. Takagi, K.M. Shen, F. Baumberger, T. Sasagawa, S. Jungthawan, and W. Meevasana, *Electronic Structure of a Quasi-Freestanding MoS_2 Monolayer,* Nano Letters **14,** 1312-1316 (2014)
11. Li, X.S., W.W. Cai, L. Colombo, and R.S. Ruoff, *Evolution of Graphene Growth*

on Ni and Cu by Carbon Isotope Labeling, Nano Letters **9,** 4268-4272 (2009)

12. Liang, C., W.R. Wang, T. Li, and Y.L. Wang, *Optimization on the Synthesis of Large-area Single-crystal Graphene Domains by Chemical Vapor Deposition on Copper Foils,* 2012 International Conference on Manipulation, Manufacturing and Measurement on the Nanoscale (3m-Nano) 144-147 (2012)
13. Ling, X., Y.H. Lee, Y.X. Lin, W.J. Fang, L.L. Yu, M.S. Dresselhaus, and J. Kong, *Role of the Seeding Promoter in MoS_2 Growth by Chemical Vapor Deposition,* Nano Letters **14,** 464-472 (2014)
14. Wu, S.F., C.M. Huang, G. Aivazian, J.S. Ross, D.H. Cobden, and X.D. Xu, *Vapor-Solid Growth of High Optical Quality MoS_2 Monolayers with Near-Unity Valley Polarization,* Acs Nano **7,** 2768-2772 (2013)
15. Wang, Q.H., K. Kalantar-Zadeh, A. Kis, J.N. Coleman, and M.S. Strano, *Electronics and optoelectronics of two-dimensional transition metal dichalcogenides,* Nature Nanotechnology **7,** 699-712 (2012)
16. Yan, R.H., A. Ourmazd, and K.F. Lee, *Scaling the Si Mosfet - from Bulk to Soi to Bulk,* Ieee Transactions on Electron Devices **39,** 1704-1710 (1992)
17. Datta, S., *Atom to transistor: A bottom-up viewpoint,* Abstracts of Papers of the American Chemical Society **230,** U2776-U2777 (2005)
18. Luisier, M., M. Lundstrom, D.A. Antoniadis, and J. Bokor, *Ultimate device scaling: intrinsic performance comparisons of carbon-based, InGaAs, and Si field-effect transistors for 5 nm gate length,* 2011 Ieee International Electron Devices Meeting (Iedm) (2011)
19. Radisavljevic, B., A. Radenovic, J. Brivio, V. Giacometti, and A. Kis, *Single-layer MoS_2 transistors,* Nature Nanotechnology **6,** 147-150 (2011)
20. Mak, K.F., C. Lee, J. Hone, J. Shan, and T.F. Heinz, *Atomically Thin MoS_2: A New Direct-Gap Semiconductor,* Physical Review Letters **105,** 136805 (2010)
21. Feng, J., X.F. Qian, C.W. Huang, and J. Li, *Strain-engineered artificial atom as a broad-spectrum solar energy funnel,* Nature Photonics **6,** 865-871 (2012)
22. Castellanos-Gomez, A., R. Roldan, E. Cappelluti, M. Buscema, F. Guinea, H.S.J. van der Zant, and G.A. Steele, *Local Strain Engineering in Atomically Thin MoS_2,* Nano Letters **13,** 5361-5366 (2013)
23. Liu, K.K., W. Zhang, Y.H. Lee, Y.C. Lin, M.T. Chang, C.Y. Su, C.S. Chang, H. Li, Y. Shi, H. Zhang, C.S. Lai, and L.J. Li, *Growth of Large-Area and Highly Crystalline MoS_2 Thin Layers on Insulating Substrates,* Nano Letters **12,** 1538-1544 (2012)
24. Clegg, W., *Crystal structure determination*. Oxford chemistry primers 60, Oxford ; New York: Oxford University Press (1998)
25. Giacovazzo, C., *Fundamentals of crystallography*. International Union of

Crystallography texts on crystallography 2, Oxford ; New York: International Union of Crystallography; Oxford University Press (1992)

26. Goldstein, J., *Scanning electron microscopy and X-ray microanalysis : a text for biologists, materials scientists, and geologists*. 2nd ed, New York: Plenum Press (1992)

27. Anderson, R.M. and S.D. Walck, *Specimen preparation for transmission electron microscopy of materials IV : symposium held April 2, 1997, San Francisco, California, U.S.A*. Materials Research Society symposium proceeedings, Pittsburgh, Pa.: Materials Research Society (1997)

28. Buseck, P., J.M. Cowley, and L. Eyring, *High-resolution transmission electron microscopy and associated techniques*, New York: Oxford University Press (1988)

29. Ozawa, L., *Cathodoluminescence and photoluminescence : theories and practical applications*. Phosphor science and engineering 2, Boca Raton: CRC Press (2007)

30. Gucsik, A., *Cathodoluminescence and its application in the planetary sciences*, Berlin: Springer (2009)

31. Geim, A.K., K.S. Novoselov, S.V. Morozov, D. Jiang, M.I. Katsnelson, I.V. Grigorieva, S.V. Dubonos, and A.A. Firsov, *Two-dimensional gas of massless Dirac fermions in graphene,* Nature **438,** 197-200 (2005)

32. Kim, P., Y.B. Zhang, Y.W. Tan, and H.L. Stormer, *Experimental observation of the quantum Hall effect and Berry's phase in graphene,* Nature **438,** 201-204 (2005)

33. Wang, C., Z.G. Cheng, Q.Y. Zhou, C.X. Wang, Q.A. Li, and Y. Fang, *Toward Intrinsic Graphene Surfaces: A Systematic Study on Thermal Annealing and Wet-Chemical Treatment of SiO(2)-Supported Graphene Devices,* Nano Letters **11,** 767-771 (2011)

34. Yacoby, A., J. Martin, N. Akerman, G. Ulbricht, T. Lohmann, J.H. Smet, and K. Von Klitzing, *Observation of electron-hole puddles in graphene using a scanning single-electron transistor,* Nature Physics **4,** 144-148 (2008)

35. Moser, J., A. Verdaguer, D. Jimenez, A. Barreiro, and A. Bachtold, *The environment of graphene probed by electrostatic force microscopy,* Applied Physics Letters **92,** 123507 (2008)

36. Novoselov, K.S., F. Schedin, A.K. Geim, S.V. Morozov, E.W. Hill, P. Blake, and M.I. Katsnelson, *Detection of individual gas molecules adsorbed on graphene,* Nature Materials **6,** 652-655 (2007)

37. Liu, J.W., G.W. Xu, C. Rochford, R.T. Lu, J. Wu, C.M. Edwards, C.L. Berrie, Z.J. Chen, and V.A. Maroni, *Doped graphene nanohole arrays for flexible*

transparent conductors, Applied Physics Letters **99,** 023111 (2011)

38. Chen, P., X.C. Dong, D.L. Fu, W.J. Fang, Y.M. Shi, and L.J. Li, *Doping Single-Layer Graphene with Aromatic Molecules,* Small **5,** 1422-1426 (2009)
39. Szafranek, B.N., D. Schall, M. Otto, D. Neumaier, and H. Kurz, *High On/Off Ratios in Bilayer Graphene Field Effect Transistors Realized by Surface Dopants,* Nano Letters **11,** 2640-2643 (2011)
40. Cho, B.J., W.C. Shin, and S. Seo, *Highly air-stable electrical performance of graphene field effect transistors by interface engineering with amorphous fluoropolymer,* Applied Physics Letters **98,** 153505 (2011)
41. Tian, J.F., L.A. Jauregui, G. Lopez, H. Cao, and Y.P. Chen, *Ambipolar graphene field effect transistors by local metal side gates,* Applied Physics Letters **96,** 263110 (2010)
42. Tao, N.J., J.L. Xia, F. Chen, P. Wiktor, and D.K. Ferry, *Effect of Top Dielectric Medium on Gate Capacitance of Graphene Field Effect Transistors: Implications in Mobility Measurements and Sensor Applications,* Nano Letters **10,** 5060-5064 (2010)
43. Sato, S., D. Kondo, K. Yagi, N. Harada, M. Sato, M. Nihei, and N. Yokoyama, *Low-Temperature Synthesis of Graphene and Fabrication of Top-Gated Field Effect Transistors without Using Transfer Processes,* Applied Physics Express **3,** 025102 (2010)
44. Ahn, J.H., B.J. Kim, H. Jang, S.K. Lee, B.H. Hong, and J.H. Cho, *High-Performance Flexible Graphene Field Effect Transistors with Ion Gel Gate Dielectrics,* Nano Letters **10,** 3464-3466 (2010)
45. Sabri, S.S., P.L. Levesque, C.M. Aguirre, J. Guillemette, R. Martel, and T. Szkopek, *Graphene field effect transistors with parylene gate dielectric,* Applied Physics Letters **95,** 242104 (2009)
46. Kocabas, C. and E. Pince, *Investigation of high frequency performance limit of graphene field effect transistors,* Applied Physics Letters **97,** 173106 (2010)
47. Flynn, G.W., S. Ryu, L. Liu, S. Berciaud, Y.J. Yu, H.T. Liu, P. Kim, and L.E. Brus, *Atmospheric Oxygen Binding and Hole Doping in Deformed Graphene on a SiO(2) Substrate,* Nano Letters **10,** 4944-4951 (2010)
48. Wang, D.Y., G. Zhang, Z.Z. Gu, and H. Mohwald, *Fabrication of superhydrophobic surfaces from binary colloidal assembly,* Langmuir **21,** 9143-9148 (2005)
49. Wang, Y.G., S.P. Lau, H.W. Lee, S.F. Yu, B.K. Tay, X.H. Zhang, K.Y. Tse, and H.H. Hng, *Comprehensive study of ZnO films prepared by filtered cathodic vacuum arc at room temperature,* Journal of Applied Physics **94,** 1597-1604 (2003)

50. Wiesner, U., M. Kamperman, A. Burns, R. Weissgraeber, N. van Vegten, S.C. Warren, S.M. Gruner, and A. Baiker, *Integrating Structure Control over Multiple Length Scales in Porous High Temperature Ceramics with Functional Platinum Nanoparticles,* Nano Letters **9,** 2756-2762 (2009)
51. Xia, F.N., D.B. Farmer, Y.M. Lin, and P. Avouris, *Graphene Field-Effect Transistors with High On/Off Current Ratio and Large Transport Band Gap at Room Temperature,* Nano Letters **10,** 715-718 (2010)
52. Morozov, S.V., K.S. Novoselov, M.I. Katsnelson, F. Schedin, D.C. Elias, J.A. Jaszczak, and A.K. Geim, *Giant intrinsic carrier mobilities in graphene and its bilayer,* Physical Review Letters **100,** 016602 (2008)
53. Krstic, V., D. Obergfell, S. Hansel, G.L.J.A. Rikken, J.H. Blokland, M.S. Ferreira, and S. Roth, *Graphene-metal interface: Two-terminal resistance of low-mobility graphene in high magnetic fields,* Nano Letters **8,** 1700-1703 (2008)
54. Hong, X., A. Posadas, K. Zou, C.H. Ahn, and J. Zhu, *High-Mobility Few-Layer Graphene Field Effect Transistors Fabricated on Epitaxial Ferroelectric Gate Oxides,* Physical Review Letters **102,** 136808 (2009)
55. Herng, T.S., S.P. Lau, S.F. Yu, S.H. Tsang, K.S. Teng, and J.S. Chen, *Ferromagnetic Cu doped ZnO as an electron injector in heterojunction light emitting diodes,* Journal of Applied Physics **104,** 103104 (2008)
56. Xu, H., L.M. Xie, H.L. Zhang, and J. Zhang, *Effect of Graphene Fermi Level on the Raman Scattering Intensity of Molecules on Graphene,* Acs Nano **5,** 5338-5344 (2011)
57. Sofo, J.O., H.E. Romero, N. Shen, P. Joshi, H.R. Gutierrez, S.A. Tadigadapa, and P.C. Eklund, *n-Type Behavior of Graphene Supported on Si/SiO$_2$ Substrates,* Acs Nano **2,** 2037-2044 (2008)
58. Tan, Y.W., Y. Zhang, K. Bolotin, Y. Zhao, S. Adam, E.H. Hwang, S. Das Sarma, H.L. Stormer, and P. Kim, *Measurement of scattering rate and minimum conductivity in graphene,* Physical Review Letters **99,** 246803 (2007)
59. Du, X., I. Skachko, A. Barker, and E.Y. Andrei, *Approaching ballistic transport in suspended graphene,* Nature Nanotechnology **3,** 491-495 (2008)
60. Ferrari, A.C., A. Das, S. Pisana, B. Chakraborty, S. Piscanec, S.K. Saha, U.V. Waghmare, K.S. Novoselov, H.R. Krishnamurthy, A.K. Geim, and A.K. Sood, *Monitoring dopants by Raman scattering in an electrochemically top-gated graphene transistor,* Nature Nanotechnology **3,** 210-215 (2008)
61. Ferrari, A.C., J.C. Meyer, V. Scardaci, C. Casiraghi, M. Lazzeri, F. Mauri, S. Piscanec, D. Jiang, K.S. Novoselov, S. Roth, and A.K. Geim, *Raman spectrum of graphene and graphene layers,* Physical Review Letters **97,** 187401 (2006)

62. Kim, K., H.J. Park, B.C. Woo, K.J. Kim, G.T. Kim, and W.S. Yun, *Electric Property Evolution of Structurally Defected Multilayer Graphene,* Nano Letters **8,** 3092-3096 (2008)
63. Ni, Z.H., T. Yu, Y.H. Lu, Y.Y. Wang, Y.P. Feng, and Z.X. Shen, *Uniaxial Strain on Graphene: Raman Spectroscopy Study and Band-Gap Opening (vol 2, pg 2301, 2008),* Acs Nano **3,** 483-483 (2009)
64. Wei, D.C., Y.Q. Liu, Y. Wang, H.L. Zhang, L.P. Huang, and G. Yu, *Synthesis of N-Doped Graphene by Chemical Vapor Deposition and Its Electrical Properties,* Nano Letters **9,** 1752-1758 (2009)
65. Fischetti, M.V. and S.E. Laux, *Band structure, deformation potentials, and carrier mobility in strained Si, Ge, and SiGe alloys,* Journal of Applied Physics **80,** 2234-2252 (1996)
66. Feng, J., X. Qian, C.-W. Huang, and J. Li, *Strain-engineered artificial atom as a broad-spectrum solar energy funnel,* Nature Photonics **6,** 866-872 (2012)
67. Kato, Y., R.C. Myers, A.C. Gossard, and D.D. Awschalom, *Coherent spin manipulation without magnetic fields in strained semiconductors,* Nature **427,** 50-53 (2004)
68. Yang, Q., W.H. Wang, S. Xu, and Z.L. Wang, *Enhancing Light Emission of ZnO Microwire-Based Diodes by Piezo-Phototronic Effect,* Nano Letters **11,** 4012-4017 (2011)
69. Signorello, G., S. Karg, M.T. Björk, B. Gotsmann, and H. Riel, *Tuning the Light Emission from GaAs Nanowires over 290 meV with Uniaxial Strain,* Nano Letters **13,** 917-924 (2013)
70. Wei, B., K. Zheng, Y. Ji, Y. Zhang, Z. Zhang, and X. Han, *Size-Dependent Bandgap Modulation of ZnO Nanowires by Tensile Strain,* Nano Letters **12,** 4595-4599 (2012)
71. Lee, C., X. Wei, J.W. Kysar, and J. Hone, *Measurement of the Elastic Properties and Intrinsic Strength of Monolayer Graphene,* Science **321,** 385-388 (2008)
72. Ni, Z.H., T. Yu, Y.H. Lu, Y.Y. Wang, Y.P. Feng, and Z.X. Shen, *Uniaxial Strain on Graphene: Raman Spectroscopy Study and Band-Gap Opening,* Acs Nano **2,** 2301-2305 (2008)
73. Lu, P., X. Wu, W. Guo, and X.C. Zeng, *Strain-dependent electronic and magnetic properties of MoS_2 monolayer, bilayer, nanoribbons and nanotubes,* Physical Chemistry Chemical Physics **14,** 13035-13040 (2012)
74. Kresse, G. and J. Furthmuller, *Efficient iterative schemes for ab initio total-energy calculations using a plane-wave basis set,* Physical Review B **54,** 11169-11186 (1996)
75. Kresse, G. and J. Hafner, *Ab initio molecular dynamics for liquid metals,*

Physical Review B **47,** 558-561 (1993)

76. Blöchl, P.E., *Projector augmented-wave method,* Physical Review B **50,** 17953-17979 (1994)
77. Kresse, G. and D. Joubert, *From ultrasoft pseudopotentials to the projector augmented-wave method,* Physical Review B **59,** 1758-1775 (1999)
78. Perdew, J.P., K. Burke, and M. Ernzerhof, *Generalized Gradient Approximation Made Simple,* Physical Review Letters **77,** 3865-3868 (1996)
79. Zhang, Y., G. Gao, H.L.W. Chan, J. Dai, Y. Wang, and J. Hao, *Piezo-Phototronic Effect-Induced Dual-Mode Light and Ultrasound Emissions from ZnS:Mn/PMN–PT Thin-Film Structures,* Advanced Materials **24,** 1729-1735 (2012)
80. Zheng, R.K., Y. Wang, J. Wang, K.S. Wong, H.L.W. Chan, C.L. Choy, and H.S. Luo, *Tuning the electrical properties of* $La_{0.75}Ca_{0.25}MnO_3$ *thin films by ferroelectric polarization, ferroelectric-field effect, and converse piezoelectric effect,* Physical Review B **74,** 094427-094433 (2006)
81. Rastelli, A., F. Ding, J.D. Plumhof, S. Kumar, R. Trotta, C. Deneke, A. Malachias, P. Atkinson, E. Zallo, T. Zander, A. Herklotz, R. Singh, V. Krapek, J.R. Schroter, S. Kiravittaya, M. Benyoucef, R. Hafenbrak, K.D. Jons, D.J. Thurmer, D. Grimm, G. Bester, K. Dorr, P. Michler, and O.G. Schmidt, *Controlling quantum dot emission by integration of semiconductor nanomembranes onto piezoelectric actuators,* Physica Status Solidi B-Basic Solid State Physics **249,** 687-696 (2012)
82. Yue, Q., J. Kang, Z.Z. Shao, X.A. Zhang, S.L. Chang, G. Wang, S.Q. Qin, and J.B. Li, *Mechanical and electronic properties of monolayer* MoS_2 *under elastic strain,* Physics Letters A **376,** 1166-1170 (2012)
83. Lee, C., H. Yan, L.E. Brus, T.F. Heinz, J. Hone, and S. Ryu, *Anomalous Lattice Vibrations of Single- and Few-Layer* MoS_2*,* Acs Nano **4,** 2695-2700 (2010)
84. Li, H., Q. Zhang, C.C.R. Yap, B.K. Tay, T.H.T. Edwin, A. Olivier, and D. Baillargeat, *From Bulk to Monolayer* MoS_2*: Evolution of Raman Scattering,* Advanced Functional Materials **22,** 1385-1390 (2012)
85. Viršek, M., A. Jesih, I. Milošević, M. Damnjanović, and M. Remskar, *Raman scattering of the* MoS_2 *and* WS_2 *single nanotubes,* Surface Science **601,** 2868-2872 (2007)
86. Bagnall, A.G., W.Y. Liang, E.A. Marseglia, and B. Welber, *Raman Studies of* MoS_2 *at High-Pressure,* Physica B & C **99,** 343-346 (1980)
87. Tongay, S., J. Zhou, C. Ataca, K. Lo, T.S. Matthews, J.B. Li, J.C. Grossman, and J.Q. Wu, *Thermally Driven Crossover from Indirect toward Direct Bandgap in 2D Semiconductors:* $MoSe_2$ *versus* MoS_2*,* Nano Letters **12,** 5576-5580 (2012)
88. Mak, K.F., K. He, C. Lee, G.H. Lee, J. Hone, T.F. Heinz, and J. Shan, *Tightly*

bound trions in monolayer MoS_2, Nature Materials **12,** 207-211 (2012)

89. Kwon, S.S., W.K. Hong, G. Jo, J. Maeng, T.W. Kim, S. Song, and T. Lee, *Piezoelectric Effect on the Electronic Transport Characteristics of ZnO Nanowire Field-Effect Transistors on Bent Flexible Substrates,* Advanced Materials **20,** 4557-4562 (2008)
90. Liu, Q., L. Li, Y. Li, Z. Gao, Z. Chen, and J. Lu, *Tuning Electronic Structure of Bilayer MoS_2 by Vertical Electric Field: A First-Principles Investigation,* The Journal of Physical Chemistry C **116,** 21556-21562 (2012)
91. Zhou, Y., Z. Wang, P. Yang, X. Zu, L. Yang, X. Sun, and F. Gao, *Tensile Strain Switched Ferromagnetism in Layered NbS_2 and $NbSe_2$,* Acs Nano **6,** 9727-9736 (2012)
92. Pan, H. and Y.-W. Zhang, *Tuning the Electronic and Magnetic Properties of MoS_2 Nanoribbons by Strain Engineering,* The Journal of Physical Chemistry C **116,** 11752-11757 (2012)
93. High, A.A., J.R. Leonard, M. Remeika, L.V. Butov, M. Hanson, and A.C. Gossard, *Condensation of Excitons in a Trap,* Nano Letters **12,** 2605-2609 (2012)
94. van der Zande, A. and J. Hone, *Optical Materials Inspired by Strain,* Nature Photonics **6,** 803-805 (2012)
95. Lin, M.W., L.Z. Liu, Q. Lan, X.B. Tan, K.S. Dhindsa, P. Zeng, V.M. Naik, M.M.C. Cheng, and Z.X. Zhou, *Mobility enhancement and highly efficient gating of monolayer MoS_2 transistors with polymer electrolyte,* Journal of Physics D-Applied Physics **45,** 345102 (2012)
96. Yin, Z.Y., H. Li, H. Li, L. Jiang, Y.M. Shi, Y.H. Sun, G. Lu, Q. Zhang, X.D. Chen, and H. Zhang, *Single-Layer MoS_2 Phototransistors,* Acs Nano **6,** 74-80 (2012)
97. Sundaram, R.S., M. Engel, A. Lombardo, R. Krupke, A.C. Ferrari, P. Avouris, and M. Steiner, *Electroluminescence in Single Layer MoS_2,* Nano Letters **13,** 1416-1421 (2013)
98. Cooper, R.C., C. Lee, C.A. Marianetti, X.D. Wei, J. Hone, and J.W. Kysar, *Nonlinear elastic behavior of two-dimensional molybdenum disulfide,* Physical Review B **87,** (2013)
99. Bertolazzi, S., J. Brivio, and A. Kis, *Stretching and Breaking of Ultrathin MoS_2,* Acs Nano **5,** 9703-9709 (2011)
100. Balandin, A.A., S. Ghosh, W.Z. Bao, I. Calizo, D. Teweldebrhan, F. Miao, and C.N. Lau, *Superior thermal conductivity of single-layer graphene,* Nano Letters **8,** 902-907 (2008)
101. Yang, L., X. Cui, J. Zhang, K. Wang, M. Shen, S. Zeng, S.A. Dayeh, L. Feng,

and B. Xiang, *Lattice strain effects on the optical properties of MoS_2 nanosheets,* Sci Rep **4,** 5649 (2014)